1994

Implementation of Ultrafast Optical Characterization Techniques

Nicholas J. Croglio
University of Central Florida, ncroglio@yahoo.com

ABSTRACT

The single beam Z-Scan technique, a two beam Pulse-Delay Modulation Technique (PDMT), and a combination of these methods are implemented to measure both nonlinear absorption and nonlinear refraction in semiconductors. The laser source used is a Kerr Lens Modelocked (KLM) Ti:sapphire laser producing tunable near IR 100 femtosecond pulses of ~5 nJ of energy per pulse at a 90 MHz repetition rate. Specifically we monitor two photon absorption and the bound electronic nonlinear refraction in ZnSe and this nonlinear refraction in ZnS.

These techniques open the spectral range where these nonlinear optical parameters can be measured by allowing tunable high repetition rate low pulse energy lasers to be used. In the past such measurements have been made primarily with high energy low repetition rate lasers such as Q-switched or modelocked and Q-switched Nd^{3+}:YAG lasers and its harmonics or Nd^{3+}:YAG pumped dye lasers. Such dye lasers while tunable are difficult to use and require organic dyes and solvents which may be flammable and/or carcinogenic. Recently, the solid state KLM Ti:sapphire laser has also been used to pump broadly tunable Optical Parametric Oscillators. The techniques discussed in this thesis will also allow such sources to be used for nonlinear optical measurements. Additionally, these material measurement techniques have a great deal in common with autocorrelation pulse width measurement techniques. Therefore, this thesis also discusses the pulse width measurement techniques that we used to characterize our laser system.

TABLE OF CONTENTS

LIST OF FIGURES

LIST OF TABLES

CHAPTER 1

INTRODUCTION

With the advent of the laser it has become possible to generate large electric fields, which change the usual rules of classical optics. At these high intensities the material response is no longer linearly dependent on the incident field strength, rather the material's optical properties such as index of refraction were found to depend on the intensity of the incident light. Therefore, by propagating through a material, the incident light was able to alter its own propagation, Hence, shortly after the discovery of the laser, the field of nonlinear optics was born [1].

The nonlinear optical properties of materials have exciting potential applications in the areas of optical limiting, fiber optical communications and all photonic switching, therefore the search is on for nonlinear optical materials that display a strong ability to generate these desired nonlinearities. The ability to accurately measure these nonlinearities over a large area of the spectrum is desired not only so these ideal nonlinear optical devices can be discovered, but also so that a database of information can be generated that will help refine theories related to these nonlinearities. Therefore, not only can general insight into the properties of the material be gained, but the ability to predict the nonlinearities will be gained. Hence, this knowledge can also be used to modify existing structures and materials as well as design new ones. In fact, these sorts of modifications to the linear and nonlinear optical properties of materials have already been performed in the areas of laser and nonlinear crystal growth, quantum confined structures [2], and organic molecules [3] just to name a few. Therefore, it is very desirable to be

able to measure these nonlinear parameters under a variety of conditions over the entire spectrum.

1.1 Purpose

In the past, such measurements have been made primarily with high energy low repetition rate lasers such as Q-switched or modelocked and Q-switched Nd:YAG lasers, CO_2 lasers and YAG pumped dye lasers. However, these solid state lasers are only capable of generating radiation at discrete frequencies and their harmonics, and the CO_2 laser is only useful in the 8-12 μm range. Whereas dye lasers provide tunable visible and near infrared radiation, they are difficult to use and require organic dyes and solvents which may be flammable and carcinogenic. Also, these dyes have a limited lifetime and must be changed to obtain tunability over a large amount of the spectrum.

Therefore, we are interested in finding experimental procedures that can independently determine the irradiance dependent and fluence dependent nonlinearities with a high repetition rate low pulse energy laser. This would allow for example, the ultrashort pulsed Ti:sapphire laser to be used for characterizing the nonlinear properties of materials. The Ti:sapphire laser is capable of generating broadly tunable radiation at its fundamental, and with a nonlinear crystal at its second harmonic, third harmonic and fourth harmonic as well as other frequencies from its use as a pump for Optical Parametric Oscillators(OPO's). Therefore, it would be possible to measure a very broad spectrum of a material's nonlinearities if this goal is achieved.

We implement the single beam Z-Scan technique, a two beam Pulse-Delay Modulation Technique (PDMT), and a combination of these methods to measure both nonlinear absorption and nonlinear refraction in semiconductors. Specifically, we use a Kerr Lens Modelocked (KLM) Ti:sapphire laser producing tunable near IR 100

femtosecond pulses of ~5 nJ of energy per pulse at a 90 MHz repetition rate to measure two photon absorption and the bound electronic nonlinear refraction in ZnSe and nonlinear refraction in ZnS.

1.2 Reason for Modulation

Eliminating system noise, laser fluctuations and differentiating between thermal and irradiance dependent nonlinearities is not a new concern. In fact, several tactics have been implemented so *low repetition* rate lasers can obtain a good signal to noise ratio while performing the single beam Z-scan.

Small deviations in the irradiance of the incident laser pulse can result in large variations in the measurements of nonlinear optical parameters, therefore it is important to have an accurate knowledge of the incident pulse energy, spatial profile and pulse width. Normally, this is done by performing careful characterization of these parameters before starting the experiment. Then, the $2/1^2$ ratio is monitored along with a reference detector that monitors the relative pulse energy, where the $2/1^2$ ratio is the ratio of the second harmonic energy to that of the energy of the fundamental squared. This ratio has been found to be inversely proportional to the pulse width. Then, the pre-experiment calibration is used to place windows on the pulse's width and energy, so that only the data that is generated by pulses that have the energy and pulse widths that fall within this narrowly defined window are used. Hence, the laser pulse fluctuations that would destroy the accuracy of experimental results can now be minimized to almost any arbitrary size. Furthermore, the fluctuations can be further reduced by dividing the measured output signal by the value of the reference detector.

However, for the above technique to work, there must be enough time between pulses for the detector to perform calculations between pulses, and for the data

acquisition system to accept or reject the resulting data point. Consequently, these methods cannot be easily implemented with cw mode locked lasers like the Ti:sapphire laser that have a period between pulses of about 10 nanoseconds. Yes, there are ways to reduce the repetition rate by picking off only certain pulses, but due to the low energy per pulse, the output would probably need to be amplified. In any event, for this type of procedure to be effective, the system's complexity and/or cost would significantly rise. In experiments performed with the higher repetition rate femtosecond laser it may be more difficult to differentiate between the irradiance and fluence dependent nonlinearities than with the lower repetition rate picosecond lasers. This is because the high frequency pulse train dumps a large power into the sample, while each individual pulse only carries a small amount of energy. Therefore, there is definitely a need for a different way in which to control the effects of noise, thermal effects and laser fluctuations on material characterization experiments with a self modelocked Ti:sapphire laser source. This is where the amplitude modulated Z-scan, the Pulse Delay Modulation Technique (PDMT) and the Pulse Delay Modulated Z-Scan(PDM Z-scan) can be of use. The effect of the laser fluctuations upon the signal to noise ratio is minimized through averaging. In the single beam Z-scan measurements, the excitation source is amplitude modulated by a high frequency to a lower noise part of the laser output spectrum, so that a lock in amplifier can amplify and average the signal while filtering out the wide band noise. In the two beam PDMT and PDM Z-scan, the addition of a variable path delay between two beams derived from the same source varies the irradiance while keeping the fluence constant, so that a second lock-in amplifier can lock-in on only the irradiance dependent signal. These techniques will be described in detail in Chapters 6 and 7. The results and analysis of the data obtained upon ZnSe and ZnS, as well as the experimental procedures will be given in Chapter 8 and Chapter 9 respectively.

The PDMT and PDM Z-scans are performed within an interferometric autocorrelation like set up, and precise pulse width characterization is imperative to obtaining accurate results when performing nonlinear optical experiments like these. Therefore, all of Chapter 5 will discuss the various pulse width characterization methods that we implemented for various laser sources.

1.3 Context of Research

The prime purpose of our Ti:sapphire laser is to be an oscillator for an Ultrafast Supercontinuum Laser Source(USLS), whose output is a white light continuum. A white light continuum is a coherent femtosecond laser pulse with an enormous bandwidth, which can be over 1000 nm wide [4]. As one can imagine such a source can be used for a great variety of applications [5]. However, this USLS will be used as a probe beam in pump probe experiments that will determine the nonlinear optical dispersion of materials. Therefore, the ideal USLS will efficiently produce a broad bandwidth pulse, with very little chirp from Group Velocity Dispersion(GVD).

A white light continuum is generated by the nonlinear interactions that occur when an ultrashort, high intensity laser pulse is focused into a medium. Although there are many nonlinear processes involved in supercontinuum generation, various forms of Self Phase Modulation(SPM), and Cross Phase Modulation(XPM)in conjunction with Stimulated Raman Scattering(SRS), and Four Photon Parametric Generation(FPPG) are primarily responsible for the large bandwidths observed [6]. Therefore, for the broadest supercontinuum possible, we need ultrashort high intensity pulses. The intense laser source will be created by picking off one 850 nm 100 femtosecond pulse from the Ti:sapphire oscillator, and amplifying it using the process of Chirped Pulse Amplification(CPA). The regenerative Cr:LiSAF amplifier that performs the

amplification will generate pulses in the millijoule range. Then, these chirped pulses need to be recompressed before they are focused upon the supercontinuum generating material.

While the amplifier system, which will be described in Chapter 3, which will generate the USLS was being built, we used a similar one in the Laser Plasma Laboratory(LPL). It was in the LPL that we performed the grating compression and single shot autocorrelation experiments that will be discussed in Chapter 4 (Methods of Pulse Compression) and Chapter 5 (Pulse Measurement Techniques) respectively. It was only after compressing and measuring the pulse that we were able to attempt to find the best configuration and materials for generating a white light continuum. The propagation of any high intensity ultrashort laser source can be greatly affected by the nonlinear and dispersive material effects, and some of these effects play important roles in the operation of the laser source itself. Therefore, in addition to discussing the laser systems in Chapter 3, these effects will be discussed. Additionally, the dispersive effects have an even more profound effect on the propagation of a 1000 nm wide USLS, and the nonlinear effects are responsible for the generation of the continuum.

REFERENCES FOR CHAPTER 1

[1] R. W. Boyd, Nonlinear Optics, Academic Press Inc., San Diego, 1992.

[2] C. Flytzanis, and Hutter, "Nonlinear Optics in Quantum Confined Structures," in Contemporary Nonlinear Optics (G. P. Agrawal, and R. W. Boyd, ed.), Academic Press, Inc., San Diego, 1992.

[3] P. N. Prasad, "Nonlinear Optical Effects in Organic Materials,", in Contemporary Nonlinear Optics (G. P. Agrawal, and R. W. Boyd, ed.), Academic Press, Inc., San Diego, 1992.

[4] R. L. Fork, C. V. Shank, C. Hirlmann, R. Yen, and W. J. Tomlinson, "Femtosecond white-light continuum pulses," *Opt Lett.* **8**, 1-3 (1983).

[5] R. Dorsinville, P. P. Ho, J. T. Manssah, and R. R. Alfano, "Applications of Supercontinuum: Present and Future," in The Supercontinuum Laser Source, (R. R. Alfano ed.) Springer-Verlag, New York, 1989.

[6] Q. Z. Wang, P.P. Ho, and R. R. Alfano, "Supercontinuum Generation in Condensed Matter." in The Supercontinuum Laser Source, (R. R. Alfano ed.) Springer-Verlag, New York, 1989.

CHAPTER 2

NONLINEAR OPTICAL PHENOMENA

When an intense beam of light passes into a medium, the rules of linear optics no longer apply. This intense beam interacts with the medium so that the material's properties are altered. Hence, the light beam changes its own path of propagation, which is referred to as self action. Now, the main thrust of this thesis is measuring the nonlinear optical phenomena of different materials that cause this self action, and using nonlinear optical materials to measure and characterize high irradiance ultrashort pulses. Additionally, performance of our laser systems, and the lasers pulse propagation are affected by these nonlinear optical phenomena. Therefore, this chapter as well as the chapter on the laser systems will include a discussion of the most relevant of these phenomena.

2.1 Nonlinear Polarization

In the case of linear optics, the dipole moment per unit volume or polarization P(t) of the medium depends linearly upon the electric field. Therefore, in terms of the linear electrical susceptibility $\chi^{(1)}$ and the permittivity of free space ε_o, the linear polarization can be written as

$$P(t) = \varepsilon_o \chi^{(1)} E(t). \qquad (2.1)$$

However, in general the electric susceptibility is a function of the applied electric field and can be written as

$$P(t) = \varepsilon_o \chi(E) E(t), \qquad (2.2)$$

where $\chi(E)$ can be expanded in a Taylor series as,

$$\chi(E) = \chi^{(1)} + \chi^{(2)}E(t) + \chi^{(3)}E^2(t) + \chi^{(4)}E^3(t) + \chi^{(5)}E^4(t) + \ldots\ldots \quad . \qquad (2.3)$$

The electrical susceptibility terms $\chi^{(n)}$ are in general tensors of order n and rank (n+1). Therefore, the nonlinear polarization can be written as

$$P(t) = \varepsilon_o(\chi^{(1)}E(t) + \chi^{(2)}E^2(t) + \chi^{(3)}E^3(t) + \chi^{(4)}E^4(t) + \chi^{(5)}E^5(t) + \ldots.), \qquad (2.4)$$

or

$$P(t) = (P^{(1)}(t) + P^{(2)}(t) + P^{(3)}(t) + P^{(4)}(t) + P^{(5)}(t) + \ldots.). \qquad (2.5)$$

Each of the terms is responsible for different nonlinear effects, and the most common ones are listed below.

$P = \varepsilon_o\chi^{(1)}:E$ {complex index of refraction

$+\varepsilon_o\chi^{(2)}:EE$ {second harmonic generation; sum and difference frequency generation; parametric flourescence; optical rectification

$+\varepsilon_o\chi^{(3)}:EEE$ {third harmonic generation; four photon parametric mixing; four photon parametric flourescence; nonlinear index of refaction; Raman scattering; two photon absorption

$+ \ldots.$

In addition to the terms listed above there are also higher order terms, and effective nonlinearities of a given order. We did not observe any significant amounts of higher order nonlinearities, except possibly in the case of the supercontinuum generation

experiment. Anyhow, the true higher order nonlinearities will not be discussed in this thesis. However, we were mildly concerned with the presence of an effective higher order nonlinearity, when performing our Z-Scan and PDM measurements. An effective high order nonlinearity is a nonlinearity that acts like a higher order nonlinearity, when in fact it is the combination of two lower order nonlinearities. The effective nonlinearity that we were most concerned with was that due to free carrier refraction. This is an effective $\chi^{(5)}$ effect, that is caused by Two Photon Absorption(2PA) followed by linear refraction(a $\chi^{(3)}$:$\chi^{(1)}$ effect). However, there are many possible combinations of lower χ effects that can cause effective higher order nonlinearities

In general, a tensor of order n contains 3^n terms in it, therefore using these tensors to relate the electrical polarization to the electrical fields may seem like a monumental undertaking. However, there are a great number of symmetry relations that reduce the number of nonredundant tensor terms. For instance, all materials that are centrosymmetric have no $\chi^{(2)}$ or any $\chi^{(2n)}$ terms. Additionally, for a given class of materials there are several terms that are always zero [1], [2], [3], [4].

2.2 Sum Frequency Generation

Both sum frequency generation and the more specific case of second harmonic generation are processes that depend upon the $\chi^{(2)}(\omega_1+\omega_3:\omega_1, \omega_3)$ of a material. These processes occur when two electric fields incident upon a noncentrosymmetric material are large enough to induce a nonlinear effect that causes a third field to be generated that has a frequency equal to the sum of the incident frequencies. While performing all of the pulse width measurements described in Chapter 5, we took advantage of the process of second harmonic generation so as to generate the second order autocorrelation functions with our autocorrelators. Furthermore, the manner in which we plan to measure the

properties of the supercontinuum laser source that we also discuss in Chapter 5, takes advantage of the related process of sum frequency generation in a cross correlation arrangement. For these processes to be efficient, the nonlinear crystal must be phased matched. Therefore, phase matching of a uniaxial crystal for the purpose of sum frequency generation will be mentioned, so that the manner by which the plots shown in Chapter 5 were generated is understood.

In general, sum frequency generation is the process where two beams of light incident upon a material combine to produce a third beam at a frequency that is the sum of that of the incident beams, so that

$$\omega_1 + \omega_2 = \omega_3, \qquad (2.6)$$

where ω_1, ω_2 and ω_3 are the angular frequencies of the two incident beams and the generated beam respectively. The intensity of the light generated by this process is

$$I_3 = I_3(\max)\frac{\sin^2(\Delta kL/2)}{(\Delta KL)^2}, \qquad (2.7)$$

where L is the interaction length of the material and Δk is the phase mismatch error. For efficient sum frequency generation, the phase mismatch error between the propagation constants

$$\Delta k = k_1 + k_2 - k_3 \qquad (2.8)$$

must be minimized, and this can only be obtained for collinear beams when

$$n_1\omega_1 + n_2\omega_2 = n_3\omega_3. \qquad (2.9)$$

However, due to the form of the dispersion curves for the refractive index of materials, both equations (2.6) and (2.9) cannot be met simultaneously in isotropic materials. However, in birefringent crystals, the index of refraction is dependent upon the polarization of the incident beams. Therefore, by manipulating the polarization of the

incident beams, the refractive index of the sum frequency generated light can be made equal to the refractive index of the incident fundamental beam. Hence, it is possible to meet both the conditions of equations (2.6) and (2.9) simultaneously, so that the phase matching conditions and efficient sum frequency generation will occur. Angle tuning will be used to obtain the phase matching conditions when performing the continuum characterization described in Chapter 5. Angle tuning involves a precise angular orientation of the crystal with respect to the propagation direction of the incident light, so that the refractive index of the extraordinary wave is altered to meet the phase matching conditions. This is most easily described for the case of a uniaxial crystal, which is characterized by a direction known as the optical axis. Light polarized perpendicularly to the direction of the propagation vector **k** and the optical axis is said to have an ordinary index of refraction n_o, whereas light in the plane of the **k** vector and the optical axis is said to see an extraordinary index of refraction $n_e(\theta)$. The extraordinary index of refraction depends upon its angle with respect to the optic axis and **k** in the following manner

$$\frac{1}{n_e(\theta)^2} = \frac{\sin^2\theta}{\bar{n}_e^2} + \frac{\cos^2\theta}{\bar{n}_o^2}. \qquad (2.10)$$

The refractive index of the extraordinary wave $n_e(\theta)$, equals the principle value $\bar{n}_e$ for θ=90 degrees and $\bar{n}_o$ the ordinary wave index for θ=0. Hence, the angle θ is varied so that the refractive index of the extraordinary wave matches the conditions necessary to satisfy both equations (2.6) and (2.9). This is achieved by either Type I or Type II phase matching, where the incident fields have polarizations that are parallel and perpendicular to each other respectively. A uniaxial crystal is called a positive or negative crystal, depending on whether or not the extraordinary refractive index is greater than or less than that of the ordinary refractive index for each possible wavelength. Therefore, it is clear

from its dispersion curves in Chapter 5, that KDP is a negative uniaxial crystal. Therefore, Type I phase matching is achieved with the incident beams incident as extraordinary waves, and the two variations of Type II phase matching occur when one incident beam is incident as an ordinary and the other as an extraordinary wave. In all three cases, the generated beam is an ordinary wave. Similarly, the exact opposite holds true for a positive uniaxial crystal [1], [5], and [6].

The plots shown in Chapter 5 were obtained by plugging in $n_e(\theta)$ from equation (2.10) into equation (2.9) and then letting the first frequency be that of the 850 nm pump beam, and the second frequency be that of the white light continuum. Then, the frequency of the generated frequency was calculated for the given continuum wavelength, and n_o and n_e were obtained for the given frequencies through the use of the Seillmier equation. Finally, the value of θ that would satisfy equation (2.9) was numerically solved for, and then the continuum wavelength was altered in small increments as the whole process was repeated over the entire spectrum. It is important to note that the θ listed is the internal angle, and that the crystal must be rotated by a greater amount than this as determined by Snell's law ($n_1\sin\theta_1=n_2\sin\theta_2$) for the phase matching conditions to hold.

2.3 Nonlinear Absorption and Refraction

Just as the real and imaginary parts of $\chi^{(1)}$ are responsible for linear refraction and linear absorption, the real and imaginary parts of $\chi^{(3)}$ are responsible for cubic nonlinear refraction and two photon absorption(2PA) present in materials. In terms of the nonlinear susceptibility [7]

$$\beta = \frac{\omega}{2n_o^2\varepsilon_o c^2}\mathrm{Im}\left[\chi^{(3)}\right] \qquad (2.11)$$

and

$$\gamma = \frac{\mathrm{Re}\left[\chi^{(3)}\right]}{2n_o^2 \varepsilon_o c^2}. \qquad (2.12)$$

These two nonlinear effects are both irradiance dependent, whereas linear absorption and refraction are independent of incident light intensity. The electronic nonlinear refractive index, n_2 and 2PA coefficient β, are the material parameters that we have set out to measure with the Z-scan, Pulse Delay Modulation Technique(PDMT) and Pulse Delay Modulated(PDM) Z-scan.

Two photon absorption (2PA) is a process whereby an atom makes a transition from the ground state to a higher state through the simultaneous absorption of two photons with energies less than the band gap, but greater than half the bandgap. **Figure** (2.1) shows an example of this process, where the incident photon energy is approximately half the band gap energy [1].

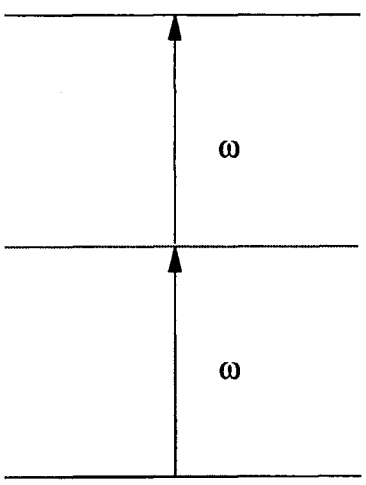

Figure 2.1 Two Photon Absorption.

In general the nonlinear refractive index can be written as

$$\Delta n = \gamma I + \sigma_r N \qquad (2.13)$$
$$= \frac{n_2}{2}|E|^2 + \sigma_r N.$$

Where σ_r is the change in the index of refraction per unit photoexcited charge-carrier density N, and $\gamma(m^2/W)$ is the nonlinear index of refraction that is due to bound electrons, such that

$$n_2(esu) = (cn_o / 40\pi)\gamma(m^2/W), \qquad (2.14)$$

where c is the speed of light in meters per second, n_o is the linear refractive index and ε_o is the permittivity of free space. Additionally, if 2PA is the significant mechanism responsible for the generation of free carriers, the carrier generation rate is given by

$$\frac{dN}{dt} = \frac{\beta I^2}{2\hbar\omega}. \qquad (2.15)$$

The free carrier nonlinearity $\sigma_r N$ is proportional to a temporal integral of I^2 that results in a effective fifth order nonlinearity ; hence

$$\Delta n = \gamma I + C\sigma I^2, \qquad (2.16)$$

where

$$C = 0.1145\frac{\beta t_o}{\hbar\omega}\left[1+\exp(\alpha_o L)\right], \qquad (2.17)$$

α_o is the linear absorption, and t_o is the pulse width [7]. We wanted to compare the magnitude of the refraction due to free carriers generated from two photon absorption with that of those from bound electronic nonlinearities, so as to determine whether the magnitude of the free carrier refraction was significant in our ZnSe sample. This was done by using $\sigma_r = -1\times10^{-21}$ cm^3, which was about twice the theoretical value of -4.4×10^{-22} cm^3 as obtained with

$$\sigma_r = A\frac{E_p}{n_o E_g^3} H\left(\frac{\hbar\omega_p}{E_g}\right). \qquad (2.18)$$

This equation is given by Wang et al. [8], where E_p is the nearly material independent Kane energy of 21 eV, $H(x)=[x^2(x^2-1)]^{-1}$ is the free carrier dispersion function, $A = 2\pi\hbar^2 e^2 / m_o = 3.4\times10^{-22}\,cm^3eV^2$, E_g is the energy gap of the material (2.67 eV for ZnSe), and $\hbar\omega_p$ is the energy of the probe photon. We then compared the first term of equation (2.13) to the second term for our highest energy pulse of irradiance of 1.8173 $\times10^3$ GW/cm^2 whose pulse width was 168 fs FWHM at 780 nm. The values of β=4.5 cm^2/GW and $\alpha_o = 0$ were used. As a result, we found that the free carrier term was still about twenty times smaller than that of the bound electronic nonlinear refraction term. Therefore, we ignored the possibility of free carrier refraction being present in our analysis, and our experimental results gave no indication to the contrary. However, there remains the possibility that long term or cumulative effects are present.

REFERENCES FOR CHAPTER 2

[1] R. W. Boyd Nonlinear Optics, Academic Press Inc., San Diego, 1992.

[2] P. N. Butcher, and D. Cotter, The Elements of Nonlinear Optics, Cambridge University Press, Cambridge, 1990.

[3] D. H. Auston, "Picosecond Nonlinear Optics," in Ultrashort Light Pulses: Picosecond Techniques and Applications, (S. L. Shapiro, ed.) Springer-Verlag, New York, 1977.

[4] D. R. Lovett, Tensor Properties of Crystals, Adam Hilger, Bristol, 1990

[5] A. Yariv, Optical Electronics, 3rd ed., Holt Rinehart and Winston, Orlando, 1985.

[6] A. Yariv, Quantum Electronics, 3rd ed., John Wiley and Sons, New York, 1989.

[7] A. A. Said, "Development and Application of a Nonlinear Optical Characterization Technique", Phd. Diss., University of North Texas, Denton, TX, 1991

[8] J. Wang, M. Sheik-Bahae, A. A. Said, D. J. Hagan, E. W. Van Stryland, "Time-resolved Z-scan measurements of optical nonlinearities," *J. Opt. Soc. Am. B* **11**, 1-9 (1994).

CHAPTER 3

LASER SYSTEMS AND PULSE PROPAGATION

For our material characterization experiments an argon pumped Ti:sapphire was used as the light source. Additionally, the Ti:sapphire laser was the oscillator for a LiSAF regenerative amplifier, when we performed the grating compression and single shot autocorrelation measurements as a part of the Ultrafast Supercontinuum Laser Source (USLS) development. In addition to describing both of the laser systems, we will discuss the propagation of high intensity ultrashort pulses through dispersive nonlinear media.

3-1 Pulse Propagation

Various material dependent effects, such as Self-Phase-Modulation (SPM), self-focusing, dispersion, and Group Velocity Dispersion(GVD) have a large impact upon the propagation of high intensity and/or broadband laser pulses. These effects will be introduced, so that the compression techniques we implemented as well as the operation of the Ti:sapphire can be better understood.

3.1.1 Chirp

A pulse is said to be "chirped", when all the frequency components within the pulse are not temporally coincident. Therefore, a chirped pulse will have the same energy as its unchirped counterpart, however its power or irradiance(w/cm^2) is diminished. Consequently, the chirping of a pulse can be quite detrimental to the initiation of

nonlinear interactions, where the highest intensity possible is wanted. On the other hand, a chirped pulse may be desirable for amplification purposes, or for pulsed radar applications. In high intensity optical pulses, chirp can be caused by Self Phase Modulation(SPM), Group Velocity Dispersion(GVD), frequency dependent geometrical path differences, or any combination of the three, where frequency dependent path differences will be discussed in Chapter 4 and SPM and GVD will be discussed later in this chapter.

Chirp due to dispersion is always present in any optical medium, and just temporally redistributes the frequencies in a pulse. Normal, or positive, dispersion in materials causes an "up-chirp" meaning that there is a time delay of the higher frequencies with respect to the lower frequencies. Similarly, "down chirp" is caused by a negative, or anomalous, dispersion and the lower frequencies are delayed with respect to the higher ones. Both of these forms of chirp can be seen in **Figure** (3.1). Since, we are dealing with short pulsed laser beams that have a large bandwidth, the chirp due to material dispersion can become very significant.

The other two processes, just alter the delay in time of frequency components relative to each other. SPM is a nonlinear optical process that creates new frequencies when a high intensity pulse passes through a material with a sufficiently large nonlinear index of refraction (n_2). For a positive n_2, these new frequency components are created so that the pulse displays a positive chirp. A pulse that is chirped by SPM may appear similar to one chirped by dispersion spatially, however it is a nonlinear process that generates new frequencies so the frequency spectrum is actually broadened. These new frequency components broaden the spectrum, so that compensating for the chirp will actually create shorter pulses than would be possible without any nonlinear process.

a)

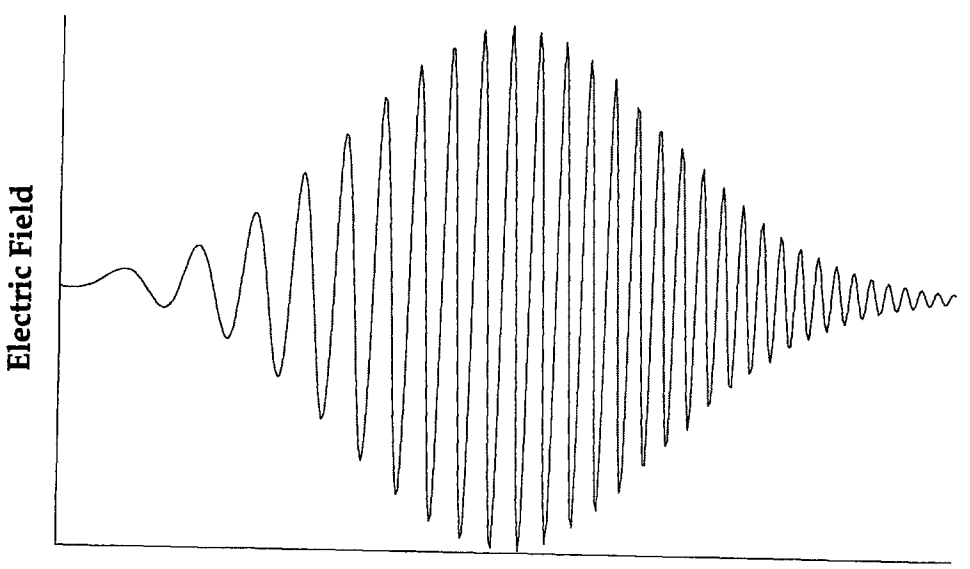

b)

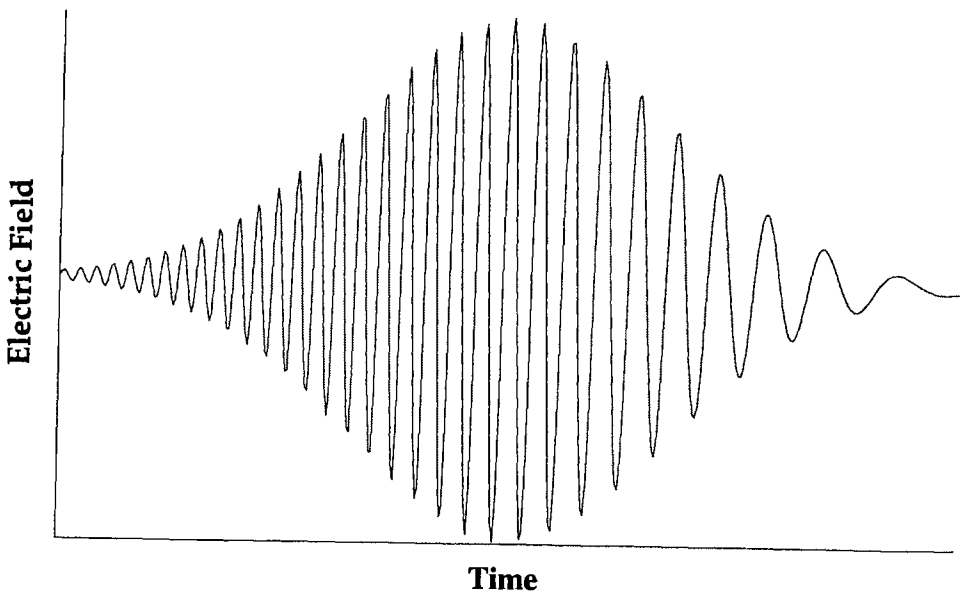

Figure 3.1 Electric field vs. time for a) Up-chirped pulse b) Down-chirped pulse.

Geometrical dispersion occurs when two different wavelength components of a pulse are delayed with respect to each other because they traveled a different geometrical path. Both positive and negative chirp can be added to a pulse by this method, whereas only positive chirp is usually added by material dispersion and SPM. In fact, the grating and prism pulse compression techniques that we will discuss, are based upon the introduction of dispersion caused by frequency dependent geometrical path differences.

3.1.2 Group Velocity vs. Phase Velocity

The existence of both dispersion and group velocity dispersion are both due to the fact that there are no materials that have a constant refractive index for all wavelengths. Atoms with orbiting electrons have resonances that absorb light at certain frequencies, therefore from the Kramers-Kronig relation, dispersion of the refractive index occurs. Since, the speed at which an optical wave traverses a given material is dependent upon the index of refraction of that material, the velocity of light is also a function of wavelength. Such that

$$v(\lambda) = \frac{c}{n(\lambda)}, \qquad (3.1)$$

where λ is the wavelength, and c is the speed of light in a vacuum. The dispersion of refractive index $n(\lambda)$, for various materials will be given later in this chapter and in Chapter 5. In most optical materials, the refractive index increases as the frequency increases or the wavelength becomes shorter, because they have a resonance frequency in the ultraviolet.

Phase velocity is a mathematical concept that only applies to an ideal optical wave with one frequency whose frequency spectrum is a δ function. However, even the most monochromatic light sources are made up of more than one frequency, because the atomic transitions that generate the light have a finite bandwidth. When dealing with

more than one wavelength of light, the group velocity of the light must be considered in addition to the phase velocity.

In the case where there are two or more wavelengths of light propagating in a medium the group velocity, v_g is more physically meaningful. The group velocity represents the speed of the energy flow of the packet of waves, and the group velocity can be more directly measured than the phase velocity. For example, consider the case where there are two light waves of different frequencies in a dispersive medium that are given by

$$E_1(x,t) = E_0 \cos(k_1 x - \omega_1 t) \tag{3.2}$$

and

$$E_2(x,t) = E_0 \cos(k_2 x - \omega_2 t) \tag{3.3}$$

respectively. By adding them together we obtain

$$E_{tot}(x,t) = E_{01}\left[\cos(k_1 x - \omega_1 t) + \cos(k_2 x - \omega_2 t)\right], \tag{3.4}$$

which after some algebra and trigonometric manipulation can be written as

$$E_{tot}(x,t) = 2E_0 \cos(k_m x - \omega_m t)\cos(\bar{k}x - \bar{\omega}t). \tag{3.5}$$

Here,

$$k_m = \frac{k_1 - k_2}{2}, \tag{3.6}$$

$$\omega_m = \frac{\omega_1 - \omega_2}{2}, \tag{3.7}$$

$$\bar{k} = \frac{k_1 + k_2}{2}, \tag{3.8}$$

and

$$\bar{\omega} = \frac{\omega_1 + \omega_2}{2}, \tag{3.9}$$

where in (3.5), the second term is the high frequency carrier oscillation and the first term represents the energy envelope. The phase velocity, v_p, is the speed at which the high frequency carrier oscillations must travel so as to keep a constant phase front, where the phase front is given by

$$\phi(x,t) = \bar{k}x - \bar{\omega}t. \qquad (3.10)$$

Therefore, for the phase front to be constant, the change in phase with respect to time must equal zero at a set position. Hence,

$$\frac{\partial \phi}{\partial t} = \bar{k}\frac{\partial x}{\partial t} - \bar{\omega} = 0, \qquad (3.11)$$

and the phase velocity is given by

$$v_p = \frac{\partial x}{\partial t} = \frac{\bar{\omega}}{\bar{k}}. \qquad (3.12)$$

Now, this phase velocity is only equal to equation (3.1) when light is monochromatic or propagating in a vacuum. In fact, when more than one frequency is moving in a dispersive medium the phase velocity can be greater than the speed of light and is not really physically meaningful. The first term represents the energy envelope, and by setting its phase equal to a constant we can solve for the group velocity just as we solved for the phase velocity earlier. So that

$$v_g = \frac{\omega_m}{k_m}, \qquad (3.13)$$

and with a little manipulation we obtain

$$v_g = \frac{\omega_1 - \omega_2}{k_1 - k_2} = \frac{\Delta\omega}{\Delta k}. \qquad (3.14)$$

Now, the function $\omega = \omega(k)$ is called a dispersion relation, and if (3.14) is small enough it can be written as a derivative. Therefore, by using ω=kc, we can represent the group velocity as

$$v_g = v_p\left(1 - \frac{k}{n}\frac{dn}{dk}\right), \qquad (3.15)$$

which is just one of many possible useful forms. Now, from (3.15), and (3.1) we can also obtain n_g which is the group index of refraction. In general, one would say that the group velocity could be equal to, less than or greater than c/n. However, (3.15) does not cause relativistic laws to be broken, because at optical frequencies in regions of normal dispersion, the refractive index increases with frequency. The refractive index of fused silica is a typical example of this and is shown in **Figure** (3.2) as a function of

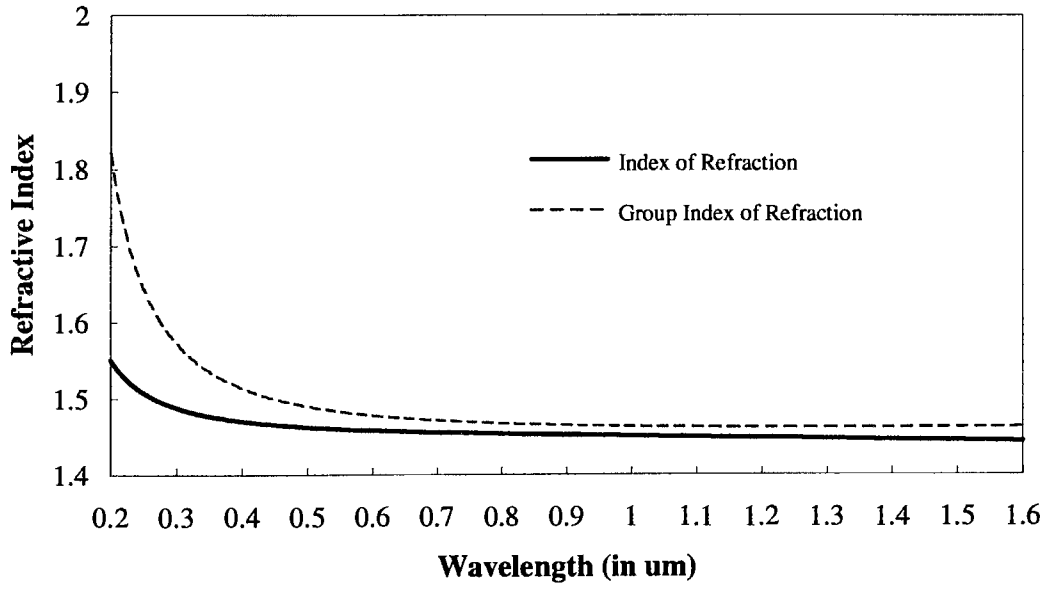

Figure 3.2 Dispersion of refractive index and group refractive index for fused silica.

wavelength. Where, $dn/d\lambda < 0$, hence $dn/dk > 0$, and the group velocity is always less than or equal to(in the case of zero dispersion or monochromatic waves) the speed of light [1].

3.1.3 Group Velocity Dispersion(GVD)

As shown above, the group velocity describes the speed at which an envelope of polychromatic pulses travels in a dispersive medium, and the Group Velocity Dispersion (GVD) is the change in the group velocity with respect to wavelength. Whereas, the group velocity is proportional to the derivative of the optical path length with respect to wavelength, the Group velocity dispersion is proportional to the second derivative of the optical path length with respect to the wavelength. The effects of dispersion can be represented by expanding the propagation constant

$$\beta(\omega) = \frac{\omega}{c} \tag{3.16}$$

in a narrow band about the central frequency ω_o as

$$\beta(\omega) = \beta(\omega_o) + \beta'(\omega_o) \times (\omega - \omega_o) + \frac{1}{2}\beta''(\omega_o) \times (\omega - \omega_o)^2. \tag{3.17}$$

Here, the coefficients in the power series expansion of $\beta(\omega)$ are

$$\beta \equiv \beta(\omega)|_{\omega=\omega_o} = \frac{\omega_o}{v(\omega_o)} \equiv \frac{\omega_o}{\text{phase velocity}}$$

$$\beta' \equiv \left.\frac{\partial\beta}{\partial\omega}\right|_{\omega=\omega_o} = \frac{\omega_o}{v_g(\omega_o)} \equiv \frac{\omega_o}{\text{group velocity}} \tag{3.18}$$

$$\beta'' \equiv \left.\frac{\partial^2\beta}{\partial\omega^2}\right|_{\omega=\omega_o} = \left.\frac{\partial}{\partial\omega}\left(\frac{\omega_o}{v_g(\omega)}\right)\right|_{\omega=\omega_o} \equiv \quad \text{GVD.}$$

3.1.4 Self Phase Modulation

Self Phase Modulation (SPM) is a process whereby a high intensity laser pulse that passes through a medium generates new frequency components. This phenomena is very important in many areas of nonlinear optics, nonlinear fiber optics, and ultrafast pulse generation, including continuum generation.

To start with, lets look at the E field equation for a general pulse

$$\tilde{E}(z,t) = \left[E_o(z,t)e^{i(\omega_o t - kz)} + c.c.\right] \qquad (3.19)$$

Now, if the electric field of this pulse is sufficiently large, then it can produce a nonlinear index change in the medium. Therefore, we can write the index of refraction as

$$n(t) = n_o + n_2 I(t), \qquad (3.20)$$

where

$$\phi(t) = \omega_o t - kz \qquad (3.21)$$

and

$$k = \frac{n\omega_o}{c}. \qquad (3.22)$$

Over a sample of length L, the pulse then experiences a time varying phase shift of

$$\phi_{NL}(t) = [-n_2 I(t)\omega_o L]/c. \qquad (3.23)$$

So, if we look at the instantaneous frequency, we see that

$$\omega_i(t) = \omega_o + \frac{d}{dt}\phi_{NL}(t) \qquad (3.24)$$

is dependent on the derivative of this nonlinear phase, which is in turn dependent on the shape and intensity of the pulse through the derivative of I(t). As an example of this phenomenon, I will use a pulse with the form of

$$I(t) = I_o \operatorname{sech}^2\left(\frac{t}{\tau_o}\right), \qquad (3.25)$$

which is a soliton like pulse and the output pulse shape emitted from our Ti:sapphire oscillator. From this pulse shape and (3.23), we can see that the nonlinear phase shift is given by

$$\phi_{NL}(t) = -n_2 \frac{\omega_0}{c} LI_o \operatorname{sech}^2(\frac{t}{\tau_o}). \qquad (3.26)$$

Then from equation (3.24), the instantaneous frequency can be given by

$$\omega_i(t) = \omega_o + 2n_2 \frac{\omega_o}{c\tau_o} LI_o \operatorname{sech}^2(\frac{t}{\tau_o}) \tanh(\frac{t}{\tau_o}). \qquad (3.27)$$

Therefore, for a positive nonlinear index of refraction, the change in frequency is negative on the leading edge of the pulse and positive on the trailing edge as is shown in **Figure** (3.3). Since, the higher frequencies lag behind the lower frequencies, the pulse then displays a positive chirp.

The maximum value of the frequency shift is around

$$\delta\omega_{max} \cong \frac{\Delta\phi_{NL}^{max}}{\tau_o}, \qquad (3.28)$$

where

$$\Delta\phi_{NL}^{max} \cong n_2 \frac{\omega_o}{c} I_o L. \qquad (3.29)$$

As a general rule, the spectral broadening due to SPM is only considered important when it exceeds the initial spectral pulse width. For a smooth pulse this is approximately $1/\tau_o$, hence SPM is usually only important when $\Delta\phi_{NL}^{max} \geq 2\pi$ [2] ,[3].

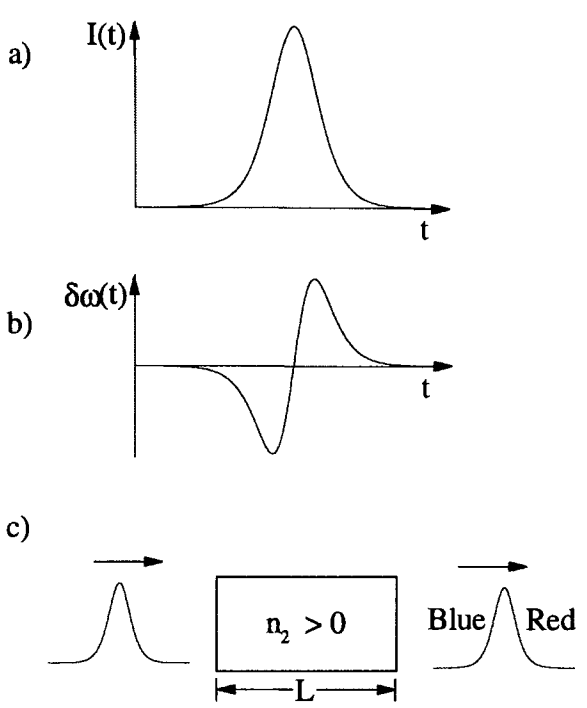

Figure 3.3 Self Phase Modulation a) Time dependence of the incident pulse. b) Change in the instantaneous frequency of the transmitted pulse. c) Manner by which SPM would be observed experimentally.

3.1.5 Self Focusing

Self focusing is a form of self action where an intense beam of light alters the index of a medium, through a positive nonlinear index of refraction n_2. Self focusing can be thought of as the spatial counterpart to the temporal self phase modulation. In fact, the spatial effects of n_2 on the propagation of Gaussian beams has been used to develop the Closed Aperture Z-scan, which will be discussed in Chapter 7. Additionally, self-focusing is very important in creating the ultrashort pulses in the Ti:sapphire laser through the process of KLM, which will be discussed later in this Chapter.

Single mode laser pulses have an approximately Gaussian spatial profile. Therefore, the intensity of the pulse is greater towards the center, hence the index of refraction as given by equation (3.20) is also greater towards the center of the beam. If $n_2 I$ is greater than the diffraction spreading through a given length, this effect will be significant. Therefore the material will appear to have a larger optical path length towards the center, and a plane parallel piece of optical material will act as a weak positive lens. See **Figure** (3.4) for a demonstration of this effect. As n_2 occurs in all materials, an intense beam propagating

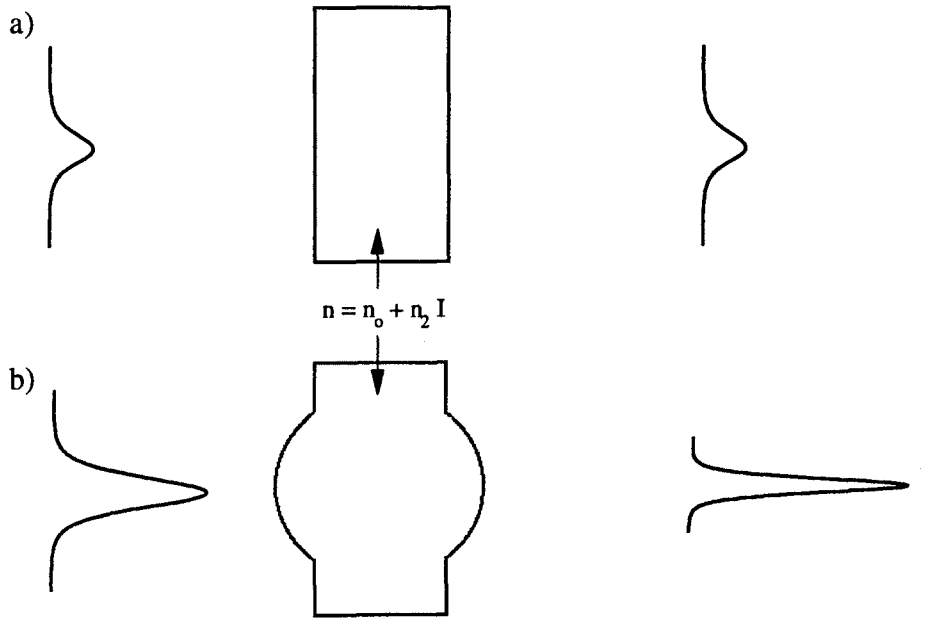

Figure 3.4 a) Low intensity pulse whose intensity profile is not effected by self-focusing b) High intensity pulse that is self-focused, so that it is spatially compressed with the same total energy.

through an amplifier will experience self focusing and SPM which can lower the quality of the beam and even cause catastrophic damage to the laser medium. Therefore, the B integral

$$B = \frac{2\pi}{\lambda} \int_0^L n_2 I(z) dz \qquad (3.30)$$

is a figure of merit for the self focusing effects in a given system, where generally B should be kept less than 3-5 to avoid problems.

3.1.6 Distortion in Lenses

It has already been stated that nonlinear effects such as SPM and dispersion can in some cases not only distort, but significantly stretch the ultrashort pulses of a laser. However, when ultrashort pulses pass through a lens or lens system, the pulse distortion due to GVD in the lens material may be small compared to the distortion caused by the Propagation Time Differences (PTD). PTD is the pulse front distortion that occurs, because of the difference in the phase and group velocities of the pulse as it passes through the lens or lens system. These effects have been derived by both geometrical [4] and Fourier optical [5] methods, and have been experimentally verified [6], [7]. The amount of temporal and spatial distortion caused by the PTD is determined mainly by the chromatic and spherical aberration of the lens. This error can be reduced by using an achromatic doublet that has been corrected for the region of the spectrum where the laser operates. An achromat will slightly increase the GVD of the lens. But, that can be corrected for with a grating compression system, whereas the distortion due to PTD cannot. These effects are only significant when using femtosecond pulses, and the wavelength times the dispersion is large relative to the GVD. It turns out that this occurs only when high frequencies that are near the resonant frequency of the material are used,

unless the pulse has an extremely large bandwidth. Therefore, the distortion due to these effects should not be much larger than that from GVD for the 100 fs 850 nm pulses that we used. However, for shorter pulses, and especially with any white light continuum pulses, these effects will be large [8].

3.2 Ti:sapphire Oscillator

We will discuss the general characteristics of the Ti:sapphire laser, as well as the specifics of the one used in our experimental set-up. Furthermore, Kerr Lens Modelocking(KLM) is the process by which the Ti:sapphire laser is able to generate femtosecond pulses. Therefore, modelocking, KLM, and the nonlinear processes involved in KLM will be discussed. Additionally, modelocking will be reviewed, along with the Kerr lens modelocking process which is responsible for the generation of femtosecond pulses.

3.2.1 Overview of Ti:sapphire

The oscillator that was used in all of our experiments was a laser based upon a titanium doped crystal(Ti:sapphire), which is a tunable vibronic solid state laser. Similar to organic dye lasers, the Ti:sapphire laser operates upon vibronic transitions, where the titanium impurity ion displaces an aluminum atom in the sapphire host. This impurity in the solid host induces changes in both the vibrational and electronic states much like organic dyes do in solution Additionally, much like organic dye lasers, the Ti:sapphire laser is tunable over a wide frequency range, hence capable of ultrashort pulses. In fact. the Ti:sapphire laser is capable of a broader tuning range than any single solid state, gas or liquid laser medium, yet it still has the stability and ease of use that many other solid state lasers possess. This relative ease of use along with its wide tunability, ultrashort pulse width capability and hence high peak powers is why we are using the Ti:sapphire

laser. Furthermore, although Ti:sapphire lasers are usually pumped with argon ion lasers or frequency doubled YAG lasers, there are flashlamp and diode pumping schemes being developed.

The Ti:sapphire is readily tunable with its highest output power for wavelengths between 700 and 900 nm, but with the proper choice of mirrors it can be tuned from 660 to 1180 nm. Additionally, commercial Ti:sapphire lasers produce several watts of power when operated in the cw mode, and they can produce more than a watt when cw modelocked. In fact, the Ti:sapphire laser's ability to be Kerr lens modelocked has made it possible for researchers to generate pulse widths as short as 11 femtoseconds with intracavity dispersion compensation.[9], [10]. However, pulse widths in the 70-100 femtosecond range are more commonly available. Its broad bandwidth and high peak powers allow Ti:sapphire lasers to effectively generate second harmonic at 350-470 nm, third harmonic at 235- 300 nm, and fourth harmonic around 210 nm. Therefore, the Ti:sapphire can cover a wide region of the visible spectrum as well as the near infrared region.

The following figure of merit has been introduced so as to help compare the suitability of different active materials for mode locked lasers:

$$M = \sigma \tau \Delta\nu, \qquad (3.31)$$

where σ is the peak cross emission cross section, τ represents the lifetime of the metastable level, and $\Delta\nu$ is the width of the fluorescence line(FWHM). A larger $\sigma\tau$ makes for easier pumping, whereas a broader fluorescence line width allows for the generation of shorter pulses and a broader tuning range. **Table** (3.1) shows this figure of merit as well as several relevant spectroscopic parameters for both the lasing materials that we used, as well as several other common ones for comparison.

Table 3.1
Spectroscopic parameters of laser materials for ultrashort optical pulse generation [11].

	Rh6G	Nd:YLF	Nd:glass	Ti:sapphire	Cr:LiSAF
Peak emission cross section (10^{-20} cm^2)	2×10^4	18	4.2	30	4.8
Gain bandwidth (cm^{-1})	1500	12	200	3200	1900
Fluorescence peak (μm)	0.6	1.047	1.053	0.78	0.83
Upper state lifetime (μs)	0.005	480	350	3.2	67
Figure of Merit M (10^{-21} cm^2s)	1.5	1.0	2.9	3.1	6.1

3.2.2 Ti:sapphire Setup

The laser oscillator that we used was a pulsed Ti:sapphire laser in an X-configuration that was pumped by a continuous wave(cw) argon ion laser. The argon pump laser was a Laser Ionics Inc. model 1400-12A with an emergent beam diameter of 1.8 mm, beam divergence of .4 mRad, and a maximum output of 15 watts cw. The argon has several bands of output wavelengths in the ultraviolet between 275.4 nm and 358.8 nm, as well as output at 25 visible wavelengths between 408.9 nm and 686.1 nm. The dominant wavelengths are between 488.0 nm and 514.5 nm, which is right in the center of the 400 nm to 600 nm absorption band for Ti:sapphire.[12], [13], [14].

The Ti:sapphire laser was set up in an X-cavity, which is a cavity design that was originally used with femtosecond dye lasers[15]. The entire set up is shown in **Figure** (3.5). The astigmatism created by using the mirrors in the cavity at an angle corrects for the astigmatism created by the crystal which is cut at Brewster's angle. There are two slits within the cavity, one near the output coupler to induce modelocking, and one near

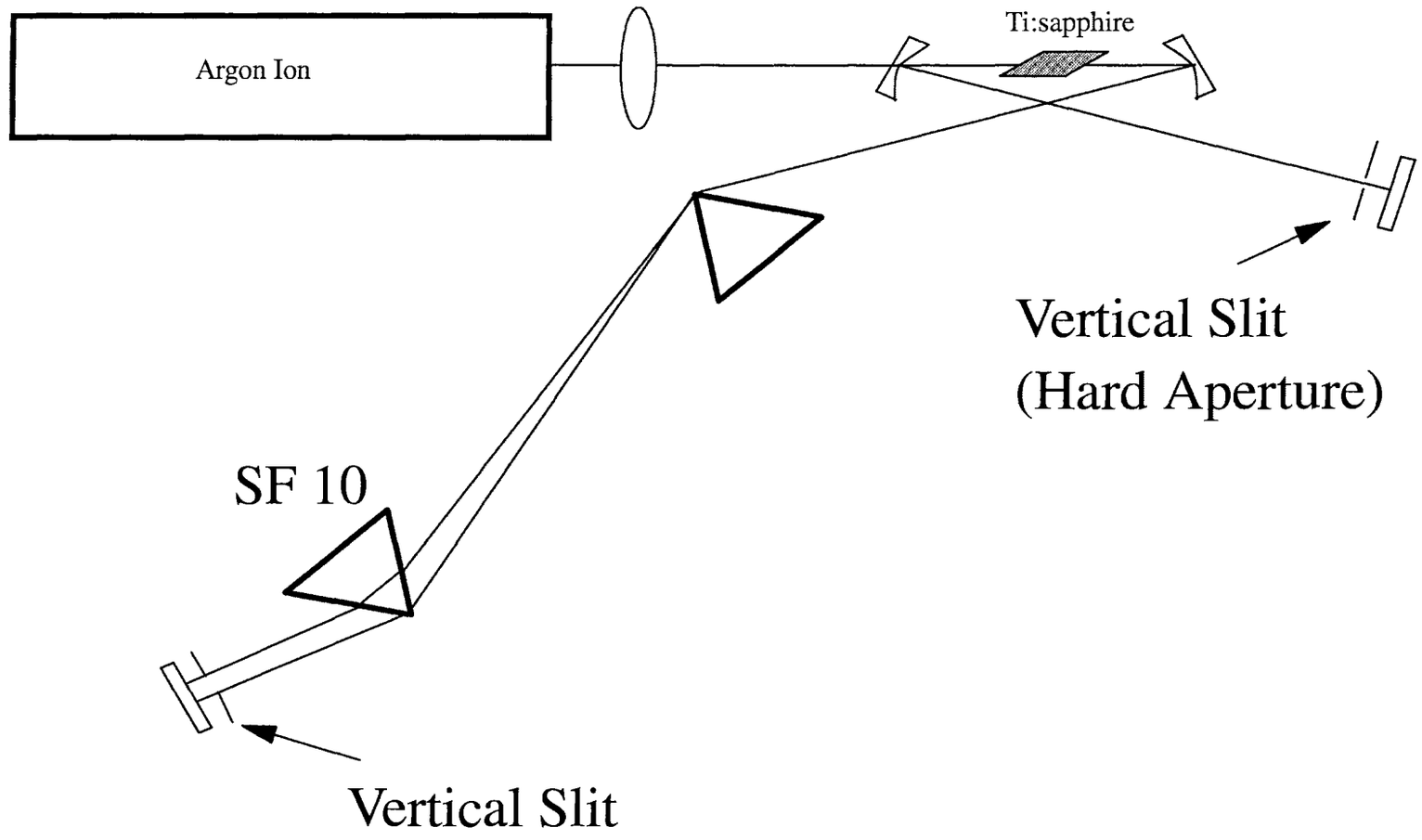

Figure 3.5 Ti:sapphire laser

the back mirror so as to stabilize the system and adjust its wavelength. The prisms that we used were made out of SF10 glass, and were separated by about 40 cm, and the Ti:sapphire crystal was about 7mm long

For the material measurement experiments the Ti:sapphire laser was run at 780 nm, which is at the peak fluorescence wavelength. We did not actually choose this wavelength ahead of time, rather it was the wavelength at which the modelocking was the most stable. This is near the wavelength region of maximum laser output, and 780 nm is the peak fluorescence wavelength of Ti:sapphire. On the other hand, the Ti:sapphire laser was operated at 850 nm when used as an oscillator for the LiSAF amplifier. The Ti:sapphire needed to be near that wavelength, because the entire amplification system was designed for 850 nm, which is near the maximum laser gain of the LiSAF crystal. Still, both of these wavelengths are well within the Ti:sapphire's optimal lasing range which is 700 - 900 nm, and we regularly obtained pulses from 80 - 170 femtoseconds Full Width at Half Maximum(FWHM) [16].

3.2.3 Modelocking

An optical resonator which is a Fabry Perot cavity can support oscillations at the frequencies given by

$$\upsilon_m = \frac{mc}{2nL}, \qquad (3.32)$$

where m is an integer, c is the speed of light and n L represents the optical path length through the cavity. Of course, these frequencies can only support oscillation if there is sufficient gain to overcome the losses at those frequencies. In **Figure** (3.5), we see an example of the modes within the cavity of an inhomogeneously broadened laser that see enough gain to oscillate.

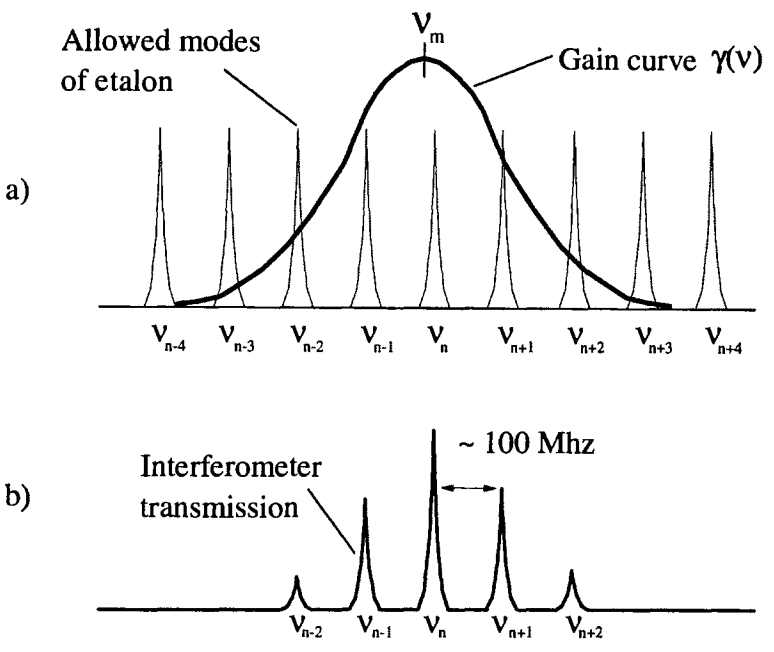

Figure 3.6 a) Inhomogeneously broadened gain curve with position of longitudinal-mode frequencies. b) Intensity versus frequency profile, where only five of the modes have sufficient gain to oscillate.

The optical electrical field that results from multimode operation can be represented at a given point by the superposition of these fields

$$e(t) = \sum_n E_n \exp\{i[(\omega_o + n\omega_{ax})t + \phi_n]\}. \qquad (3.33)$$

Here, the summation is taken over all m modes, where ω_o is the reference frequency $\omega_{ax} = \pi c / nL$, and ϕ_n is the phase of the nth mode. It can be shown that the total electric field is periodic, so that

$$e(t) = E(t + T), \qquad (3.34)$$

if the ϕ_n are made equal the round trip time of the resonator $T=2\pi/\omega_{ax} = 2L/c$.

If the phase ϕ_n is random, then the intensity of the laser output will fluctuate randomly. Therefore, the laser would not be useful in applications were coherence is

important. However, locking the relative phases or prohibiting all but one of the axial modes from oscillating will ensure coherence. Modelocking occurs when all n modes are locked together with the exact same phase.

If we look at the case where all the modes have equal amplitudes(E_n =1) and the phases are all equal to zero(ϕ_n=0), the representation for the electrical field from equation (3.32) becomes

$$e(t) = \sum_n \exp\{i(\omega_o + n\omega_{ax})t\}. \tag{3.35}$$

Which, after some manipulation can be rewritten as

$$e(t) = \exp(i\omega_o t)\frac{\sin(N\omega_{ax}t/2)}{\sin(\omega t_{ax}/2)}. \tag{3.36}$$

Therefore, the laser output power P(t), which is proportional to e(t)e*(t) is given by

$$P(t) \propto \frac{\sin^2(N\omega_{ax}t/2)}{\sin^2(\omega_{ax}t/2)}, \tag{3.37}$$

where N is the total number of modes. Hence, the power is emitted in a series of pulses with a period equal to the round trip time of the cavity ($T = 2\pi/\omega_{ax}$=2L/c), so that the peak power is equal to N times the average power.

$$P_{peak} = N \times P_{average}. \tag{3.38}$$

Furthermore, the pulse width can be estimated by

$$\tau_p = T/N \tag{3.39}$$

which can then give an indication of the number of modes in the cavity, where the number of modes oscillating is approximately

$$N \cong \Delta\omega/\omega_{ax}. \tag{3.40}$$

So, if the linewidth $\Delta\omega$ is known, equation (3.40) can be used to obtain the approximate temporal pulse width

$$\tau_p \cong \frac{2\pi}{\Delta\omega} \cong \frac{1}{\Delta\upsilon}. \qquad (3.41)$$

Therefore, the length of the shortest possible modelocked pulse is inversely proportional to the gain linewidth of the laser, where the constant of proportionality depends on the actual pulse shape. Hence, dye lasers and solid state lasers like Ti:sapphire and Cr:LiSAF that have the largest gain linewidths are theoretically capable of producing the shortest pulses [17], [18], [19].

3.2.4 Kerr Lens Modelocking

It has long been known that when high intensity light propagates through an optical medium with a positive nonlinear index of refraction then self focusing occurs. This self focusing in Ti:sapphire leads to a change in the position and size of the resonator mode [20]. The higher power modes are focused more by the Kerr effect than the lower power cw operation. Hence, by aperturing(ie, controlling the spatial gain profile) or using a slit, a power dependent loss can be added into the system. Higher power and shorter pulses are encouraged to oscillate over the lower power cw modes by properly positioning the aperture or slit. This aperturing acts as an equivalent ultrafast saturable absorber. However, this process is often not self starting, so that there must be an initial noise spike added to the system to initiate the process. In our set up we achieve this by placing the output coupler on a translation stage which is free to move in the direction of the beam, and is actually shaken by a speaker until modelocking occurs.

To achieve the 100 femtosecond pulse widths that are commonly observed there must be compensation for the GVD and SPM of the Ti:sapphire crystal. This is performed with a pair of prisms as described in Chapter 4, where the positive chirp induced by the crystal is canceled by the negative GVD of the prism set up [21].

3.3 LiSAF Amplifier

The 90 femtosecond 850 nm output pulse of the Ti:sapphire is amplified from 5 nJ per pulse to about 1 mJ through the use of a Cr:LiSAF regenerative amplifier. This amplification is performed by utilizing a technique called Chirped Pulse Amplification (CPA), which was actually originally developed for use with radar amplifiers. CPA is performed by expanding the incident pulse in time so that the pulse can be amplified to a greater power without damaging the amplifier, where the major concern is nonlinear self focusing although other nonlinear processes, saturation effects and forms of distortion are also reduced.

3.3.1 Cr:LiSAF

Cr:LiSAF is chosen as the crystal for the amplifier, because it has a broad emission bandwidth which extends from 780 nm to 1010 nm, so that it is broadly tunable and capable of supporting ultrashort pulses. Additionally, its absorption band and spontaneous emission lifetime of 67 μs are compatible with conventional flashlamp pumping. Since, this high gain crystal (σ = 1900 cm^{-1}) is now available in high optical quality laser rods, it makes an ideal candidate for a laser amplification material [22], [23], [16].

3.3.2 Amplification System

The output pulses of the Ti:sapphire are expanded from 90 fs to 250 picoseconds, a factor of 2500 by adding positive chirp with a folded system that acts like a telescope between a pair of gratings [24], [25], [26], [27]. Four times a second one of the pulses is picked off by a Pockels cell and polarizer combination and injected into the LiSAF amplifier. This pulse is regeneratively amplified [28] by being allowed to bounce around in the cavity for 250 ns or approximately 25 round trips while the gain of the xenon

pumped LiSAF amplifier is at its maximum. A pulse train of amplified pulses that are separated by the cavity round trip time of about 10 ns exits the cavity. Then another Pockels cell picks off the pulse immediately after the peak of the pulse train. This 250 picosecond pulse of a couple of millijoules of energy is then recompressed to its original pulse width by using a parallel grating pair which can exactly correct for all orders of chirp added by the complementary expansion grating. The parallel grating pair is thoroughly described in Chapter 4.

REFERENCES FOR CHAPTER 3

[1] E. Hecht, Optics, Addison Wesley, Reading, 1989. pp. 250-254

[2] R. W. Boyd Nonlinear Optics, Academic Press Inc., San Diego, 1992. pp. 275-276

[3] A. E. Siegman, Lasers, University Science Books, Mill Valley, 1986. pp. 380-385

[4] Z. Bor, "Distortion of femtosecond laser pulses in lenses and lens systems," *Journ. of Modern Opt.* **35**, 1907-1918 (1988).

[5] M. Kempe, U. Stamm, B. Wilhelmi, and W. Rudolph, "Spatial and temporal transformation of femtosecond laser pulses by lenses and lens systems," *Journ. of Opt. Soc. Am. B* **9**, 1158-1161 (1992).

[6] M. Kempe, and W. Rudolph, "Impact of chromatic and spherical aberration on the focusing of ultrashort light pulses by lenses," *Opt. Lett.* **18**, 137-139 (1993).

[7] M. Kempe, and W. Rudolph, "Analysis of confocal microscopy under ultrashort light-pulse illumination," *Journ. of Opt. Soc. A* **10**, 240-245 (1993).

[8] Z. Bor, "Distortion of femtosecond laser pulses in lenses," *Opt. Lett.* **14**, 119-121 (1989).

[9] M. T. Asaki, C-P Huang, D Garvey, J Zhou, H. C. Kapteyn, and M. M. Murnane, "Generation of 11-fs pulses from a self mode-locked Ti:sapphire laser," *Opt. Lett.* **18**, 977-979 (1993).

[10] A Stingl, C Spielmann, F. Krausz, and R. Szipocs, "Generation of 11-fs pulses from a Ti:sapphire laser without the use of prisms," *Opt. Lett.* **19,** 204-206 (1994).

[11] F. Krausz, M. E. Fermann, T. Brabec, P. F. Curley, M. Hofer, M. H. Ober, C. Spielmann, E. Wintner, and A. J. Schmidt, "Femtosecond Solid-State Lasers," *IEEE J. Quantum Electron.* **QE-28**, 2097 (1992).

[12] Laser Ionics, Table of specifications (given with Argon ion laser Model 1400-12A) Laser Ionics, Orlando (1993).

[13] J. T. Verdeyen, Laser Electronics, Prentice-Hall, Englewood Cliffs, 1981. pp. 276-277

[14] J. Hecht, "Ion lasers deliver power at visible and UV wavelengths," *Laser Focus World* **28**(12), 97-105 (Dec. 1992).

[15] H. W. Kogelnik, E. P. Ippen, A. Dienes, and C. V. Shank, "Astigmatically compensated dye lasers," *IEEE J. of Quantum Electron.* **QE-8**, 373-379 (1972).

[16] J. Hecht, "Tunability makes vibronic lasers versitile tools," *Laser Focus World* **28**(10), 93-103 (Oct. 1992).

[17] J. T. Verdeyen, Laser Electronics, Prentice-Hall, Englewood Cliffs, 1981. pp. 222-230

[18] A. Yariv, Optical Electronics, 3rd ed. Holt Rinehart and Winston, Orlando, 1985. pp. 164-168

[19] A. E. Siegman, Lasers, University Science Books, Mill Valley, 1986. pp. 1041-1059

[20] T. Brabec, Ch. Spielmann, P. F. Curley, and F. Krausz, "Kerr lens mode locking," *Opt. Lett.* **17**, 1292-1294 (1992).

[21] F. Krausz, M. E. Fermann, T. Brabec, P. Curley, M. Hofer, M. H. Ober, C. Spielmann, E. Winter, and A. J. Schmidt, "Femtosecond Solid State Lasers," *IEEE Journal of Quant. Electron.* **QE 28**, 2097-2122 (1992).

[22] J. Hecht, "Tunability makes vibronic lasers versitile tools," *Laser Focus World* **28**, 93-103 (Oct. 1992).

[23] M. D. Perry, S. A. Payne, T. Ditmire, R. Beach, G. J. Quarles, W. Ignatuk, R. Olsen, and J. Weston, "Better materials trigger Cr:LiSAF laser development," *Laser Focus World* **29**, 85-92 (September 1993).

[24] P. Maine, D. Strickland, P. Bado, M. Pessot, and G. Mourou, "Generation of Ultrahigh Peak Power Pulses by Chirped Pulse Amplification," *IEEE Journal of Quant. Electron.* **QE 24**, 398-403 (1988).

[25] P. Maine, D. Strickland, M. Pessot, J. Squier, P. Bado, and G. Mourou, "Chirped Pulse Amplification: Present and Future," in Springer Series in Chemical Physics, Vol. 48: Ultrafast Phenamena VI (T. Yajima, K. Yoshhihara, C. B. Harris, and S. Shoinoya ed.), pp. 2-6. Springer-Verlag, Berlin Heidelberg, 1988.

[26] O. E. Martinez, "3000 Times Grating Compressor with Positive Group Velocity Dispersion: Application to Fiber Compensation in 1.3-1.6 μm Region," *IEEE Journal of Quant. Electron.* **QE-23**, 59-64 (1987).

[27] M. Pessot, P. Maine, and G. Mourou, "1000 Times Expansion/Compression of Optical Pulses for Chirped Pulse Amplification," *Opt. Comm.* **62**, 419-421 (1987).

[28] P. Beaud, E. Miesak, Y-F. Chen, B. H. T. Chai, and M. C. Richardson, "110 fs Fourier-transform limited Gaussian pulses from a Cr:LiSAF regenerative amplifier," *Opt. Comm.* **95**, 46-50 (1993).

CHAPTER 4

METHODS OF PULSE COMPRESSION

Pulse compression techniques are of prime importance in the area of nonlinear optics, because many of the characteristics of interest are irradiance dependent. Therefore, by compressing a pulse down to its transform limit, it is possible to obtain the maximum irradiance possible for that pulse with a given amount of energy. Pulse compression can be used to compensate for chirp caused by the Group Velocity Dispersion (GVD) and Self-Phase Modulation (SPM) that are inherent in most optical materials, as well as to recompress pulses that were intentionally expanded for the purpose of Chirped Pulse Amplification (CPA). Whereas, pulse expansion can be achieved by either material dispersion, SPM or frequency dependent geometrical path differences, both the grating and the prism methods compress positively chirped pulses by using frequency dependent geometrical path differences which cause a delay in time between the different wavelength components of the pulses.

4.1 Prism Method

Four prisms or more commonly a pair of prisms and a mirror can be used to alter the GVD of a pulse. As was described in Chapter 3, most materials exhibit a normal or positive dispersion. Therefore, one compensates by adding negative dispersion to the pulse. However, few materials exhibit a negative or anomalous dispersion in the regions of interest. Therefore, one must take advantage of the fact that an angular dispersion causes a negative dispersion to be added to the pulse. So, we have an added positive

group-velocity dispersion from the prism material, and a negative contribution from the frequency dependent geometrical path difference.

The set up usually consists of two prisms with suitable material dispersion cut so that the Brewster's angle is equal to the minimum deviation angle at the center frequency of the laser. The exit face of the second prism is parallel to the exit face of the first prism, and the exit face of the second prism is parallel to the entrance face of the first prism. So that if the two prisms were next to each other you would have a rhomboid, where the entire set up can be seen in **Figure** (4.1). The plane MM′ is perpendicular to the pulse's path between prisms I and II, and this plane of symmetry is where the mirror should be placed if two, instead of four prisms are used. Additionally, the wavelengths are laterally displaced at this point, hence a slit or an aperture can be used to control the lasing

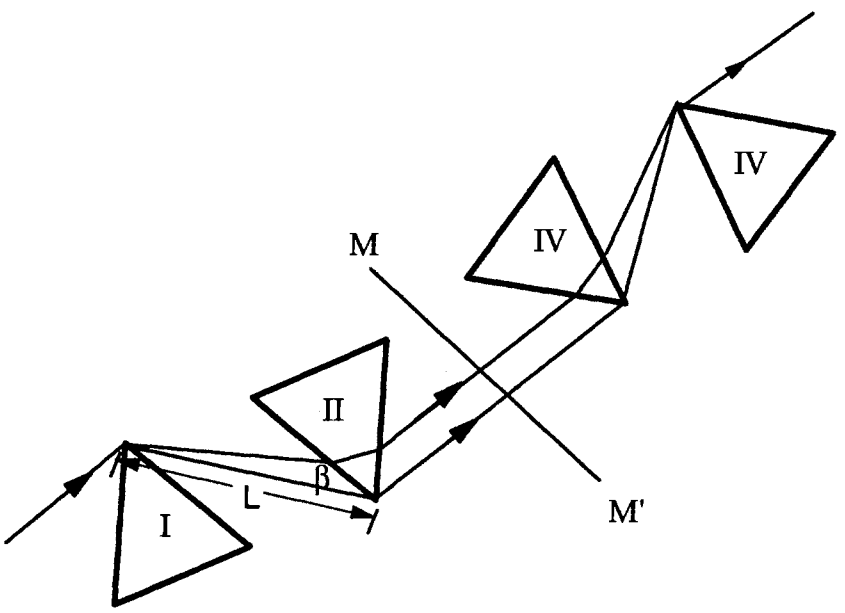

Figure 4.1 Four prism sequence for pulse compression.

frequency and/or help stabilize the modelocking of the laser at a given frequency. Ideally, by the time that the light reaches the last prism, the dispersion compensation will be complete and the different wavelength components will be temporally coincident.

The amount of dispersion compensation that is obtained is determined by first calculating the dispersion constant

$$D = -L^{-1}\frac{dT}{d\lambda} = \left(\frac{\lambda}{cL}\right)\frac{d^2P}{d\lambda^2}, \qquad (4.1)$$

where L is the physical length of the light path, P is the optical path length, λ is the wavelength in air, and T is the time for the light to traverse L. Now if we let the ray that passes through the second prism closest to its apex be the reference ray, then the path difference between the reference ray and any other ray after passing through the entire four prism set up in terms of the separation between the prisms L is given by

$$P = 2\,L\cos\beta. \qquad (4.2)$$

Hence,

$$dP/d\beta = -2\,L\sin\beta, \qquad (4.3)$$

and

$$d^2P/d\beta^2 = -2\,L\cos\beta, \qquad (4.4)$$

where β is a function of the ray's wavelength or actually the difference between its wavelength and that of the reference ray. Therefore, β primarily depends upon the bandwidth of the laser, although the shape of the incident beam may have an effect. After employing the chain rule it can be shown that

$$\frac{d^2P}{d\lambda^2} = \left[\frac{d^2n}{d\lambda^2}\frac{d\beta}{dn} + \left(\frac{dn}{d\lambda}\right)^2\frac{d^2\beta}{dn^2}\right]\frac{dP}{d\beta} + \left(\frac{dn}{d\lambda}\right)^2\left(\frac{d\beta}{dn}\right)^2\frac{d^2P}{d\beta^2}. \qquad (4.5)$$

When evaluating these derivatives it is assumed that the angle of incidence at prism I, ϕ_1 is fixed, and the angle that the transmitted beam makes with respect to the prisms normal

ϕ_2 is allowed to vary. If the respective interior angles are ϕ_1' and ϕ_2' and α is the prism's apex angle, then we can use Snell's law and the relation $\alpha = \phi_1' + \phi_2'$ to obtain

$$d\phi_2/dn = (\cos\phi_2)^{-1}\left[\sin(\phi_2') + \cos(\phi_2')\tan(\phi_1')\right] \tag{4.6}$$

and

$$\frac{d^2\phi_2}{dn^2} = \tan\phi_2\left(\frac{d\phi_2}{dn}\right)^2 - \frac{\tan^2\phi_1'}{n}\left(\frac{d\phi_2}{dn}\right). \tag{4.7}$$

Since the prisms are used at both the minimum deviation and Brewster's angle of incidence, $\phi_1' = \phi_2'$ and $\tan\phi_2 = n$. Therefore, $d\beta/dn = -(d\phi_2/dn)$ and $d^2\beta/dn^2 = -(d^2\phi_2/dn^2)$ so that

$$d\beta/dn = -2 \tag{4.8}$$

and

$$d^2\beta/dn^2 = -4 + 2/n^3. \tag{4.9}$$

Therefore, by inserting equations (4.2), (4.3), (4.8) and (4.9) into equation (4.5) one can obtain

$$\frac{d^2P}{d^2\lambda} = 4L\left\{\left[\frac{d^2n}{d\lambda^2} + \left(2n - n^{-3}\right)\left(\frac{dn}{d\lambda}\right)^2\right]\sin\beta - 2\left(\frac{dn}{d\lambda}\right)^2\cos\beta\right\}. \tag{4.10}$$

The third derivative of the optical path length with respect to wavelength is needed, when calculating the cubic phase, and the complex expression can be well approximated for typical materials by

$$\frac{d^3P}{d\lambda^3} \cong 4L\left(\frac{d^3n}{d\lambda^3}\sin\beta - 6\frac{dn}{d\lambda}\frac{d^2n}{d\lambda^2}\cos\beta\right). \tag{4.11}$$

In general, β is of the order of the angular deviation of the ray bundle, which is usually small enough so that $\sin\beta << \cos\beta$. Hence, L $\sin\beta$ is about twice the beams spot size, and $\cos\beta$ is approximately unity. Therefore, the second term adds a negative GVD that is proportional to the distance between the prisms and their dispersion, whereas the first

term does not depend upon the separation between the prisms. Rather, it depends upon the material dispersion and GVD of the prisms, as well as the beams angular deviation. Consequently, a sufficiently large distance between the prisms can compensate for the positive GVD caused by the material of the prisms and generate the negative GVD that is needed in most pulse compression applications [1], [2], [3].

4.2 Grating Theory and Example

One general manner in which to describe the GVD or change in group delay with respect to frequency is by looking at the phase of the pulse. For instance, the Fourier transform of a pulse with the following electric field

$$E(z,t) = E_o(z,t)\exp\{i[\omega t - kz + \phi(z,\omega)]\} \tag{4.12}$$

can be written as

$$E(z,\omega) = A(z,\omega)\exp[i\phi(z,\omega)] \tag{4.13}$$

where $A(z,\omega)$ and $\phi(z,\omega)$ are the amplitude and phase respectively. If we assume that their is minimal attenuation, then after the chirped pulse passes through a grating or prism compression system the pulses' Fourier transform will be

$$E(z,\omega) = A(z,\omega)\exp\{i[\phi(z,\omega) + \phi_c(z,\omega)]\}. \tag{4.14}$$

Where, $\phi_c(z,\omega)$ is the phase induced by the compression system, and both of the phase terms can be expanded in a Taylor series about the central frequency ω_o as

$$\phi(\omega) = \phi(\omega_o) + \left(\frac{d\phi}{d\omega}\right)_{\omega_o}(\omega-\omega_o) + \frac{1}{2}\left(\frac{d^2\phi}{d\omega^2}\right)_{\omega_o}(\omega-\omega_o)^2 \tag{4.15}$$

$$+\frac{1}{6}\left(\frac{d^3\phi}{d\omega^3}\right)_{\omega_o}(\omega-\omega_o)^3 + \quad \ldots\ldots \quad \frac{1}{n!}\left(\frac{d^n\phi}{d\omega^n}\right)_{\omega_o}(\omega-\omega_o)^n.$$

Here the first four terms are the constant phase factor, the group delay time, the quadratic phase term and the cubic phase term respectively, and we are only concerned in correcting for the quadratic and the cubic phase terms. This is done by generating a negative term with the compression system for every positive term that the chirped pulse possesses, and vise versa. At best, any given pulse can only be compressed back down to its transform limit as shown in **Table** (4.1).

Gratings have a relatively high efficiency and a broad tunability, and nonlinear behavior only occurs when compression ratios are high or when dealing with femtosecond pulses. The properties of gratings can be described with respect to the phase, where it has been shown that

$$\phi(\omega) = \omega\frac{P(\omega)}{c} + R(\omega), \qquad (4.16)$$

where the $P(\omega)$ is the optical path length and $R(\omega)$ is a complex geometrical function specific to the grating [4]. Now, the group delay time is

$$\tau(\omega) = \frac{d\phi}{d\omega} = \frac{P(\omega)}{c} + \frac{\omega}{c}\frac{dP(\omega)}{d\omega} + \frac{dR(\omega)}{d\omega}, \qquad (4.17)$$

so that

$$\tau(\omega) = \frac{P(\omega)}{c}. \qquad (4.18)$$

Hence, the group delay time, as well as the phase of the pulse is determined by the optical path length for that frequency [5], [6].

As described in Chapter 3, when we were performing the Ultrafast Supercontinuum Laser Source (USLS) characterization experiments, we were implementing a system that took advantage of CPA. The Ti:sapphire pulse of about 90 femtoseconds was expanded to about 250 picoseconds using an arrangement with a telescope between a grating pair, and then it was amplified in a LiSAF regenerative amplifier. Since, this pulse expander is

identically matched to the grating pair pulse compressor [2], [7], [8], [9] it was obvious that the grating pair would be the optimal compression scheme. In those experiments our goal was simply to find out the correct grating spacing and compress the pulse. Instead of employing the phase delay method [4], [10] to calculate the correct distance between the gratings, we used a path delay method as discussed by Broson [11], [12]. Although, both methods are correct and equivalent, the latter method is simpler to visualize.

In the path delay method, one simply cancels the linear chirp in the 250 picosecond pulse by delaying the longer wavelengths at the beginning of the pulse by 250 picoseconds with respect to the shorter wavelengths at the end of the pulse. In our case the redder wavelengths that lead the pulse must be delayed by 250 picoseconds so that they are placed on top of the shorter wavelengths temporally. However, at best the pulse width can only be compressed down to the Full Width at Half Maximum (FWHM) as expressed by the uncertainty relation for a transform limited pulse. These are tabulated in **Table** (4.1). Here, Δt and $\Delta\tau$ are the FWHM of I(t) and $G_2(\tau)$, and $\Delta\nu$ is the FWHM of the frequency spectrum.

Table 4.1 Transform Limited Pulse width Relations for Different Pulse shapes [13].

Pulse Shape	I(t)	$\Delta\tau/\Delta\nu$	$\Delta\nu\Delta t$
Square	$1(0\le t\le\Delta t)$	1	0.886
Gaussian	$\exp\{\frac{-(4\ln 2)t^2}{\Delta t^2}\}$	1.414	0.441
$Sech^2$	$\mathrm{sech}^2\{\frac{1.76t}{\Delta t}\}$	1.55	0.315
Exponential	$\exp\{\frac{-(\ln 2)t}{\Delta t}\}$	2	0.11

We can see in **Figure** (4.2) that the optical path length for any pulse passing though compression gratings is composed of two parts, $P_1(\omega)$ and $P_2(\omega)$, such that

$$P(\omega) = P_1(\omega)+P_2(\omega). \qquad (4.19)$$

Where

$$P_1(\omega) = d \sec\theta_r \qquad (4.20)$$

and

$$P_2(\omega) = d \cos(\theta_r-\theta_i)\sec\theta_r, \qquad (4.21)$$

so that the total optical path length is

$$P(\omega) = d [\cos(\theta_r-\theta_i)+1]\sec\theta_r, \qquad (4.22)$$

with d being the perpendicular grating separation and θ_i and θ_r being the incident and reflected angles respectively.

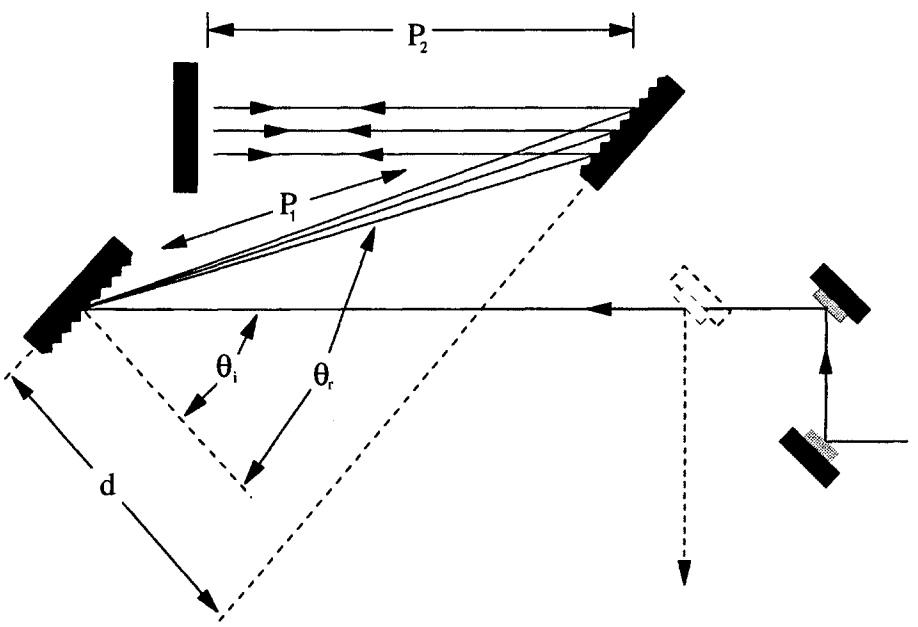

Figure 4.2 Doubled grating pair pulse compression system.

Now, like the phase $\phi(\omega)$, the optical path length $P(\omega)$ can be expanded in a Taylor's series about ω_o. So that

$$P(\omega) = d\left[p(\omega) + (\omega - \omega_o)p'(\omega_o) + \frac{1}{2}(\omega_o - \omega)^2 p''(\omega_o) + \cdots \right. \qquad (4.23)$$

$$\left. \cdots + \frac{1}{n!}(\omega_o - \omega)^n p^{(n)}(\omega_o) \right]$$

where ω_o is the central frequency of the laser, ω is the frequency of the individual wave component, and $p^{(n)}(\omega_o)$ are the path length coefficients.

Several of the articles [4], [10] have errors in their derivation of the correct grating spacing, which we confirmed by comparing our solution to that of other articles [11]. The correct derivation is shown starting with the following form of the grating equation

$$\sin\theta_r + \sin\theta_i = \frac{m\lambda}{\Lambda} = \frac{2m\pi c}{\omega\Lambda}, \qquad (4.24)$$

where θ_i and θ_r are the angles of incidence and refraction of the pulse with respect to the gratings normal, Λ is the grating spacing and m is the refractive order which in our case is 1.

$$\theta_r = \sin^{-1}\left(\frac{2\pi c}{\omega\Lambda} - \sin\theta_i\right) \qquad (4.25)$$

$$\frac{\partial}{\partial x}\sin^{-1} u = \frac{1}{\sqrt{1-u^2}}\frac{\partial u}{\partial x} \qquad (4.26)$$

One can obtain expressions for the path length coefficients by taking the first and second derivatives of $P(\omega)$ to get,

$$p(\omega) = \frac{1}{d}\left[\frac{\partial}{\partial\omega}P(\omega)\right] = \frac{\partial}{\partial\omega}\frac{[\cos(\theta_r(\omega) - \theta_i) + 1]}{\cos\theta_r(\omega)}. \qquad (4.27)$$

Note, that although θ_r has an ω dependence as shown in Equations (4.25), it will not be explicitly stated from here on out. Therefore, $p(\omega)$ can be written as

$$p(\omega) = \frac{\partial}{\partial\omega}\frac{[\cos(\theta_r - \theta_i) + 1]}{\cos\theta_r} \tag{4.28}$$

$$= \frac{\{-\cos\theta_r \sin(\theta_r - \theta_i) + [\cos(\theta_r - \theta_i) + 1]\sin\theta_r\}}{\cos^3\theta_r(\omega)}\left(\frac{-2\pi c}{\omega^2\Lambda}\right) \tag{4.29}$$

$$= \frac{-2\pi c}{\omega^2\Lambda\cos^2\theta_r}\{\cos\theta_r\cos\theta_i\sin\theta_r + \cos^2\theta_r\sin\theta_i - \cos\theta_r\sin\theta_r\cos\theta_i + \sin^2\theta_r\sin\theta_i + \sin\theta_r\} \tag{4.30}$$

$$= \frac{-2\pi c}{\omega^2\Lambda}\frac{(\sin\theta_r - \sin\theta_i)}{\cos^3\theta_r} \tag{4.31}$$

$$= \frac{-4\pi^2c^2}{\omega^3\Lambda^2}\frac{1}{\cos^3\theta r} \tag{4.32}$$

$$= \frac{-4\pi^2c^2}{\omega^3\Lambda^2}\left[1 - \left(\frac{2\pi c}{\omega\Lambda} - \sin^2\theta_i\right)\right]^{-\frac{3}{2}} \tag{4.33}$$

Now, by differentiating equation (4.32) with respect to ω once again, $p''(\omega)$ can be found.

$$p''(\omega) = \frac{1}{d}\left[\frac{d^2}{d\omega^2}P(\omega)\right] = \frac{\partial}{\partial\omega}p'(\omega) = \frac{\partial}{\partial\omega}\left[\frac{-4\pi^2c^2}{\omega^3\Lambda^2}\frac{1}{\cos^3\theta_r}\right] \tag{4.34}$$

$$= \frac{-4\pi c^2}{\omega^3 \Lambda^2}\left[\frac{-\frac{3}{\omega^4}\cos^3\theta_r - \frac{1}{\omega^3}3\cos^2\theta_r(-\sin\theta_r)\cos^{-1}\theta_r\left(\frac{-2\pi c}{\omega^2\Lambda}\right)}{\cos^6\theta_r}\right] \tag{4.35}$$

$$= \frac{12\pi^2 c^2}{\Lambda^2\,\omega^4\cos^5\theta_r}\left[\cos^2\theta_r + \sin\theta_r\left(\frac{2\pi c}{\omega\Lambda}\right)\right] \tag{4.36}$$

$$= \frac{12\pi^2 c^2}{\Lambda^2\,\omega^4}\frac{\left[\cos^2\theta_r + \sin\theta_r(\sin\theta_r + \sin\theta_i)\right]}{\cos^5\theta_r} \tag{4.37}$$

$$= \frac{12\pi^2 c^2}{\Lambda^2\,\omega^4}\left[\frac{1+\sin\theta_r\sin\theta_i}{\cos^5\theta_r}\right] \tag{4.38}$$

$$p''(\omega) = \frac{12\pi^2 c^2}{\Lambda^2\,\omega^4}\frac{\left[1+\sin\theta_i\left(\frac{2\pi c}{\omega\Lambda} - \sin\theta_i\right)\right]}{\left[1-\left(\frac{2\pi c}{\omega\Lambda} - \sin\theta_i\right)^2\right]^{\frac{5}{2}}} \tag{4.39}$$

If we have linearly a chirped pulse such that

$$\omega(t) = \omega_o + \frac{\Delta\omega}{\Delta t_c}, \tag{4.40}$$

where $\Delta\omega$ is the bandwidth of the chirped pulse, and Δt_c is its duration and ω_o is its central frequency, then maximum compression of the pulse occurs when the linear chirp of the compressor delay cancels the pulses linear chirp. This occurs when

$$\frac{d}{c}p'(\omega_o) + \frac{\Delta t_c}{\Delta\omega} = 0, \tag{4.41}$$

where the minimum pulse length is determined by the transform limit as is shown in **Table** (4.1). However, in many cases the magnitude of the quadratic chirp is large

enough to restrict ones ability to achieve a bandwidth limited pulse, hence in the limit where the pulse is much longer than the transform limit

$$\Delta t_{min} = \frac{d}{c} p''(\omega_o)\left(\frac{\Delta\omega}{2}\right)^2. \qquad (4.42)$$

By inserting equation (4.41) into (4.42), we can determine that

$$\Delta t_{min} = \tfrac{1}{4}(\Delta t_c)(\Delta\omega)\left|\frac{p''(\omega_o)}{p'(\omega_o)}\right|. \qquad (4.43)$$

The minimum pulse width is only obtained when transform limited pulse length $\Delta\tau_{limit}$ is much less than that in equations (4.7) and (4.8). Hence, for a $sech^2$ pulse

$$\frac{\Delta t_{min}}{\Delta t_{limit}} = a = \tfrac{\pi}{2}\frac{(\Delta t_c)(\Delta\omega)^2}{.315}\left|\frac{p''}{p'}\right| << 1 \qquad (4.44)$$

must be true for the output pulses from a grating pulse compressor to give truly transform limited pulses. It should be noted however, that the above equation assumes that all of the quadratic path (cubic phase) difference created by the grating pairs contributes to the chirp of the pulse. In our experiment, most of the chirp is intentionally created by our matched expansion system, therefore we will have corrected for all but the quadratic chirp generated by the optical materials in the system [14], [15].

We compressed the 850 nm 250 ps amplified pulse back down to its original bandwidth limited 90 fs with two 1800 line per mm holographic gratings in the configuration shown in Figure (4.2). The gratings were gold plated for high reflectivity and high damage threshold around 850 nm, although in most high power systems the beam must be expanded so as not to damage the gratings. In fact, the maximum irradiance achievable by systems that employ CPA is usually the damage threshold of the gratings, however our output powers were well below this irradiance. The gratings were designed for maximum efficiency with an incident angle of 41.6 degrees, hence θ_i and θ_r

where 41.8 and -60 degrees respectively. For a 90 fs linearly chirped pulse at 850 nm, $\Delta\nu$ and $\Delta\lambda$ equal 3.5×10^{12} Hz and 8.43 nm respectively. We knew that the amplifier may have lengthened the pulse further than 250 ps, and added nonlinearities, so that the chirp may not be linear anymore. Yet, we used equation (4.6) and determined the correct grating separation assuming that there was no higher order chirp. We determined that the perpendicular grating separation d should be 20.1926 cm, and the more easily measured straight line separation between the center of the gratings, P_1 or d $\sec\theta_r$, should be about 40.385 cm when the system is operated in a double pass manner as shown in **Figure** (4.2). By using the above distances as a starting point, we determined experimentally that the straight line separation P_1, that minimized the pulse width was about 40 cm. Hence, the linear approximation worked well for helping us determine the correct grating separation. The minimum pulse width that we were able to obtain was around 113 fs, where the measurement procedure will be thoroughly discussed in Chapter 5. It is obvious that we were able to compress the pulse to near its transform limit. We may have been incapable of achieving the original pulse length for a variety of reasons, including the presence of higher order dispersion added by the optical system, inaccuracy in our measurement procedure, beam walk off errors caused by the finite beam size [16] and/or the incident pulse was never as short as we believed.

4.3 Comparison

Both the prism and the grating methods of pulse compression work effectively, however each has its own advantages and disadvantages. The prism method is the main choice for intracavity compensation [17], [18] although cavity mirrors also have been used [19], [20]. The prism method is also used to fine tune the dispersion compensation outside of cavities, especially in the case where gratings are unable to correct for the

cubic chirp caused by material dispersion. Still, the grating method is the workhorse for extracavity GVD compensation, especially when compressing very high power pulses that were stretched using the complementary anti-parallel grating pair [7] - [9] so as to perform Chirped Pulse Amplification (CPA). **Table** (4.2) shows the second and third derivatives of the phase with respect to frequency for a double prism pair, a double grating pair, and material.

Table 4.2 Second and third derivatives of phase with respect to frequency for a double prism pair, a double grating pair, and an optical material [21].

	$\frac{d^2\phi}{d\omega^2}$	$\frac{d^3\phi}{d\omega^3}$
Prism	$\frac{\lambda^3}{2\pi c^2}\frac{d^2P}{d\lambda^2}$	$\frac{-\lambda^4}{2\pi^2 c^3}\left(3\frac{d^2P}{d\lambda^2}+\lambda\frac{d^3P}{d\lambda^3}\right)$
Grating	$\frac{\lambda^3 L}{\pi c^2 \Lambda^2}\left[1-(\frac{\lambda}{\Lambda}-\sin\theta_i)^2\right]^{-\frac{3}{2}}$	$-\frac{d^2\phi_g}{d\omega^2}\frac{6\pi\lambda}{c\Lambda}(1+\sin\theta_r \sin\theta_i)\cos^{-2}\theta_r$
Material	$\frac{\lambda^3 l_m}{2\pi c^2}\frac{d^2n_m}{d\lambda^2}$	$\frac{-\lambda^4 l_m}{2\pi^2 c^3}\left(3\frac{d^2n_m}{d\lambda^2}+\lambda\frac{d^3n_m}{d\lambda^3}\right)$

One of the advantages of the grating method is that it takes only one fourth the distance to compress the same pulse as with the prism method, so that it takes up far less space. Additionally, the laser pulse is not passing through any material, therefore there is no fear of generating enormous nonlinear effects when high powers are being implemented. However, the cubic phase added by the grating system is positive, which is the same sign as that generated by material dispersion. Therefore, the grating system can be incapable of correcting for higher order phase, and the minimum pulse width can be limited by the cubic phase or quadratic chirp instead of the transform limit. Additionally, the grating system generates large losses in energy, in fact 50 percent of the energy may

not make it through the system. Due to these high loses, and inability to correct for the higher order chirp, the grating method is not at all useful inside of laser cavities, where loss is extremely important.

Although, antireflection coatings can be added to the prisms so as to reduce the losses, that is not usually necessary. This is because the prisms are usually set up at Brewster's angle, hence the Fresnel losses are for the most part eliminated. Also, the incident and transmitted beam are collinear, and the prism can correct for higher order dispersion. Hence, the prism method is ideal for intracavity compression, such as in a Ti:sapphire or dye laser cavity in an X or Z configuration. Additionally, it is easy to adjust the dispersion down to the zero value, and either positive or negative chirp can be added to a pulse accurately. Furthermore, there is no transverse displacement of the temporally dispersed beams, which can broaden ultrashort pulses. Therefore, the prism method is better than the grating method for compressing pulses down to their transform limit when the pulses were expanded due to material interactions.

Since, both the grating pair and prism pair methods of pulse compression have their own advantages, they have been combined to take advantage of them. This has been done by first sending the chirped pulse through a grating system that corrects for the quadratic phase distortion, and then the prisms which correct for the cubic phase distortion [22]. The use of both systems in sequence doubles the number of variables that can be optimized, so that it is easier to achieve transform limited pulses than with either method alone. In fact, pulses that were frequency broadened with an optical fiber were compressed down to 6 femtoseconds using a grating prism sequence [21], [23].

REFERENCES FOR CHAPTER 4

[1] J. P. Gordan, and R. L. Fork, "Optical Resonator with negative dispersion," *Opt Lett.* **9**, 153-155 (1984).

[2] O. E. Martinez, J. P. Gordon, and R. L. Fork, "Negative group-velocity dispersion using refraction," *J. Opt. Soc. Amer. A.* **1**, 1003 (1984)..

[3] R. L. Fork, O. E. Martinez, and J. P. Gordon, "Negative dispersion using pairs of prisms," *Opt. Lett.* **9**, 150 (1984)..

[4] E. B. Treacy, "Optical Puse Compression With Diffraction Gratings," *IEEE J. Quantum Electron.* **QE-5**, 454 (1969).

[5] T. Gray, "Optical Pulse Compression," *Spectra-Physics Laser Technical Bulletin*, # 11, (August 1987).

[6] I. P. Cristov, and I. V. Tomov, "Large bandwidth pulse compression with diffraction gratings," *Opt Comm.* **58**, 338 (1986).

[7] P. Maine, D. Strickland, M. Pessot, J. Squier, P. Bado, and G. Mourou, "Chirped Pulse Amplification: Present and Future," in Springer Series in Chemical Physics, Vol. 48: Ultrafast Phenamena VI (T. Yajima, K. Yoshhihara, C. B. Harris, and S. Shoinoya ed.), pp. 2-6. Springer-Verlag, Berlin Heidelberg, 1988.

[8] O. E. Martinez, "3000 Times Grating Compressor with Positive Group Velocity Dispersion: Application to Fiber Compensation in 1.3-1.6 μm Region," *IEEE Journal of Quant. Electron.* **QE-23**, 59-64 (1987).

[9] M. Stern, J. P. Heritage, and E. W. Chase, "Grating Compensation of Third-Order Fiber Dispersion," *IEEE Journal of Quant. Electron.* **QE-28**, 2742-2748 (1992).

[10] G. P. Agrawal, Nonlinear Fiber Optics, pp. 180-186, Academic Press Inc., San Diego, 1989. pp. 148-153

[11] S. D. Brorson, and H. A. Haus, "Geometrical limitations in grating pair pulse compression," *Appl. Opt.* **27**, 25 (1988).

[12] S. D. Brorson, and H. A. Haus, "Diffraction gratings and geometrical optics," *J. Opt. Soc. B* **5**, 247-248 (1988).

[13] E. P. Ippen, and C. V. Shank, in Ultrashort Light Pulses, "Picosecond Techniques and Applications", p. 88 (S. l. Shapiro, ed.) Springer-Verlag, New York, 1977.

[14] J. D. McMullen, "Analysis of compression of frequency chirped optical pulses by a strongly dispersive grating pair," *Appl. Opt.* **18**, 737-741 (1979).

[15] S. D. Brorson, and H. A. Haus, "Geometrical limitations in grating pair pulse compression," *Appl. Opt.* **27**, 25 (1988).

[16] O. E. Martinez, "Grating and prism compressors in the case of finite beam size," *J. Opt. Soc. Am. B* **3**, 929-934 (1986).

[17] B. E. Lemoff, and C. P. J. Barty, "Cubic-phase-free dispersion compensation in solid-state ultrashort-pulse lasers," *Opt. Lett.* **18**, 57-59 (1993).

[18] B. Proctor, and F. Wise, "Quartz prism sequence for reduction of cubic phase in a mode-locked Ti:Al_2O_3 laser, *Opt. Lett.* **17**, 1295-1297 (1992).

[19] S. De Silvestri, P Laporta, and O Svelto, "The Role of Cavity Dispersion in CW modelocked Lasers," *IEEE Journal of Quant. Electron.* **QE-20**, 533-539 (1984).

[20] A. Stingl, C. Spielmann, and F. Krausz, "Generation of 11-fs pulses from a Ti:sapphire laser without the use of prisms," *Opt. Lett.* **19**, 204-206 (1994).

[21] R. L. Fork, C. H. Brito Cruz, P. C. Becker, and C. V. Shank, "Compression of optical pulses to six femtoseconds by using phase compensation," *Opt Lett.* **12**, 483-485 (1987).

[22] R. Dorsinville, P. P. Ho. J. T. Manassah, and R. R. Alfano, "Applications of Supercontinuum Present and Future," in The Supercontinuum Laser Source, (R. R. Alfano ed.) Springer-Verlag, New York, 1989. pp. 438-439

[23] A. S. L. Gomes, and A. S. Gouveia-Neto, and J. R. Taylor, "Optical fibre-grating pulse compressors," *Opt. and Quant. Electron.* **20**, 95-112 (1988).

CHAPTER 5

PULSE MEASUREMENT TECHNIQUES

When working with lasers in the area of nonlinear optics it is very important to be able to characterize your pulse. This is because most of the nonlinear properties are either fluence(J/cm^2) or irradiance dependent(W/cm^2). Therefore, it is important to know the total energy, spatial shape and the temporal shape of the pulse. The advent of ultrashort pulses in recent years has made measuring the temporal shape or pulse width increasingly difficult, unless all optical techniques are implemented. However, the traditional electronic techniques of implementing CCD arrays and power meters or energy detectors can still be effective at measuring the total energy and spatial profile of these ultrashort pulsed beams. For instance, a calibrated energy detector can be used to measure the energy of low repetition rate lasers. Additionally, a calibrated power meter can be used to measure the average power of a cw modelocked laser or of a high repetition laser, and if knowledge of the repetition rate is known the energy per pulse can be determined. Similarly, CCD arrays or pinhole scans with a detector can be used to measure the spatial profile of most laser beams. However, the traditional photodiode and oscilloscope combination is no longer sufficient to measure the temporal characteristics of the shortest laser pulses.

The processes that we are interested in are predominately irradiance dependent, therefore, the exact pulse width is extremely important. Hence, this chapter will deal only with pulse width measurement techniques. Furthermore, it will focus on autocorrelation techniques that use nonlinear processes to measure the pulse width of a laser.

Additionally, some attention will be paid to the shape of autocorrelation functions for different pulse shapes. Not only is knowledge of a laser's pulse width important, but some of the material measurement techniques that we used are really variations of an autocorrelation pulse width measurement technique. Therefore, the mathematics and calculations presented here will help in the theory of our material characterization techniques, and assist in the analysis of experimental results.

5-1 Methods of Pulse Width Measurement

The combination of a detector and an oscilloscope is the easiest way to measure the pulse width of a laser pulse, however this method is unable to accurately measure ultrashort pulses. In fact, only all optical techniques can measure pulse widths in the sub picosecond regime, because we are limited to the rise time of the photodiodes and the oscilloscope. In addition to discussing some important all optical measurement techniques the limitations of the photodiode oscilloscope method will be mentioned. However, second harmonic measurement techniques, and their autocorrelation functions will not be discussed at this time. Rather, an entire section will be devoted to each, because of their importance in our material characterization and pulse width measurements.

5.1.1 Photodiode-Oscilloscope

Using a simple photodiode connected to an oscilloscope is the simplest manner in which to measure the temporal profile of a pulse of light. The total rise time of the pulse as viewed on the oscilloscope is

$$t_{system} = \sqrt{t_{scope}^2 + t_{detector}^2} \qquad (5.1)$$

so that

$$t_{pulse} = \sqrt{t_{trace}^2 - t_{system}^2}. \qquad (5.2)$$

Oscilloscopes with a bandwidth of 5 GHz have a rise time of around 70 picoseconds, and the fastest photodiodes have rise times typically around 25 picoseconds, but these cost several thousand dollars. Similarly, there are superconducting oscilloscopes that can go down to several picoseconds, as well as faster photodiodes that are made with Gallium Arsenide as an active element, but their prices are extremely high and femtosecond pulses still cannot be measured. However, if there are many repetitive pulses as in the case of a cw mode locked laser, then real time measurement is not needed and sampling techniques can be used. Since, a typical sampling head may have a rise time of only about 30 picoseconds, the photodiodes act primarily as the limiting factor. However, this is still only sufficient to obtain information about the stability of the system. Therefore, the shortest pulses that we can hope to realistically measure by standard electronic techniques are around 30 picosecond [1].

5.1.2 Single Shot measurement by the Optical Kerr Effect

The optical Kerr shutter provides a convenient way to measure the dynamics of molecular orientation in liquids and electronic state distortions in glasses or other media. However, the optical Kerr shutter is mentioned here, because it can be used as a method to measure the chirp of a white light continuum. Additionally, the optical Kerr shutter can be used as a single shot pulse width measurement technique for femtosecond pulses.

The optical Kerr shutter takes advantage of the optical Kerr effect, where an intense ultrashort pump pulse induces a transient birefringence in a Kerr medium. This induced birefringence can cause the polarization of a probe beam to be altered. The experimental set up consists of the probe beam passing through a Kerr medium that is placed between a polarizer and an analyzer, while the pump beam passes through the same part of the Kerr

medium at a slight angle with a polarization of about 45 degrees with respect to the probe beam. When the pump and probe beam are coincident upon the Kerr medium, the probe beam will see a different refractive index for the polarization components parallel and perpendicular to the probe beam. This pump induced birefringence causes the coincident part of the probe beam to alter its polarization, so that it can partially pass through the analyzer.

The time evolution of the Kerr shutter transmission is then directly proportional to the index of refraction variation squared and the relaxation time of the material. When the relaxation time is large compared to the excitation duration, the probe pulse transmission is primarily dependent on the dynamics of the optical Kerr effect in the medium. Whereas, the shutter transmission is proportional to the intensity of the pump pulse squared for an "instantaneous" Kerr medium. Therefore, for single shot pulse width measurements or when characterizing a continuum it is desirable to use a Kerr medium with an instantaneous effect such as thorium doped glass.

If a continuum is used as the probe pulse, then its chirp can be determined. This is done by varying the path delay between the pump and the probe , while looking at the spectrum of the transmitted part of the probe with a spectrometer. The chirp is obtained by plotting the maximum wavelength transmitted versus the time or path delay. The basic set-up for this procedure can be seen in **Figure** (5.1).

Now, using the same set up and the information pertaining to the continuum's chirp, one can determine the pulse width of the pump beam in one shot. This is done by passing the pump beam through a portion of the continuum that is linearly chirped, and then recording the wavelengths transmitted through the Kerr medium with a spectrometer. The pulse's temporal shape can then be mapped using knowledge of the relative intensity for each frequency of the continuum, along with the plot of the continuum's chirp that

was obtained above. This pulse width measurement technique allows the measurement of asymmetrical pulses, whereas traditional second order autocorrelation techniques do not detect asymmetries [2], [3], [4].

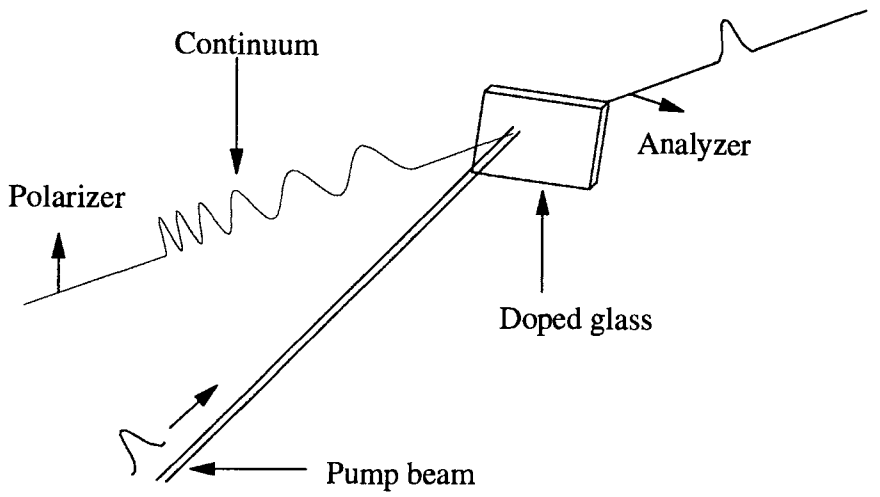

Figure 5.1 Possible set-up for mapping the chirp of an USLS or single shot pulse width measurement.

5.1.3 Two-Photon Fluorescence (TPF) Measurements

The two-photon fluorescence measurement(TPF) method consists of splitting a short high intensity pulse into two identical replicas. The two beams then travel in opposite directions into a fluorescent dye cell so that the path length traveled is the same. The dye is chosen so that it can be excited to fluoresce by the light of the laser only by two photon absorption. The fluorescence intensity from the dye cell is then photographed as seen in **Figure** (5.2). The intensity of the fluorescence is related to the pulse shape by

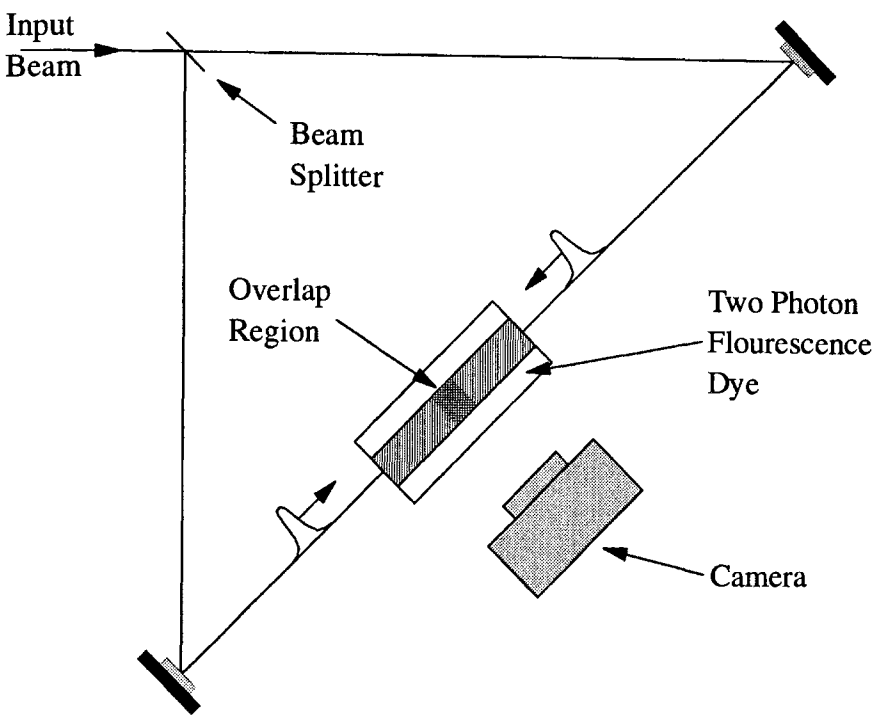

Figure 5.2 Set up for the Two Photon Fluorescence pulse width measurement technique.

$$I(\tau) = A[\int_{-\infty}^{\infty} I(t)^2\,dt + 2\int_{-\infty}^{\infty} I(t)I(t+\tau)dt], \qquad (5.3)$$

where A is a constant of proportionality and $\tau = 2Z/c$. Therefore, the intensity can be written in terms of the second order intensity autocorrelation function as

$$I(\tau) = A[G_2(0) + 2G_2(\tau)], \qquad (5.4)$$

where

$$G_2(\tau) = \int_{-\infty}^{\infty} I(t)I(t+\tau)dt \qquad (5.5)$$

and the complete autocorrelation profile is displayed simultaneously as a function of distance. The second harmonic autocorrelation methods that we used contain the same sort of pulse correlation functions as the output, therefore these correlation functions will be discussed in detail later. The main benefit of the TPF method is that it allowed the measurement of pulse width with only one pulse. Whereas, the initial second harmonic methods required the use of many pulses at different path lengths, therefore TPF methods initially superseded the second harmonic methods of pulse measurement. But, the TPF method required proper knowledge of the camera's magnification, development of film and then a microdensitometer to get the intensity profile from the film, so it took a considerable amount of time to perform. Additionally, it takes time to calibrate the system and requires the use of messy dyes. Therefore, even though it is now currently possible to use a CCD array to mimic the function of the camera, the development of simpler single shot second harmonic autocorrelation methods have replaced the TPF method. Additionally, the widespread use of cw modelocked lasers makes multiple shot second harmonic methods more attractive. Hence, the second harmonic methods dominate the field presently.

5.2 Correlation Functions

The nonlinear optical techniques that we are concerned with do not provide us with the shape of the pulse that we measure. Rather, they provide us with the autocorrelation function of the incident pulses' intensity envelope. Therefore, it is very important to consider the relationship between the pulses' shape and that of its correlation function. There are three basic and characteristic properties by which correlation functions can be categorized. A correlation has a background or is background free can be slow or fast and is either a cross-correlation or autocorrelation, where the nth order correlation is

performed in general with n different pulses. For n distinct light pulses having a real electric field given by

$$e(t) = \mathrm{Re}[E(t)], \tag{5.6}$$

where

$$E(t) = E_o(t)\exp\left\{i\left[\omega_j t + \phi_j(t)\right]\right\} \tag{5.7}$$

and $E_o(t)$ is the temporal shape of the pulse. We can write the general nth-order fast correlation function with background as

$$g_B^n(\tau_1,\tau_2,\cdots,\tau_{n-1}) = \frac{\int_{-\infty}^{\infty}\left\{e_1(t)+e_2(t+\tau_1)+\cdots+e_n(t+\tau_{n-1})\right\}^{2n}dt}{\int_{-\infty}^{\infty}\left\{e_1(t)^{2n}+e_2(t+\tau_1)^{2n}+\cdots+e_n(t+\tau_{n-1})^{2n}\right\}dt}. \tag{5.8}$$

The denominator in equation (5.8) has been chosen so that the expression is normalized to its background level $g_B^n(\infty,\infty,\cdots,\infty) = 1$, because all the cross terms disappear for $\tau_n = \infty$ in the numerator. Similarly, the general nth order background-free correlation function is

$$g_0^n(\tau_1,\tau_2,\cdots,\tau_{n-1}) = \frac{\int_{-\infty}^{\infty}\left\{e_1(t)e_2(t+\tau_1)\cdots e_n(t+\tau_{n-1})\right\}^2 dt}{\int_{-\infty}^{\infty}\left\{e_1(t)e_2(t)\cdots e_n(t)\right\}^2 dt}, \tag{5.9}$$

where the denominator has been chosen so that $g_0^n(0,0,\cdots 0) = 1$. The main difference between the background and the background-free correlation is that g_b^n remains finite for all delays, whereas g_0^n vanishes if any of the delays is much larger than the duration of any of the pulses. In general the peak to background ratio of an nth order fast correlation with background is equal to $n^{(2n-1)}$, so that for a second order autocorrelation we have an 8 to 1 peak to background ratio. A correlation is termed fast when it contains rapidly

varying phase terms $\sim\cos(\omega_j\tau_{j-1})$, which require control and measurement of the spatial variations on a scale of about 1/10 that of the shortest wavelength involved [5].

When phase matched high intensity laser pulses are incident on a second harmonic crystal, the output field is at twice the frequency of the input with a magnitude proportional to the square of the input field. Similarly, when two pulses are incident in the same polarization with a delay between them, then the output field is proportional to the square of the total input field. Hence, the current produced by the second harmonic field incident upon a detector is proportional to the integral over all time of the output field squared. This is of the same form as a fast second order autocorrelation with background, that is

$$g_2(\tau)=\frac{\int_{-\infty}^{\infty}\left\{|E(t)+E(t-\tau)|^2\right\}^2 d\tau}{\int_{-\infty}^{\infty}|E^2(t)|^2 d\tau}. \tag{5.10}$$

This is regularly referred to as interferometric autocorrelation, however if the detector is not fast enough to resolve the fringes we obtain the second order intensity autocorrelation

$$G_2^B(\tau)=1+2G_2(\tau). \tag{5.11}$$

Here $G_2(\tau)$ is the fringe averaged portion of the intensity autocorrelation, which is also equal to the background-free autocorrelation, which is

$$G_2(\tau)=\frac{\int_{-\infty}^{\infty}|E^2(t)E^2(t-\tau)|d\tau}{\int_{-\infty}^{\infty}|E^2(t)|^2 d\tau}. \tag{5.12}$$

The relationhips between these functions and the incident pulse shapes are extremely important, therefore **Table** (5.1) shows them for both Gaussian and $sech^2$ shaped pulses. Here Δt and $\Delta\tau/\Delta t$ represent the ratio between the input functions FWHM to its HW1/eM, and the FWHM of $G_2(t)$ and the FWHM of the input function respectively. The equations listed for $g_2(\tau)$ in the **Table** (5.1) are the upper and lower envelopes of the second order interferometric autocorrelation function.

Table 5.1 Diagnostic functions corresponding to various pulse shapes [6].

$I(t)$	$\exp(-t^2)$	$sech^2(t)$
Δt	1.665	1.763
$I(\omega)$	$\exp(-\omega^2)$	$sech^2(\pi\omega/2)$
$\Delta\omega$	1.665	1.122
$\Delta\omega\Delta t$	2.772	1.978
$G_2(\tau)$	$\exp(-\tau^2/2)$	$\frac{3(\tau\cosh\tau-\sinh\tau)}{\sinh^3\tau}$
$\Delta\tau$	2.355	2.720
$\Delta\tau/\Delta t$	1.414	1.543
$g_2(\tau)$	$1+3G_2(\tau)\pm 4\exp(-3\tau^2/8)$	$1+3G_2(\tau)\pm\frac{3(\sinh 2\tau-2\tau)}{\sinh^3\tau}$

Second order autocorrelation functions are always symmetric [7] irrespective of any asymmetries in the actual pulse shape, therefore higher order correlation functions must be implemented to determine I(t) uniquely. In fact only correlation functions of an odd order will ever be asymmetric. It has been shown that exact knowledge of both the second and third order correlation functions is sufficient to describe all higher orders [8], [9], [10], hence the pulse shape can be determined. However, as the order increases

$I^{(n-1)}(t)$ becomes a sharper function in time. Hence, it becomes more sensitive to pulse asymmetries. Therefore, higher order correlation functions can be used to better determine the shape of a pulse, and orders of up to five have been seen experimentally [11]. A third order correlation would require a third order process like three photon absorption or third harmonic generation, and higher processes would require higher order nonlinearities. These higher order nonlinearities may give more information than the second order autocorrelation, but they have a lower conversion efficiency and are more difficult to implement.

5.3 Second Harmonic Autocorrelation Methods

As stated above, the nonlinear interaction of two pulses with a varying delay between each other delivers us a second order autocorrelation function as they pass through a second harmonic crystal. This process is a very effective way to determine the pulse shape of an incident laser pulse. Here, we describe the autocorrelation systems that were built along with the measurements that we performed. They include the background free autocorrelation system for a picosecond Nd^{3+} doped YLF laser, an interferometric autocorrelation system for a Ti:sapphire laser, and a single shot noncollinear autocorrelator for the output of a low repetition rate Cr:LiSAF amplified Ti:sapphire laser.

5.3.1 Interferometric Autocorrelation

The purpose of implementing an interferometric autocorrelation is to obtain information about the chirp of a pulse, whereas an intensity autocorrelation can only obtain the pulse width [12]. In fact any change in shape of the pulse causes a much larger change to occur in the interferometric autocorrelation than in the fringe average

autocorrelation. As shown in **Figure** (5.3) the Gaussian and hyperbolic secant squared functions with the same Full Width at Half Maximum (FWHM) are virtually identical, however there is a noticeable difference in the theoretical shape of their second order interferometric autocorrelation envelopes as shown in **Figure** (5.4). Whereas, as is shown at the end of Chapter 6, their respective fringe averaged autocorrelations are much more similar. More, importantly, the shape of an intensity or fringe averaged autocorrelation remains the same when the incident laser pulse is chirped, whereas that of an interferometric autocorrelation is altered. An idea of how the shape of the autocorrelation changes for various amounts of chirp can be obtained by numerically integrating the equation below as given by Diels et al. [13], [14].

$$g_2(\tau) = 3/8\int \{E_o^4(t) + E_o^4(t-\tau) + 4E_o^2(t)E_o^2(t-\tau) \qquad (5.10)$$

$$+4\left[E_o^2(t) + E_o^2(t-\tau)\right]E_o(t)E_o(t-\tau)\cos\left[\omega\tau - \phi(t) + \phi(t-\tau)\right] +$$

$$+2E_o^2(t)E_o^2(t-\tau)\cos 2\left[\omega\tau - \phi(t) + \phi(t-\tau)\right]\}dt,$$

where $\phi(t)$ is the phase of the pulse as described in both Chapter 4 as well as Chapter 3.

We used an interferometric autocorrelator when adjusting the prism separation in our Ti:sapphire so as to eliminate the chirp and minimize the pulse width. This was done by aligning the two beams in the Michelson interferometer collinearly, while the speaker

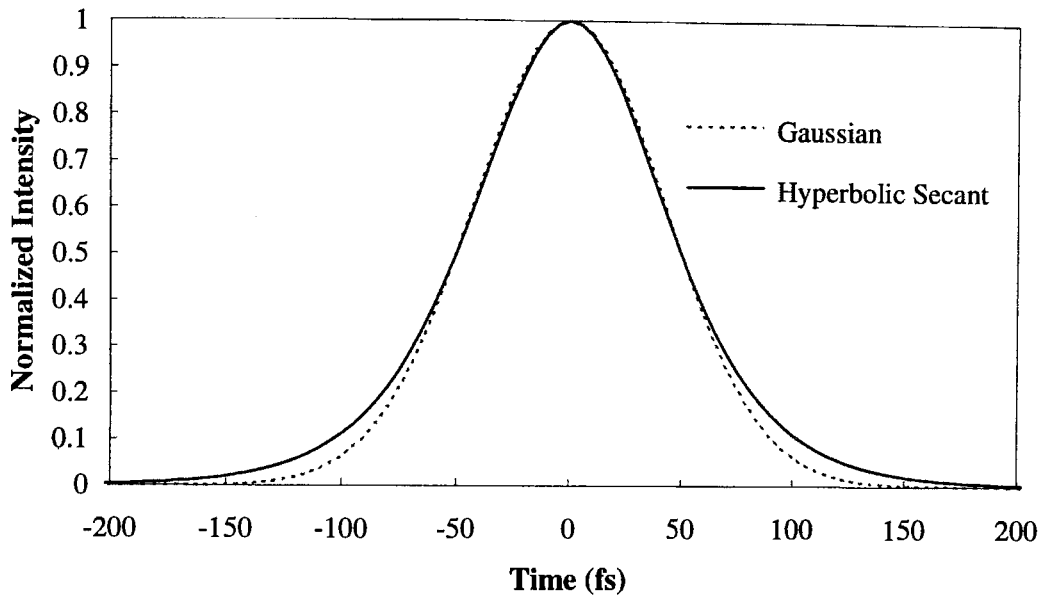

Figure 5.3 Hyperbolic Secant squared pulse versus a Gaussian pulse.

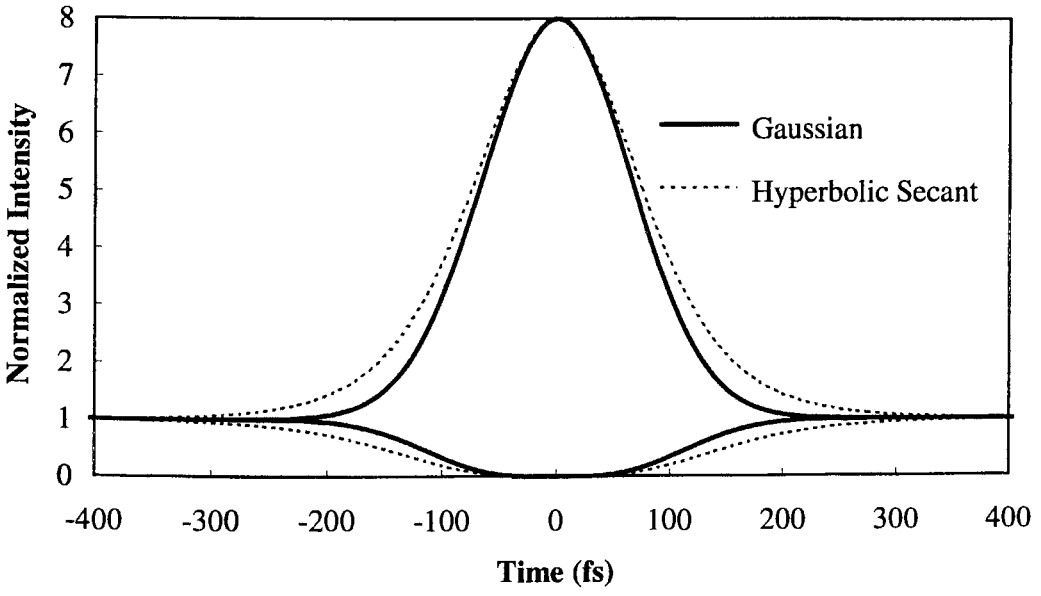

Figure 5.4 Comparison of the envelopes of Gaussian and hyperbolic secant squared interferometric autocorrelation functions.

that modulated the delay in the one arm was modulated slowly. The frequency response of the detector was altered by adjusting a variable resistor to either see or not see the fringes. The entire set up can be seen in **Figure** (5.5), whereas **Figure** (5.6) and **Figure** (5.7) show both the theoretical and experimental interferometric autocorrelation of a 100 femtosecond (FWHM), chirp free pulse.

Additionally, we originally had difficulty achieving the optimal 8 to one peak to background ration experimentally, although the autocorrelation did not appear chirped. We thought that our unequal beam ratio of 5 to 4 or possible poor alignment caused this discrepancy. However, as seen in **Figure** (5.8) a moderate deviation between the

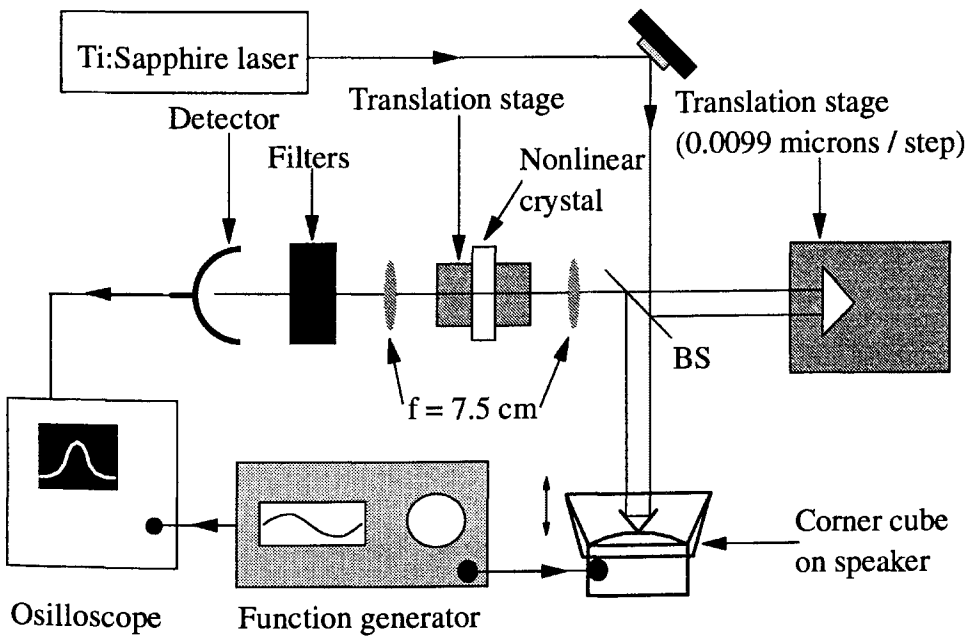

Figure 5.5 Interferometric autocorrelation set up for the measurement of femtosecond pulses.

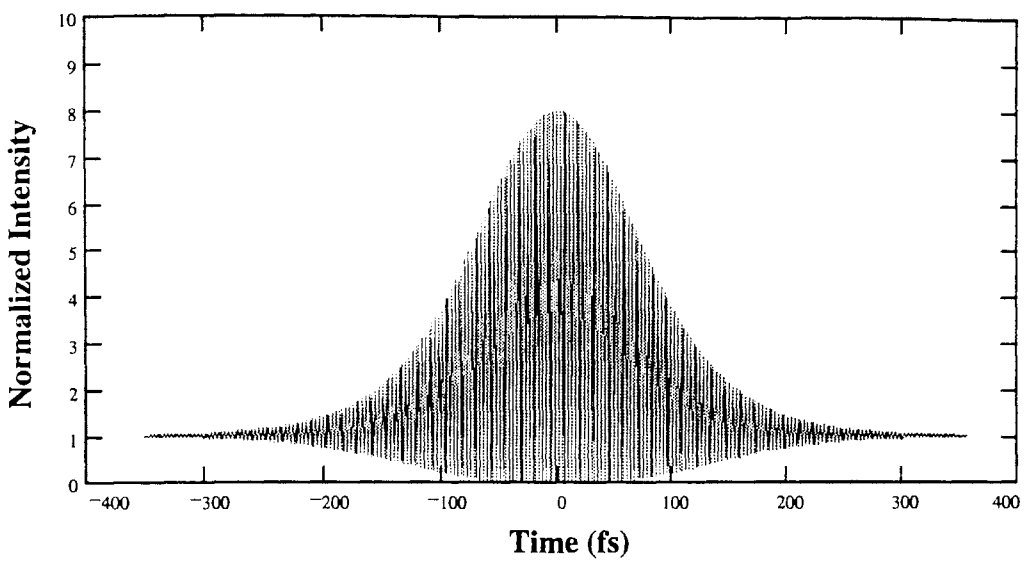

Figure 5.6 Theoretical plot of the interferometric autocorrelation function for a hyperbolic secant squared shaped pulse with a 100 fs FWHM.

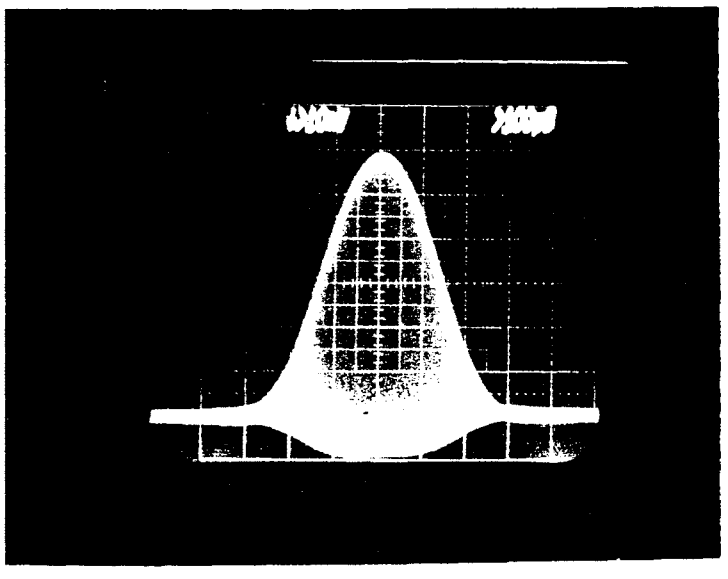

Figure 5.7 Experimental interferometric autocorrelation of an a 100 fs hyperbolic secant squared shaped pulse with approximately an 8 to one peak to background ratio.

intensities of the two beams has a minor effect on the peak to background ratio. For the most part it was not the critical alignment that caused this problem either, rather it was mostly caused by the detection and electronics.

We did not perform accurate pulse width measurement with this system, when it was fast or fringe resolved, because the autocorrelation was altered too much by the addition of a glass slide into one path. Instead, we usually altered the impedance seen by the detector with a variable resistor and measured the pulse width of the fringe averaged autocorrelation function. We regularly obtained pulses of around 100 femtoseconds at wavelengths from 780 - 850 nm.

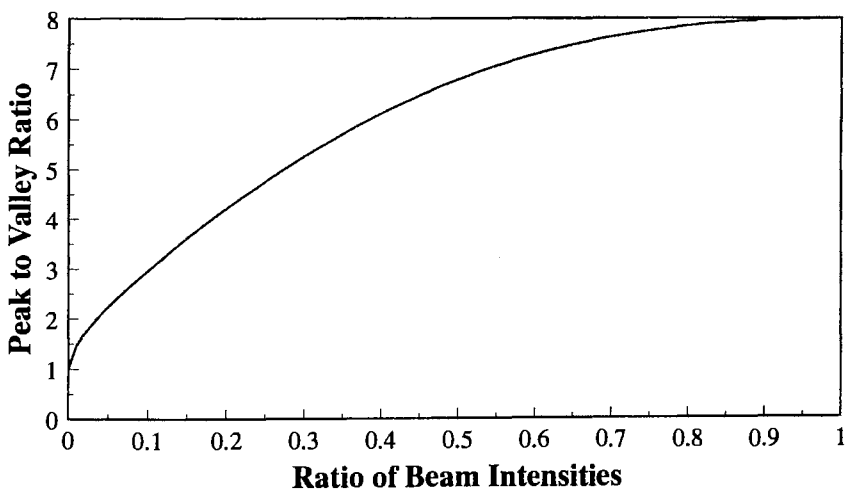

Figure 5.8 The peak to background ratio of a $sech^2$ interferometric autocorrelation versus the beam intensity ratio.

5.3.2 Background Free Autocorrelation

In a background free autocorrelation the two beams are sent into the nonlinear crystal, so that only when the K-vectors of the two beams add together will the phase

matching condition be met. This can be achieved by sending the two beams into the crystal collinearly with opposite polarizations, or by sending them in noncollinearly at the proper angles of incidence. The method used primarily depends upon the nonlinear crystal available and the users preference.

In any event, both the pulses must be coincident temporally, or there will be no second harmonic generated in the direction of the net K-vector. Therefore, it is easier to determine the correct path difference when aligning the autocorrelator. However, the main benefit of the background free autocorrelator is that there should be no background signal when the delay between the pulses is large, therefore any signal must be due to cw noise in the laser [15].

We wanted to be able to monitor the pulse width of a Nd^{3+}:YLF laser in real time, while we were optimizing the pulse width. Although the laser was acousto optically modulated and capable of 50-80 picosecond pulses, the laser would generate pulse widths in the hundreds of picoseconds when the cavity length was wrong. However, we wanted one device that could cheaply and efficiently measure the pulse width over the entire pulse width range. Although photodiodes could easily detect and measure the longer pulses, only the most expensive photdiodes would be of any use with the shorter 50 - 80 picosecond pulses. On the other hand, it is difficult for real time autocorrelators to measure the longer pulse widths, because of the large path differences that must be generated. However, real time autocorrelators have been made with large path differences, including some very expensive commercial systems. Therefore, our solution was to build a noncollinear background free autocorrelator that was capable of measuring path differences of up to one nanosecond. The one nanosecond time delay required that the path length of the modulating arm of the Michelson interferometer be altered by a foot at its maximum. The pulse in the modulating arm was bounced off the moving prism,

before it hit a second prism and returned to the beam splitter. Therefore, the modulating arm was quadruple passed instead of the usual double pass. Additionally, with the aid of a rotating motor and aluminum rod, the stage that held the first prism was translated one and one half inches. Therefore, with the quadruple pass we obtained one half foot of change in path delay, so that temporal delays of up to one half nanosecond could be added between the incident pulses. The entire experimental set up is shown in **Figure** (5.9).

We used two different methods to obtain the pulse widths from the Nd^{3+}:YLF laser, so as to increase the accuracy of the measurement. The path delay is proportional to the cosine of the time delay on the scope, and we will assume that our pulses are short enough so that they are within the linear region of movement towards the center of the travel of the stage. The change in path length was one half foot, therefore there is a full one foot path difference or about one nanosecond time delay between three autocorrelation traces. Additionally, the linear region of the movement has a slope of $\pi/2$ times that of the average slope over the entire range of movement. Therefore, from the oscilloscope traces shown in **Figure** (5.10), we can tell that the separation between three autocorrelation traces is about 8.1 divisions and that one division is equivalent to about 194 ± 10 picoseconds. Hence, the Full Width at Half Maximum(FWHM) of the autocorrelation, which is about 1.2 division must be around 232.7 picoseconds and the FWHM of the actual pulse width is about 165 picoseconds. The second method that we used included adding a .25"$\pm$.001" path delay in the unmodulated arm of the interferometer, and using the shift as our time calibration. The .25" change in path delay caused a shift of about $0.25 \pm .05$ divisions in either direction of the central pulse shown in **Figure** (5.5) with respect to the outer pulses. From this, one division on the oscilloscope is equivalent to 169 picoseconds, and the FWHM of the autocorrelation of 1.2 divisions equals 203 picosecnds. Therefore, the FWHM of the pulse as estimated from this method

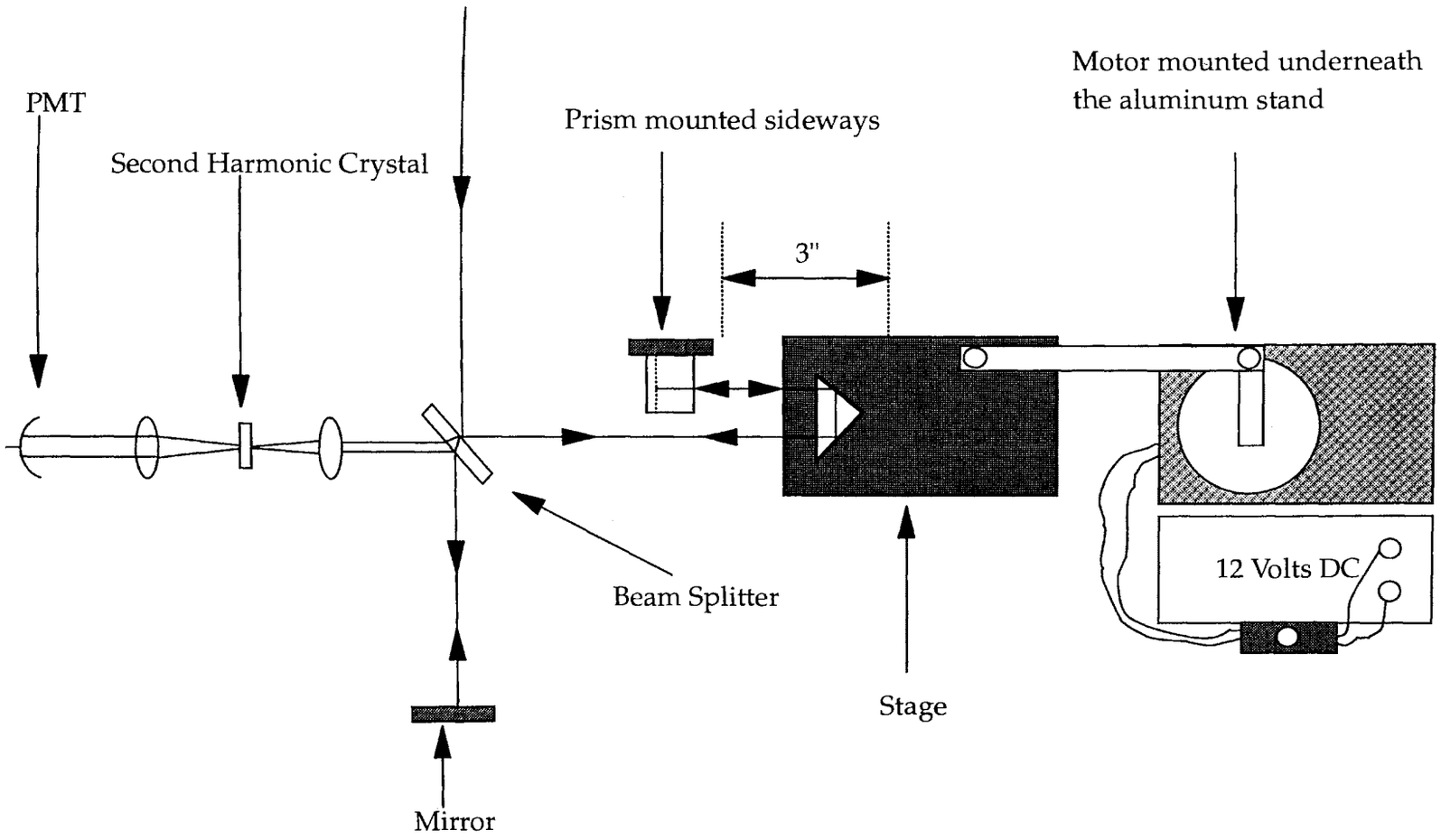

Figure 5.9 Noncollinear background free nanosecond autocorrelation set up.

is 144 picoseconds. So, the pulses shown in **Figure** (5.10) were probably about 160 picoseconds, and **Figure** (5.11) shows the output of the autocorrelator with the oscilloscope trace of a single autocorrelation. Additionally, with more tweeking of the laser, we were able to measure pulses in the 50-80 picosecond regime, however the laser was much less stable under those conditions. On the other hand, **Figure** (5.12) shows the output from our fastest photodetector-oscilloscope combination, which was a small area silicon photodiode and the sampling head a Tektronix 7834 storage scope. It can be seen that the pulse width is actually smaller than the maximum resolution as determined by the time constants of the electronics. Still, the photodiode-oscilloscope combination is sensitive enough to show that the pulses are probably about 100 picoseconds or so, which can be very useful with longer pulses and when the laser is first being aligned.

After these measurements were taken, we replaced the 0.75" arm on the turning motor with a 1.25" one. Therefore, the range of motion of the stage in one direction increased from 1.5" to about 2.625 ± 0.05", so that spatial delays of 10.5 inches or temporal delays of almost 1 nanosecond could be obtained.

a)

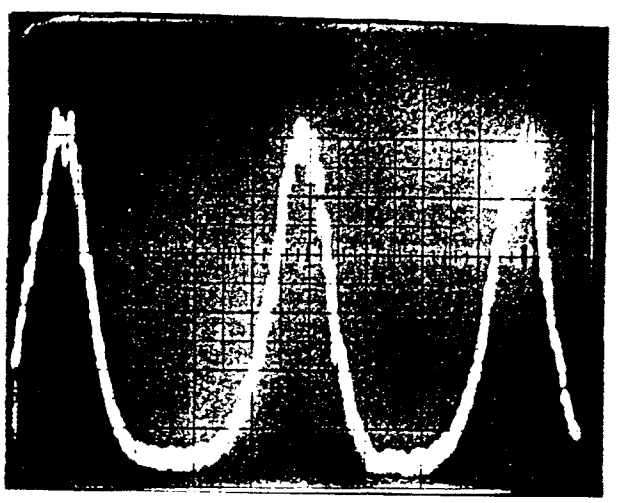

b)

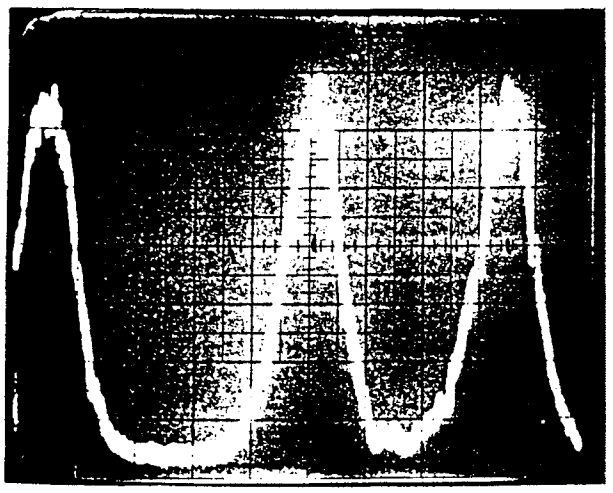

Figure 5.10 Autocorrelation traces that were used to calibrate the system. a) No extra path delay b) .25" path delay added to stationary arm.

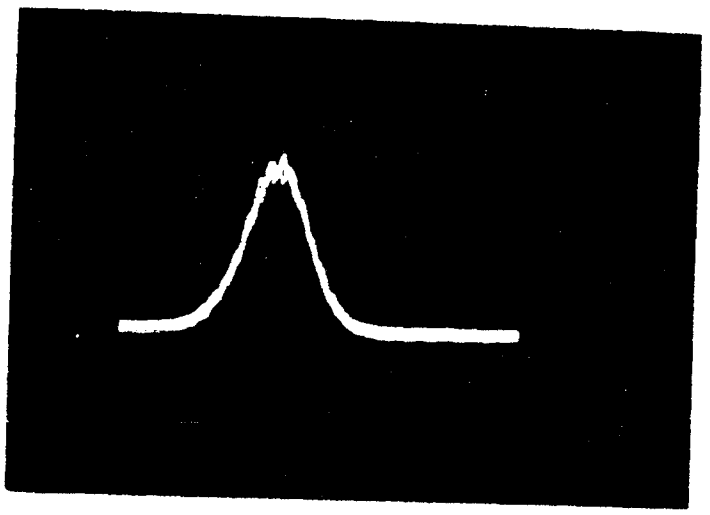

Figure 5.11 Output for single autocorrelation trace.

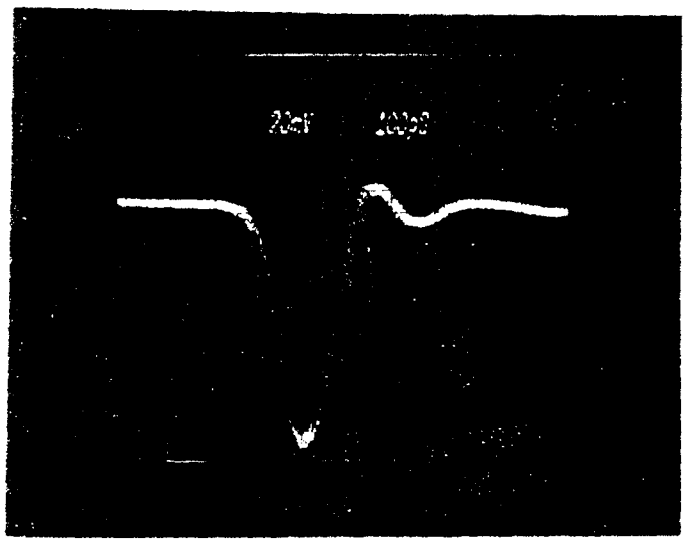

Figure 5.12 Output from scope when a fast photodiode is used.

5.3.3 Single Shot Autocorrelation

When using a low repetition rate laser, it is not possible to implement real time autocorrelators. Additionally, the traditional autocorrelation methods take significant time to implement, hence immediate feedback is not possible. However, constant or at least frequent pulse width observation is sometimes desirable as in the case of supercontinuum production. Implementing a single shot autocorrelator with a nonlinear crystal can be an effective solution. Using a thin second harmonic crystal it is possible to measure pulses shorter than 100 femtoseconds with only one pulse by transforming the temporal shape of the pulse into spatial information. This is done by crossing two magnified beams in the nonlinear crystal at a small angle so that the small temporal overlap is transformed into a spatial overlap that is large enough for a CCD array to resolve. The relationship between the temporal width and spatial overlap was derived by Jansky et al. [16], such that for two incident pulses $I_1(t)$ and $I_2(t)$ at an angle of ϕ with respect to each other the temporal shape is given by

$$S(x) \propto \int_{-\infty}^{\infty} I(t+\tau)I(t-\tau)dt = G_2(2\tau) \qquad (5.14)$$

where the delay is related to n the index of the nonlinear medium, and x_o the horizontal distance in x from the central maximum of the spatial second harmonic profile by

$$\tau = \frac{nx_o \sin(\phi/2)}{c}. \qquad (5.15)$$

Hence, a shift in temporal delay between the pulses shifts the spatial second harmonic pattern by

$$\Delta x_o = \frac{c\Delta t_o}{2n\sin(\phi/2)}. \qquad (5.16)$$

A schematic of the relation between τ and x_o as obtained from Salin et al. [17] is shown in **Figure** (5.13). Since, S(x) is proportional to the second order intensity autocorrelation function, we can easily obtain the FWHM of the temporal autocorrelation by calculating or determining experimentally, the ratio between Δx_o and Δt. Furthermore, methods have been demonstrated that generate phase sensitive [18] and interferometric autocorrelations [2], [19], however we made no attempt to implement them.

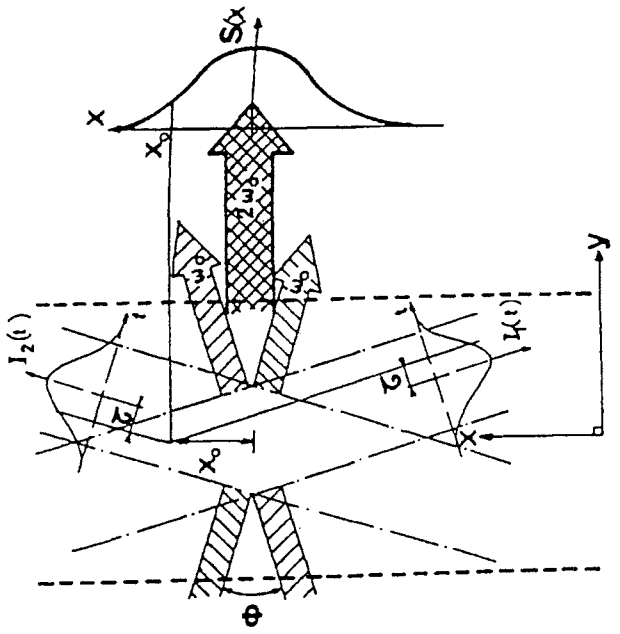

Figure 5.13 Interaction of two femtosecond beams in a nonlinear crystal [19].

To transform the temporal shape of the pulse into a spatial profile a beam splitter is used to split the pulse into two identical pulses, which are crossed in the frequency doubling crystal with no path difference. The second harmonic is then imaged unto the CCD array. Normally, if the pulses are noncollinear there will only be second harmonic produced when the pulses are coincident both temporally, and spatially. For this experiment, we used a thin crystal so as to minimize GVD and beam walk off, therefore the two individual beams were phase matched at the same time as the noncollinear autocorrelation was. Therefore, we saw three blue beams with the central one being the autocorrelation.

The autocorrelation was performed without the aid of lenses prior to the nonlinear crystal, because they would lengthen the pulse. Therefore, we split the initial pulse into two identical pulses, by sending it onto a 50/50 beam splitter at a 45 degree angle of incidence. In this manner, we were able to keep the path lengths of the two pulses equal and direct them onto the frequency doubling crystal with only one mirror for each branch. The total angle between the two beams was about .1 radians(6 degrees), with the mirror separation being about 4 inches and their distance from the frequency doubling crystal being around 40 inches. The complete set up that we used to implement the single-shot autocorrelation, while measuring the output of the Cr:LiSAF regenerative amplifier is shown in **Figure** (5.14).

We used a 400 micron thick Lithium Iodate crystal cut so as to frequency double the 850 nm laser light. The spatial intensity profile created at the crystal was then one to one imaged unto the CCD array with a 15 cm lens. There were also some BG 38 filters used to block the incident 850 nm and some neutral density filters used to attenuate the doubled 425 nm light so as not to damage the CCD array or saturate the image. A two dimensional CCD array was used as a beam profiler, so that we could measure both the

spatial and temporal properties of the beam. The two dimensional image obtained is shown in **Figure** (5.15), where the horizontal width corresponds to the temporal pulse width and the vertical corresponds to the pulse shape.

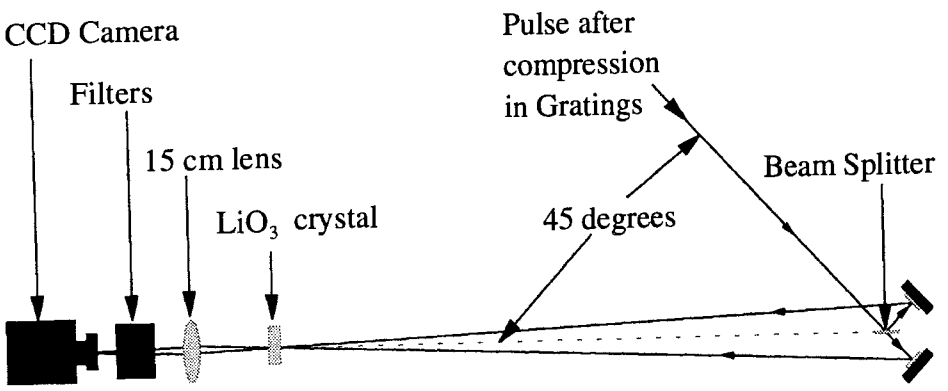

Figure 5.14 Single shot autocorrelation set up.

Now, to calibrate our measurement system we placed a 150 micron thick microscope cover slide, which is made of soda lime glass n=1.50, into one of the beam paths and noted the change on the CCD array. This was then repeated with the other beam for increased accuracy. The calibration formula is

$$\frac{\Delta_{glass}}{FWHM} = \frac{\Delta X_{shift}}{\Delta X_{FWHM}}, \qquad (5.17)$$

so that

$$FWHM = \frac{\Delta_{glass} \times \Delta x_{FWHM}}{\Delta x_{shift}} \qquad (5.18)$$

a)

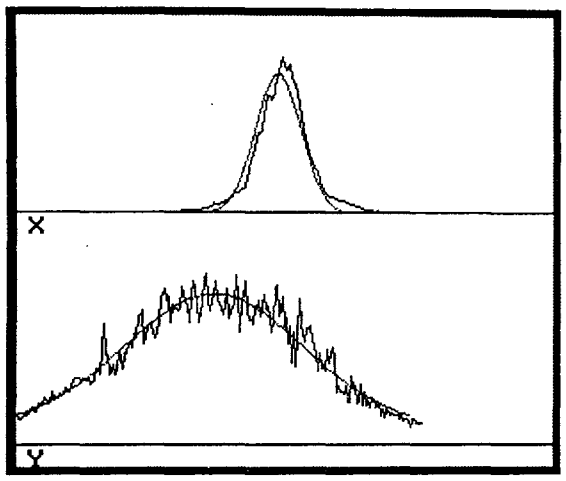

b)

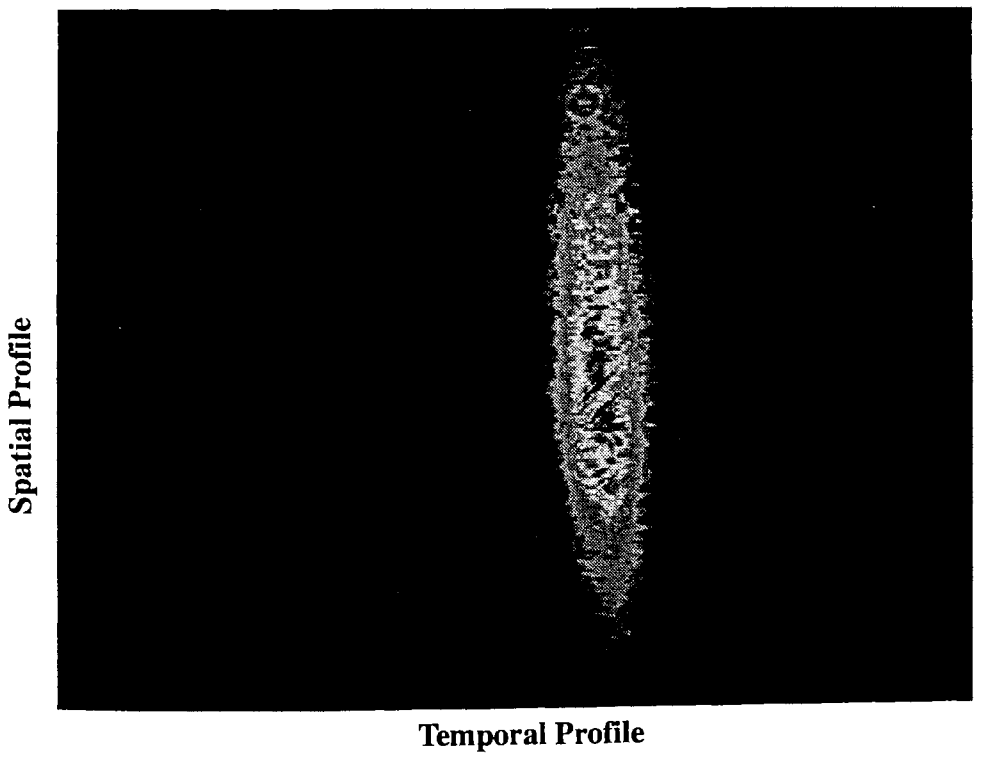

Figure 5.15 Beam profile obtained from the CCD array while measuring a 113 fs pulse with the single shot autocorrelator. a) Beam profiles. b) Two dimensional image.

where the quantities are defined below.

Δ_{glass} = actual time delay caused by the cover slide,
FWHM = autocorrelation' s full width at half maximum,
ΔX_{shift} = shift of pulse on CCD
ΔX_{FWHM} = FWHM of pulse on CCD array

For our microscope cover slide:

$$\Delta t_{glass} = \frac{(n-1)d}{c} = \frac{(1.5-1)\times 150\times 10^{-6}}{3\times 10^{8}} = 250\text{fs}, \qquad (5.19)$$

and the ratio of ΔX_{FWHM} to ΔX_{shift} was 0.7. Therefore, the FWHM of the autocorrelation was about 175 femtoseconds, and by assuming a $sech^2$ intensity profile, we estimate that the pulse width was around 113 femtoseconds. Since, we averaged two readings and placed an accurately measured slide into the beam perpendicularly, we feel that this measurement is correct to within ± 5 femtoseconds.

5.4 Cross Correlation System

After generating an Ultra-fast Supercontinuum Laser Source(USLS), we needed a method by which to characterize the spectrum with respect to its temporal position in the pulse. We decided to do this with a cross correlation system that consists of the 850 nm beam and the output of the USLS focused upon a nonlinear crystal at near normal incidence. We intended to look at the spectrum of the sum frequency of the two pulses on a spectrometer for various amounts of delay between the two pulses. Therefore, in addition to the temporal delay we would also obtain the relative intensity with respect to wavelength for the USLS. The nonlinear crystal needed to be very thin so as to avoid the group velocity dispersion in the USLS beam, minimize the beam walk off, and allow a broad phase matching frequency range. The GVD could be corrected for later in the

analysis, so that would not be a major problem. However, we intended to angle tune the crystal, because we did not want to invest the extra money for the equipment needed for temperature tuning, so beam walk off and phase matching conditions were a concern.

Our main goal was to characterize the continuum over the largest spectral range possible, with priority given to the 400 nm to 1000 nm range. Now, the crystal companies usually sell crystals for second harmonic generation or optical parametric oscillation at very common frequencies, but they were of little use in determining the proper crystal and cut for the sum generation of an 850 nm pump beam with wavelengths over the 400 nm to 1000 nm range. Therefore, we needed to determine the crystal and cut that would be angle tunable with a relatively high d_{eff} over the range of wavelengths needed for the sum frequency generation. Then we could negotiate the price for the crystal after giving the exact specifications to the vendor.

We intended to send the continuum and the 850 nm pump beam into the crystal at nearly normal incidence with a variable path or time delay between the two beams. The crystal would then be on a rotating stage so that it could be angle tuned, and BG 38 filters would be used to filter out the 850 nm pump light before the fiber optic cable of the Ocean Optics Spectrometer was used to detect the signal. We then could detect the wavelength and relative strength of the sum frequency light versus the temporal delay between the beams to determine the chirp of the white light continuum. The set up is shown in **Figure** (5.16).

The three materials that we looked at using were potassium dihydrogen phosphate (KDP), lithium borate (LBO), and barium borate (BBO). We tried KDP because, it is a readily available crystal, and Fork et al. [20] had used it to characterize the femtosecond continuum that they produced at 620 nm. Dr. Torrelas recommended the LBO, because

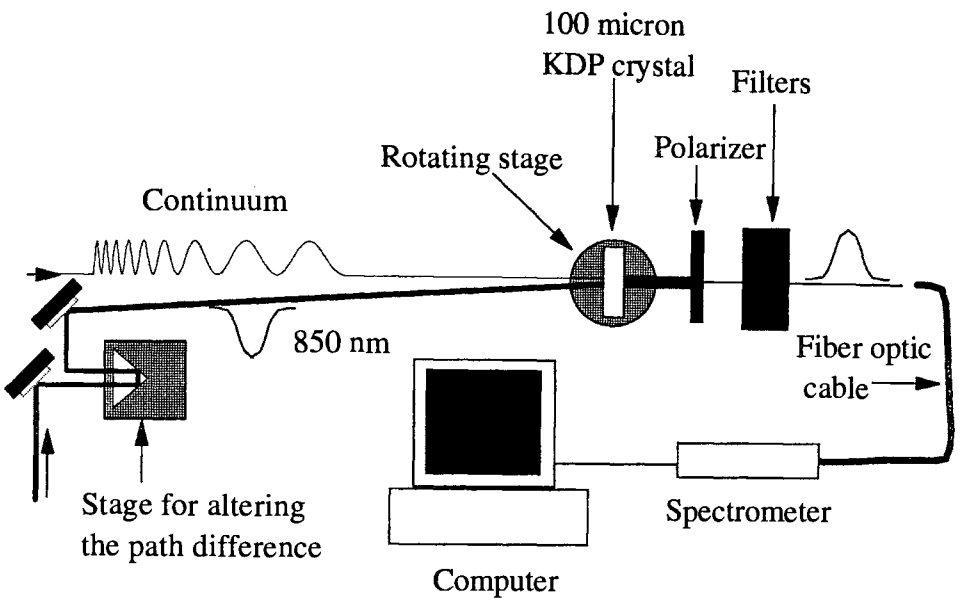

Figure 5.16 Proposed set up for characterizing the dispersion of the USLS.

individuals have successfully generated optical parametric oscillators(OPO) over a large spectral regions in the visible and infrared with them [21], and the Borate crystals are better for temperature tuning than KDP [22], [23]. However, as mentioned earlier, we decided to use angle tuning, therefore one of the prime benefits of the LBO and BBO(temperature tuning capability) was no longer valid.

Therefore, I went ahead and calculated the tuning angle for various continuum input wavelengths for type I phase matching of KDP. Meanwhile, Dr. Torrelas calculated basically the same thing for Type I phase matching with LBO, as well as all Type I, Type IIa, and Type IIb phase matching with KDP. The phase machining conditions were determined numerically with the basic equations given in Chapter 2, along with the dispersion equations for the materials. The numerical solutions were obtained with MathCad and/or MatLab, where the plots shown are the ones performed by Dr. Torrelas

with MatLab. **Figure** (5.17) and **Figure** (5.18) show the dispersion curves for LBO [24] and KDP [25] respectively, that were determined from their respective Seillmier equations. **Figure** (5.19) shows both the input continuum wavelength and the generated wavelength for LBO sum frequency Type I phase matching versus internal angle of incidence. The same information is shown in **Figure** (5.20) for KDP Type I (w-o, p-o, s-e), **Figure** (5.21) for KDP Type IIa (w-o, p-e, s-e), and **Figure** (5.22) for KDP Type IIb (w-e, p-o, s-e) phase matching. Where, for w, p, and s denote the white light, 850 pump and signal and o or e represent whether they are ordinary or extraordinary waves. The KDP Type IIa and Type IIb phased matched crystal did not meet our tuning range requirements and were withdrawn from consideration immediately, whereas the LBO and KDP Type I phase matching did. Although, the d_{eff} of the LBO was larger over much of the spectrum, it was about the same in the higher frequency region where it would be most needed due to the lower continuum output in that region. Additionally, KDP was phase matchable at higher frequencies(Type I) than LBO(Type I), and KDP has a smaller GVD than that of LBO in the visible region as shown in **Figure** (5.23). The primary reason for choosing KDP over Dr. Torrelas's recommendation of LBO was that we were able to quickly and cheaply obtain a 100 μm thick piece of KDP cut at an angle of 60 degrees.

Since, we were using a Type I phase matching, both the incident beams have a polarization opposite to the output beam. This is very useful, because the large amount of energy from the continuum and 850 nm pump beam can be eliminated without attenuating the power of the sum frequency beam that we want to detect.

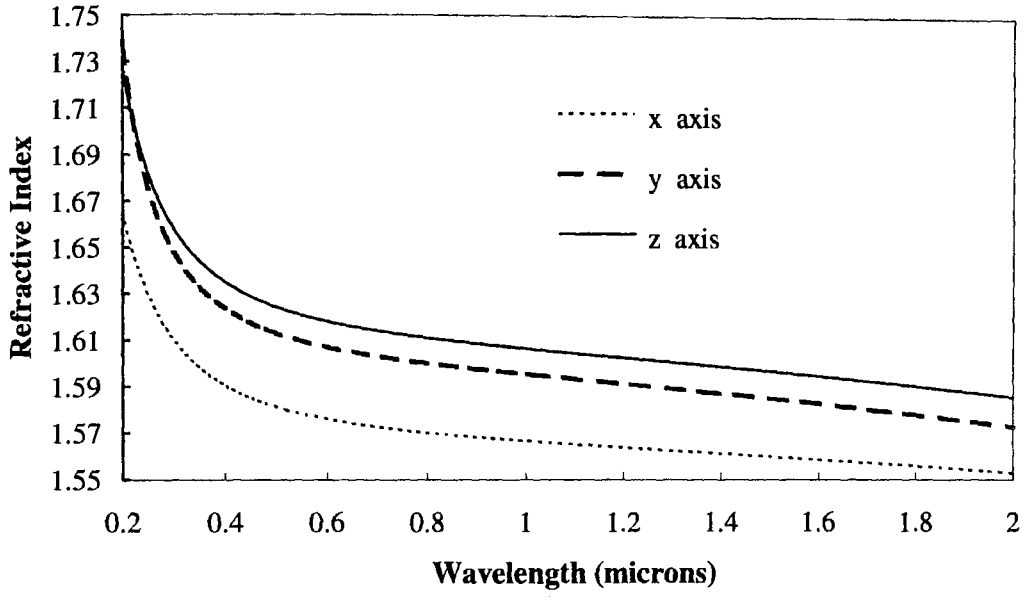

Figure 5.17 Dispersion of LBO with the refractive index plotted versus wavelength in microns.

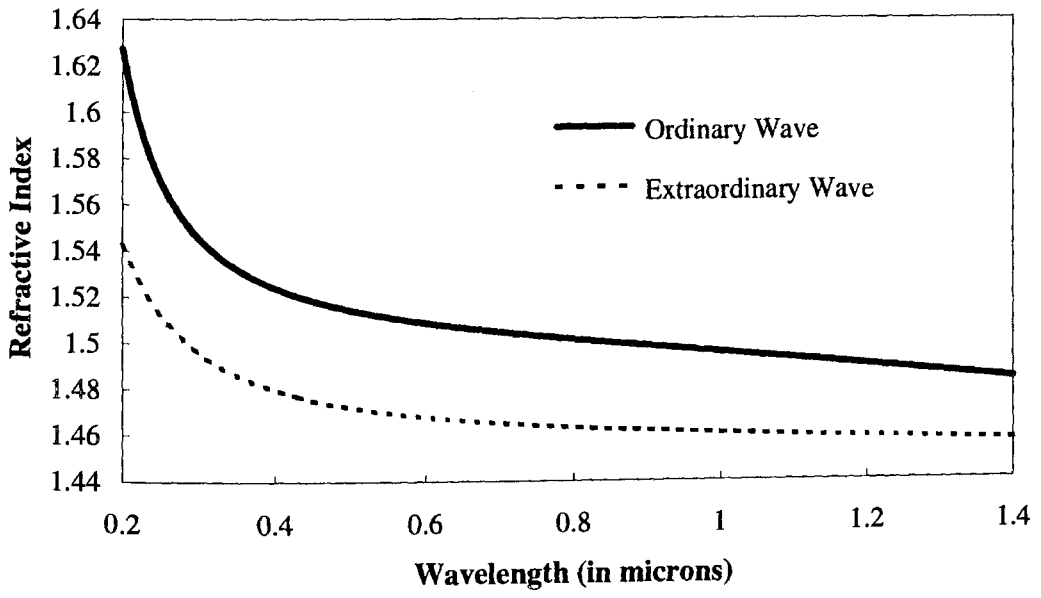

Figure 5.18 Dispersion of KDP with the refractive index plotted versus wavelength in microns.

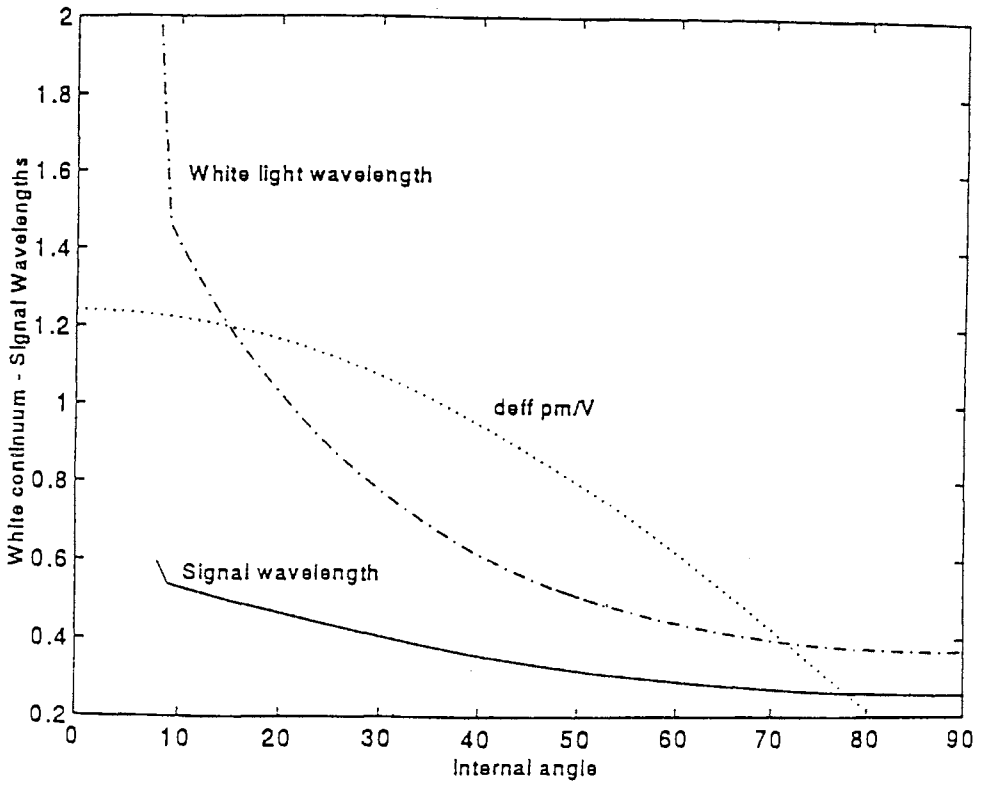

Figure 5.19 Plot of the phase matching conditions for LBO type I sum frequency generation with the supercontinuum wavelength, signal wavelength generated, and d_{eff} in pm/V versus internal angle.

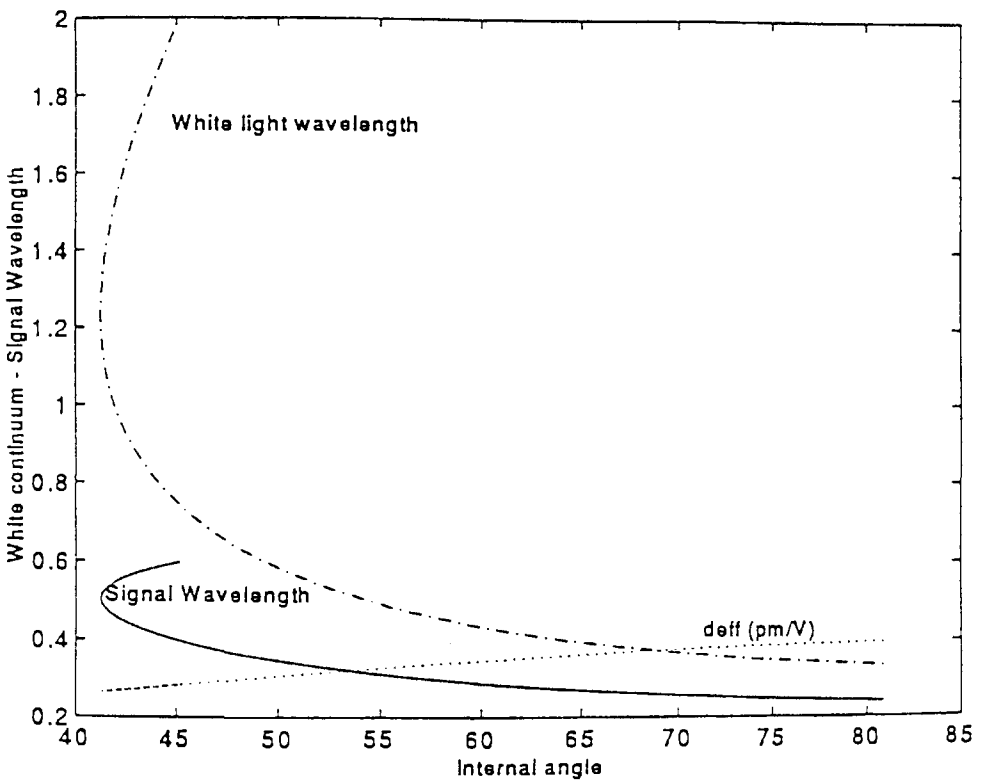

Figure 5.20 Plot of the phase matching conditions for KDP type I sum frequency generation with the supercontinuum wavelength, signal wavelength generated, and d_{eff} in pm/V versus internal angle.

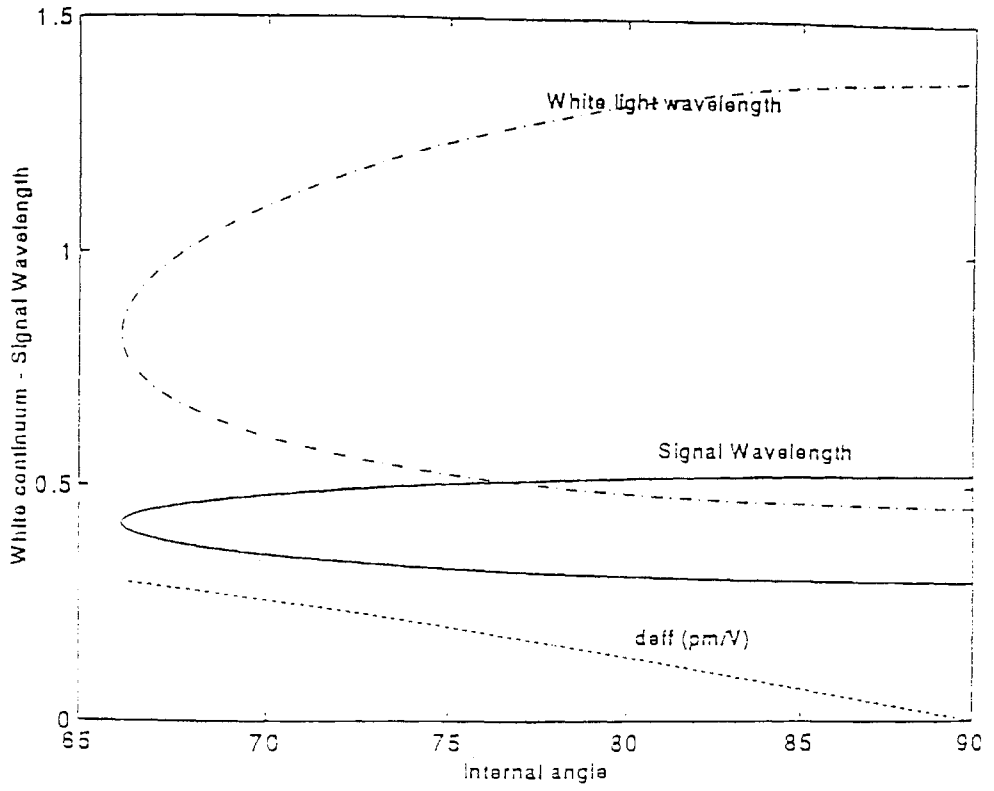

Figure 5.21 Plot of the phase matching conditions for KDP type IIa sum frequency generation with the supercontinuum wavelength, signal wavelength generated, and d_{eff} in pm/V versus internal angle.

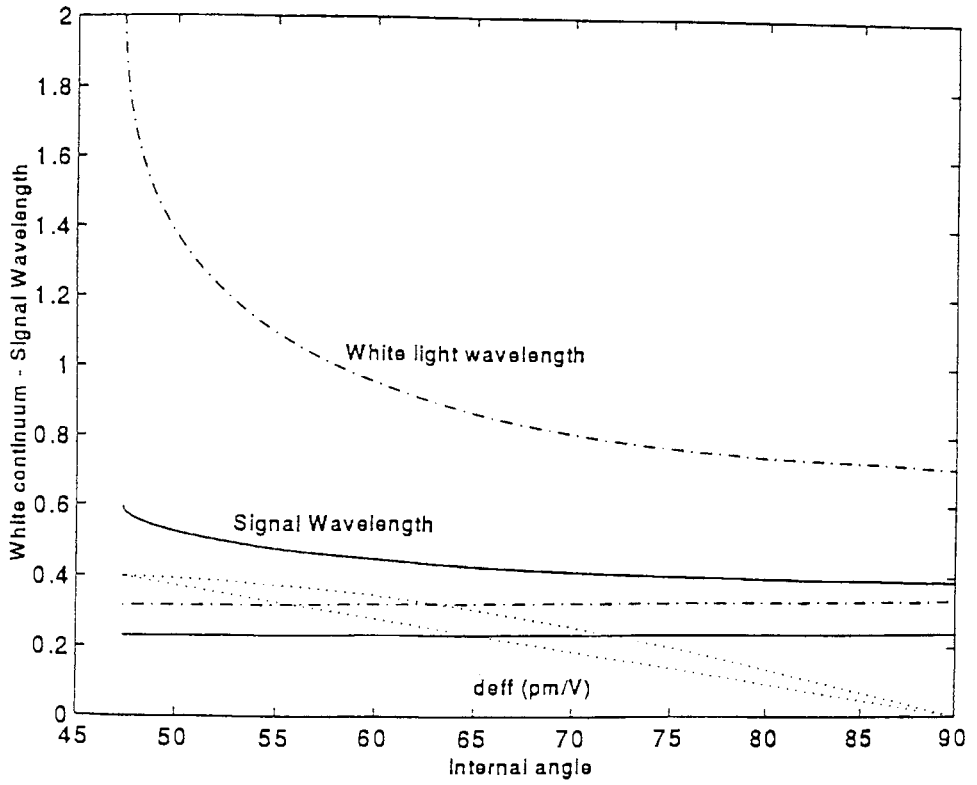

Figure 5.22 Plot of the phase matching conditions for KDP type IIb sum frequency generation with the supercontinuum wavelength, signal wavelength generated, and d_{eff} in pm/V versus internal angle.

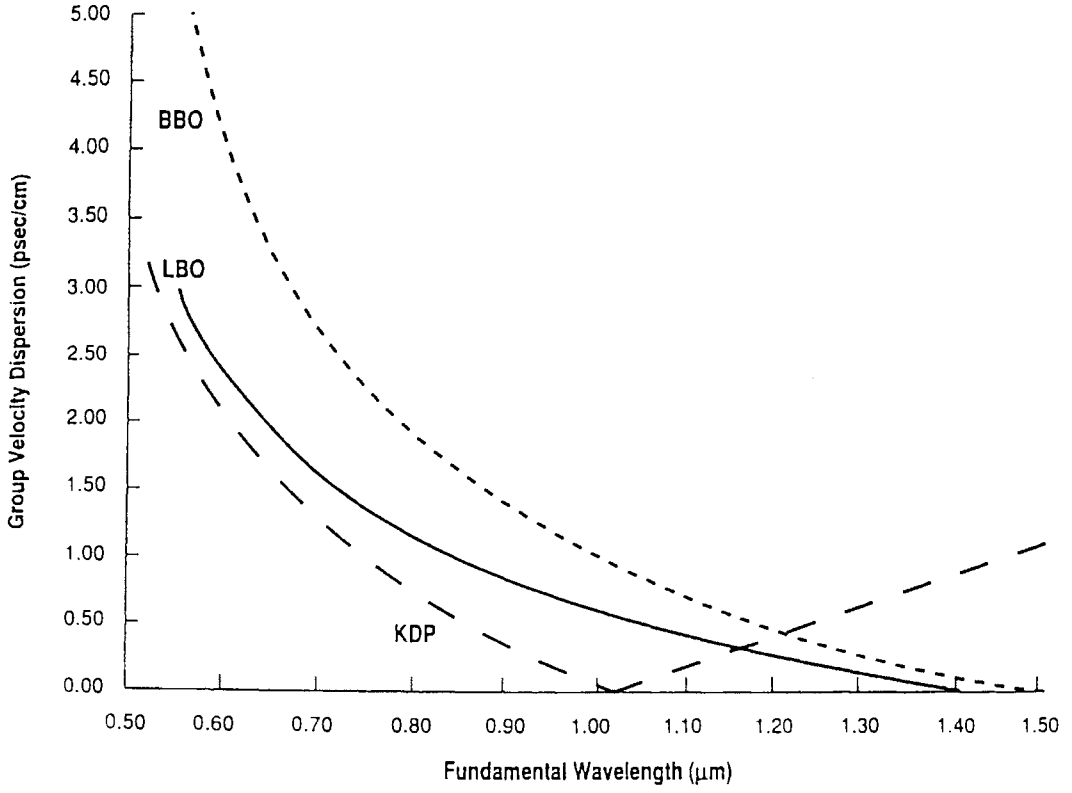

Figure 5.23 Comparison of the group velocity dispersion for KDP, BBO, and LBO given in picoseconds of delay per cm of crystal length as a function of the fundamental wavelength [26].

REFERENCES FOR CHAPTER 5

[1] D. J. Bradley, in Ultrashort Light Pulses, "Picosecond Techniques and Applications", p. 23 (S. l. Shapiro, ed.) Springer-Verlag, New York, 1977.

[2] A. Brun, P. Georges, G. Le Saux, and F. Salin, "Single-shot characterization of ultrashort light pulses", *Appl. Phys.* **24**, 1225-1233 (1991).

[3] G. P. Agrawal, Nonlinear Fiber Optics, pp. 180-186, Academic Press Inc., San Diego, 1989.

[4] J. Motowski, and M. G. Raymer, in Contemporary Nonlinear Optics (G. P. Agrawal, and R. W. Boyd, ed.), pp. 177-178, Academic Press, Inc., San Diego, 1992.

[5] K. L. Sala, G. A. Kenney-Wallace, and G. E. Hall, "CW Autocorrelation Measurements of Picosecond Laser Pulses," *IEEE J. Quantum Electron.*, **QE-16**, 990-996 (1980).

[6] J-C. M. Diels, J. J. Fontaine, I. C. McMichael, and F. Simoni, "Control and Measurement of ultrashort pulse shapes (in amplitude and phase) with femtosecond accuracy," *Appl. Opt.* **24**, 1270-1282 (1985).

[7] J. -C. Diels, J. J. Fontaine, and W. Rudolph, "Ultrafast diagnostics," *Revue Phys. Appl.* **22**, 1605-1611 (1987).

[8] E. P. Ippen, and C. V. Shank, in Ultrashort Light Pulses, "Picosecond Techniques and Applications," p. 86 (S. l. Shapiro, ed.) Springer-Verlag, New York, 1977

[9] R. J. Harrach, "Determination of Ultrashort Pulse Widths by Two-Photon Flourescence Patterns," *Appl. Phys. Lett.* **14**, 148 (1969).

[10] D. H. Auston, "Second Order Intensity Correlations of Optical Pulses," *IEEE Journal of Quant. Electron.* **QE-7**, 465-467 (1971).

[11] D. H. Auston, "Measurement of Picosecond Pulse Shape and Background Level," *Appl. Phys Lett.* **18**, 249-251 (1971).

[12] J. -C. Diels, J. J. Fontaine, and W. Rudolph, "Ultrafast diagnostics," *Revue Phys. Appl.* **22**, 1605-1611 (1987).

[13] J.-C. Diels, E. W VanStryland, and D. Gold, "Investigation of the Parameters Affecting Subpicosecond Pulse Durations in Passively Mode Locked Dye Lasers", in Picosecond Phenomena, pp. 117-120 (ed. C. V. Shank, E. P. Ippen, S. L. Shapiro) Springer Series in Chemical Physics 4 Springer-Verlag, Berlin Heidelberg, 1978.

[14] J.-C. Diels, in Dye Laser Principles (F. J. Duarte, and L. W. Hillman, ed.) pp. 103-115, Academic Press, Inc., San Diego, 1990.

[15] E. P. Ippen, and C. V. Shank, in Ultrashort Light Pulses, "Picosecond Techniques and Applications," pp. 90-92 (S. l. Shapiro, ed.) Springer-Verlag, New York, 1977

[16] J. Janskzy, G. Corradi, R. N. Gyuzalian, "On a possibility of analysing the temporal characteristics of short light pulses," *Opt. Comm.* **23**, 293-298 (1977).

[17] F. Salin, P. Georges, G. Roger, and A. Brun, "Single-shot measurement of a 52-fs pulse," *Appl. Opt.* **26**, 4528-4531 (1987).

[18] G. Szabo, Z. Bor, and A. Miller, "A Phase Sensitive Single Pulse Autocorrelator for Ultrashort Laser Pulses," in Ultrafast Phenamena VI (T. Yajima, K. Yoshihara, C.. B. Harris, and S. Shionoya ed.) pp. 146-148, Springer-Verlag, Berlin, Heildelberg, 1988.

[19] F. Salin, P. Georges, G. Le Saux, G. Roger, and A. Brun," *Revue De Physique Appliquee*. **22**, 1613-1617 (1987).

[20] R. L. Fork, C. V. Shank, C. Hirlmann, R. Yen, and W. J. Tomlinson, "Femtosecond white-light continuum pulses," *Opt Lett.* **8**, 1-3 (1983).

[21] J. Y. Zhang, J. Y. Huang, Y. R. Shen, and C. Chen, "Optical parametric generatino and amplification in barium borate and lithium triborate crystals," *J. Opt. Soc. Am. B* **10**, 1758-1763 (1993).

[22] N. P. Barnes, D. J. Gettemy, and R. S. Adhav, Variation of the refractive index with temperature and the tuning rate for KDP isomorphs," *J. Opt. Soc. Am.* **72**, 895-898 (1982).

[23] F. Hanson, and D. Dick, "Blue parametric generation from temperature-tuned LiB_3O_5," *Opt. Lett.* **16**, 205-207 (1991).

[24] S. Lin, J. Y. Huang, J. Ling, C. Chen, and Y. R. Shen, "Optical parametric amplification in a lithium triborate crystal tunable from 0.65 to 2.5 μm," *Appl. Phys. Lett.* **59**, 2805-2807 (1991).

[25] F Zernike JR., "Refractive Indices of Ammonium Dihydrogen Phosphate and Potassium Dihydrogen Phosphate between 2000 A and 1.5 μm," ," *J. Opt. Soc. Am.* **54**, 1215-1220 (1964).

[26] J. Motowski, and M. G. Raymer, in Contemporary Nonlinear Optics (G. P. Agrawal, and R. W. Boyd, ed.), pp. 177-178, Academic Press, Inc., San Diego, 1992.

CHAPTER 6

PULSE DELAY MODULATION TECHNIQUES

The Pulse Delay Modulation Technique(PDMT) was developed as a modified direct transmission measurement technique for measuring two-photon absorption in bulk materials and thin films. There are two main advantages of using measurement techniques based on Pulse Delay Modulation(PDM) over direct transmission methods. First of all, there is a greater signal to noise ratio, which generates a greater sensitivity. Secondly, irradiance dependent nonlinearities can be independently measured even while in the presence of large thermal nonlinearities. The PDMT that we implemented is based on the technique developed by Miller et al. [1], which is based on earlier Raman spectroscopy frequency modulation techniques [2], [3], [4], [5], [6], [7].

6.1 Overview and Set-up

The PDMT was originally developed so that high repetition rate lasers could be used to consistently measure irradiance dependent nonlinearities, more specifically two photon absorption, within the shot noise limit of the detector even in the presence of huge thermal nonlinearities. In our experiments, the thermal nonlinearities are not as large, as will be shown later, and we have large enough signals so that it is not necessary to reach the shot noise limit. Still, we do want to eliminate thermal nonlinearities, or at least demonstrate that they are insignificant. Similarly, we will use the PDMT to reduce the system's noise and fluctuations. However, we probably did not reach the above shot

noise limit, partially because we used a simpler modulation technique than employed by Miller [1].

The system is basically a Michelson interferometer being used in an interferometric autocorrelation-like set up. Therefore, instead of a mirror in each arm of the interferometer, there is a prism and a corner cube respectively. The prism is on a stepper motor driven stage, and in the prism arm there is an amplitude modulation added to the laser pulse with a chopper wheel. A diagram of the system that we used is shown in **Figure** (6.1). It should be noted that our system is very similar to those that others have used, however there are a few significant differences. For instance, we used a mechanical chopper motor wheel, whereas Miller and others used an electro optic modulator between crossed polarizers. The net difference is that an electrooptic modulator can amplitude modulated the signal from 1 - 100 MHz, as opposed to the maximum frequency that we used of around 2.54 KHz with our mechanical modulator. This is important because the noise of modelocked Ti:sapphire lasers usually extends to near 1 MHz. so that we are probably still dominated by laser rather than shot noise[8]. In the other arm of the interferometer, the corner cube rests upon an oscillating audio speaker, which varies the overlap of the two pulses temporally. The pulse delay between the two pulses is modulated in this arm, hence the term Pulse Delay Modulation(PDM). The PDM is actually a modulation performed in the 20 to 100 Hz range of the combined beams incident intensity. In our case, the frequency range of this oscillation was determined by the time constants of the lock-in amplifiers. On the other hand, in Miller's experiment the frequency range was primarily limited by the capabilities of the speaker. However, both experiments had PDM in them at about the same frequency. After the beams recombine at the beam splitter they are focused into the sample. Then after passing through another lens and some optical filters the beam is incident upon a photodiode

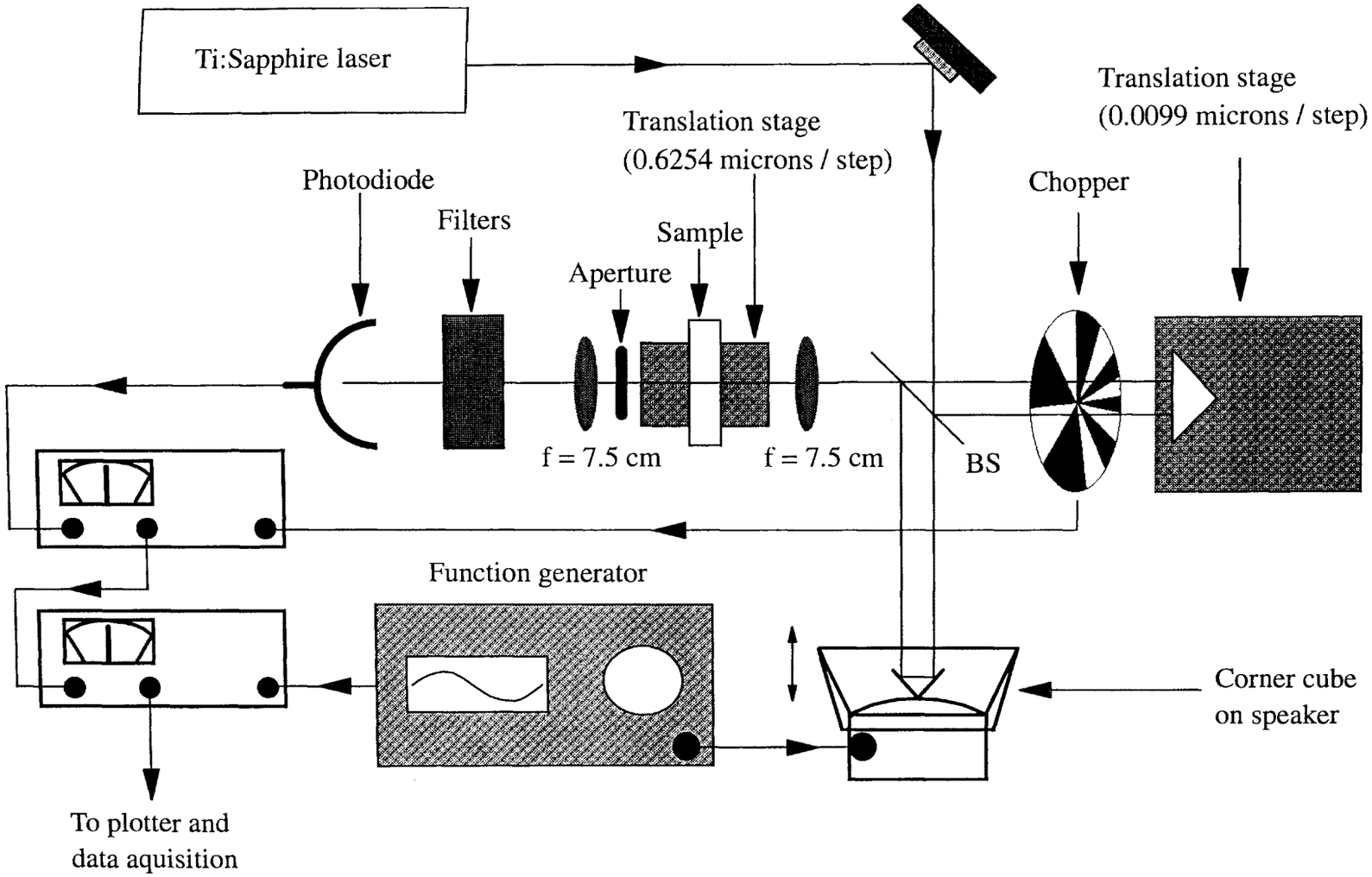

Figure 6.1 Experimental set up for the PDMT experiment,.

detector. Finally, the detected signal sequentially passes through two lock-in amplifiers, then the output of the second lock-in amplifier is piped into the data collection system. A scan consists of moving the prism so that the delay between pulses changes by more than the distance of their entire overlap. Including a safety margin this turned out to be about 200 micrometers. The combination of the amplitude modulation along with the PDM with a pulse delay much less than the pulse width is what we call the Pulse Delay Modulation Technique(PDMT).

6.2 Lock in Amplifier

The purpose of this section is to describe how the lock-in amplifier performs its most basic operations. By explaining the lock-in amplifier, the reason for modulating signals and using lock-in amplifiers in experimental set-ups should be become transparent. Additionally, this section will go over some of the specifics of the lock-in amplifiers that we used. However, the effects on our data analysis of implementing lock-in amplifiers as compared to more direct measurement methods and the details of how the lock-in amplifiers were implemented in each individual experiment will be discussed along with the experiments in question.

The Stanford Research Systems Model SR510 and SR530 lock-in. were amplifiers used in these experiments. The only real difference is that the SRS530 can give both the in phase and quadrature components of the signal at once. We did not use the quadrature component, so in effect both lock-ins were equivalent as far as we were concerned. However, there are examples where the quadrature component could be useful [6]. In general, the information presented here pertaining to the lock-in amplifiers is predominately based upon the material obtained from the SRS510 manual. Furthermore, **Figure** (6.2) shows a block diagram of the Model SRS510 system as depicted therein.

In general lock-in amplifiers are used to measure very small ac signals. These signals can be measured accurately even when in the presence of other signals or noise that may be orders of magnitude larger than the desired signal. Lock-in amplifiers achieve this by placing an arbitrarily narrow bandwidth filter centered at the frequency of the signal of interest. Therefore, the entire signal can pass through the filter, whereas only a tiny fraction of the power from broad band noise sources can pass through the system. Hence, as is shown in **Figure** (6.3), the Signal-to-Noise-Ratio (SNR) has been greatly increased. Obviously, a lock-in amplifier can best detect this ac signal when it occurs in a relatively low noise area of the spectrum. However, the detectability of dc signals and ac signals in a high noise area of the spectrum can be significantly enhanced when a lock-in amplifier is excited by a fixed frequency in a relatively quiet part of the spectrum. The lock-in amplifier then amplifies the signal and detects it in a very narrow bandwidth at that different and usually higher excitation frequency. The amplification and narrow bandpass filtering is performed with an active filter that can achieve a Q in the millions, which is well beyond the capabilities of passive electronic filters.

The manner in which the lock-in amplifier obtains the increase in signal to noise ratio is actually quite simple. Both the input signal and a reference signal with the same frequency as the input signal must be provided to the lock-in amplifier. There are a series of three filters that the input signal can then be passed through depending on the users preference. These include two different line filters that block the line frequency and its second harmonic, as well as an auto-tracking bandpass filter. Then this signal is amplified with a high gain ac amplifier. The amount of amplification depends on the units sensitivity setting. Meanwhile. the frequency of the reference signal is followed

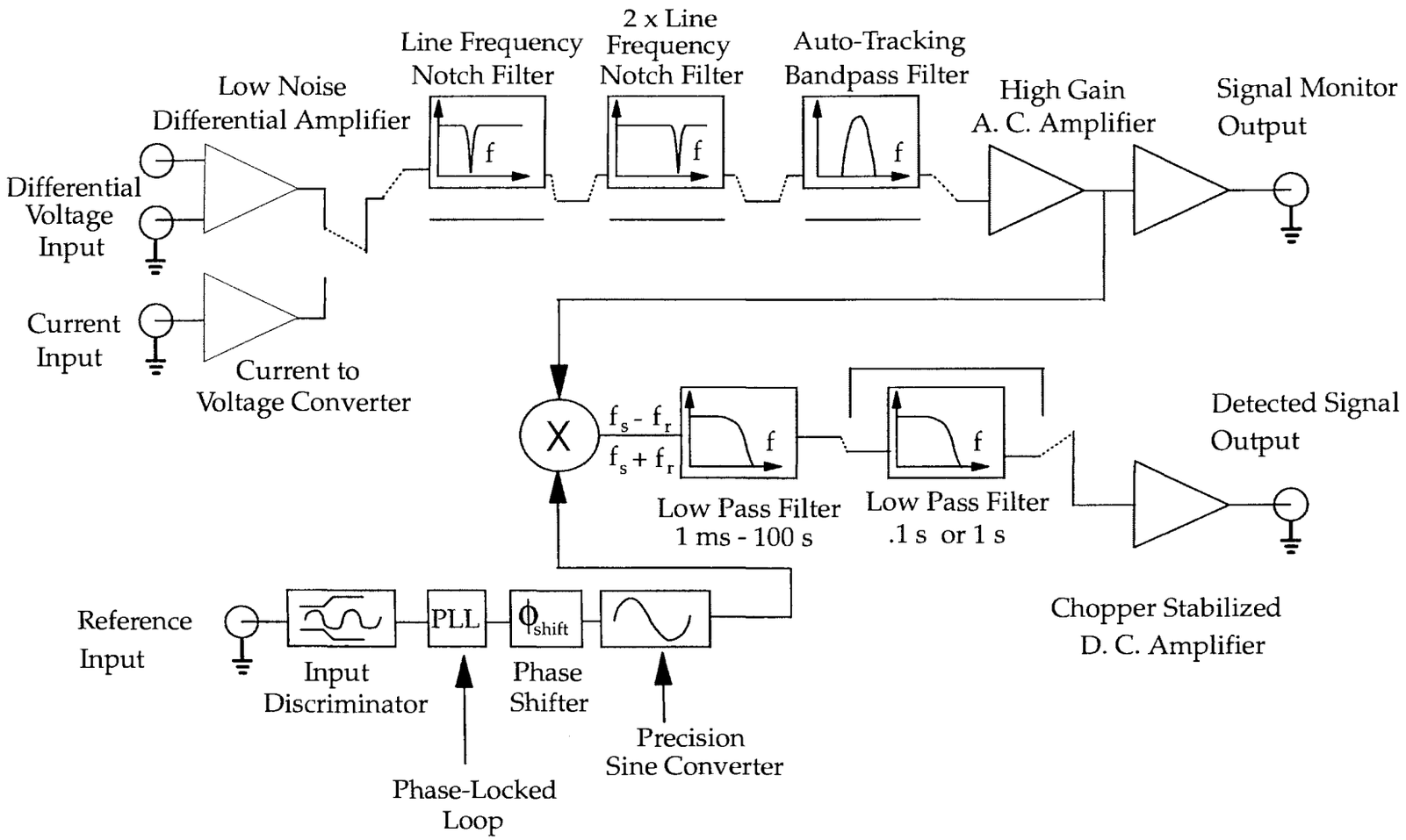

Figure 6.2 Block diagram for model SR510 lock-in amplifier

with a Phase Locked Loop(PLL). The phase of the PLL output may be shifted by the user, and by the time the reference signal reaches the Phase Sensitive Detector(PSD), it equals

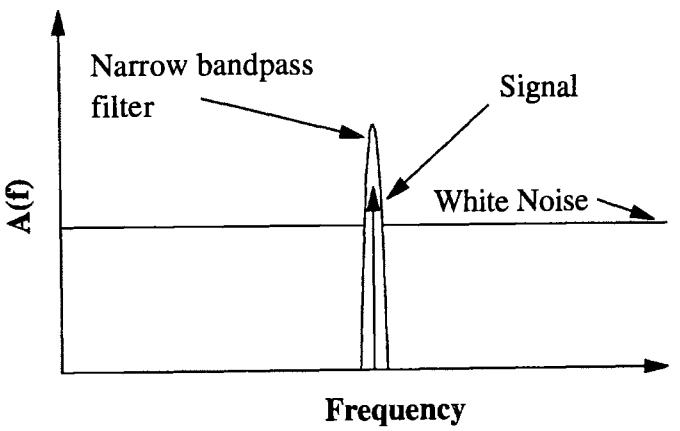

Figure 6.3 Narrow band filter that aids in detecting a relatively small signal in the presence of a large background noise.

$$V_r = \cos(\omega_r t + \phi). \tag{6.1}$$

This signal is then multiplied with the input signal in the PSD so that

$$V_{PSD} = V_{PLL} \cdot V_i, \tag{6.2}$$

where the input signal V_i is related to the information carrying signal Vs, by the following relation

$$V_i = V_s \cdot \sum_n [a_n \cos(n\omega_r t + \theta) + b_n \sin(n\omega_r t + \theta)]. \tag{6.3}$$

the summation represents the fact that the signal is not actually being modulated by a true sinusoid, rather some other function with its fundamental frequency equal to that of the sinusoid. The output of the PSD can be written as

$$V_{PSD} = V_s \cdot \sum_n [a_n \cos(n\omega_r t + \theta) + b_n \sin(n\omega_r t + \theta)] \cos(\omega_r t + \phi). \qquad (6.4)$$

Now, the PLL of a lock-in amplifier performs a different function than the PLL in a typical radio receiver. The PLL in a typical radio receiver is given the modulation frequency by the user, and it maintains a zero phase difference between the signal and reference waves. On the other hand, the function of the PLL in a lock-in amplifier is to determine the frequency of the reference modulation, and the user must ensure that the reference and signal waves are in phase. This can be done by adjusting the phase ϕ of the lock-in amplifier until the output signal is minimized, and then flipping the phase by 90 degrees. When the phase of the lock-in amplifier is set correctly, its output is maximized and ϕ is exactly equal to θ. Therefore, under these conditions the voltage of the PSD can be written as

$$V_{PSD} = \frac{1}{2} V_s \cdot \sum_n \{a_n [\cos[(\omega_r + n\omega_r)t] + \cos[(\omega_r - n\omega_r)t]] + b_n [\sin[(\omega_r + n\omega_r)t] + \sin[(\omega_r - n\omega_r)t]]. \qquad (6.5)$$

It should be noted that the introduction of the auto-tracking bandpass filter does increase the harmonic rejection. However, the maximum frequency component of the signal voltage Vs, is usually much less than the modulation frequency. Hence, when the active pre and post filter time constants are set by the user about the signals bandwidth, all the high frequency components and higher order harmonics of any significance are filtered out. Therefore, we end up with only the n=1 terms. So that the output appears as

$$V_{Out} = \frac{1}{2} V_s \cdot a_1. \qquad (6.6)$$

However, in this case there is only one beam, so the constants do not really make a difference. The important fact is that the output voltage is linearly related to the input signal. However, we will consider more complicated scenarios in a later chapter were we will have to consider the constant factors [1], [9].

6.3 System Noise and Modulation Frequency

The signal modulation can be pictured as shifting the signal to a new frequency range. Therefore, this modulation not only allows the lock-in amplifier to isolate and amplify the signal, but it determines what band of noise will be detected or rejected. Consequently, we ideally want the modulation frequency to be in a low noise part of the spectrum, so that as little of the noise or random fluctuations as possible will be let through by the pre and post filters. Of course there are physical constraints that limit our control of this modulation frequency, however a knowledge of the noises present is required to find the optimal modulation frequency.

The first source of noise that we are considering are the noises caused by random fluctuations in the electrical signal present in the detection process. There is not just one individual cause for this noise, rather there are several different noises that add in quadrature. We used a silicon photodiode that was biased with a negative 9.22 volts as our detector. The most significant noises present in the detection of a light source with this type of photodetector are 1/f noise, shot noise, and Johnson noise.

Johnson noise is the random voltage across a resistor at finite temperature, due to the thermal energy of the charge carriers in the resistor. Johnson noise is not actually inherent to the detection process, rather it is created when the photodiode created current passes through the load resistor. The RMS noise voltage due to Johnson noise is given by

$$\overline{V}^2_{\text{Johnson}} = 4kTR\Delta f. \qquad (6.7)$$

where T is the temperature in degrees Kelvin, R is the resistance, Δf is the bandwidth, and k is Boltzmann's constant which equals 1.38×10^{-23} J/K. Since, Johnson noise is frequency independent, we cannot eliminate it no matter what modulation frequency we choose. However, the lock-in amplifiers reduce the bandwidth, hence the total amount of Johnson noise, as well as 1/f noise and shot noise on the background is reduced. The

magnitude of Johnson noise is virtually insignificant compared to the size of the signal, and only dominates other forms of noise at extremely high frequencies.

The mechanisms behind 1/f noise are not well understood, however the contribution of 1/f noise to the current noise is

$$\bar{i}^2_{1/f}(f) = \frac{Ki^{\alpha}}{f^{\beta}}. \qquad (6.8)$$

Where K is a proportionality factor, $\alpha = 1$, and $\beta = 2$. By modulating at frequencies greater than 1 KHz, it is possible to reduce this low frequency noise.

Shot noise occurs because of the discrete nature of the charge carriers. When operating in linear regimes, either a photon liberates an electron or it doesn't. The RMS. noise current due to shot noise can be given as

$$\bar{i}^2_{shot} = 2ei_{avg}\Delta f, \qquad (6.9)$$

where e is the electron charge (1.6×10^{-19} Coulombs), i_{avg} is the mean current flowing due to signal and background, and Δf is the bandwidth of the measurement. Shot noise is white (flat with respect to frequency) for all the modulation frequencies that either we or the other groups used, therefore the magnitude of shot noise is expected to be larger than that of Johnson noise.

A generic plot of the relative magnitudes of these noises versus frequency is shown for a photodetector operated in the photoconductive mode in shown **Figure** (6.4). Therefore, we see that 1/f noise can be "eliminated" at a modulation frequency in the KHz region, while shot and Johnson noise are reduced by the limited bandwidth of the lock-in amplifier. However, laser noises are not shown in **Figure** (6.4), and I suspect that they dominate in the KHz regime. We aligned the beams collinearly in all of our experiments, so there was no thermal two beam coupling effects, and most other thermal nonlinearities would manifest themselves as an added signal instead of a noise. Still, in

the case of the experiments where any PDM was involved, only the irradiance dependent electronic nonlinearities would be detected.

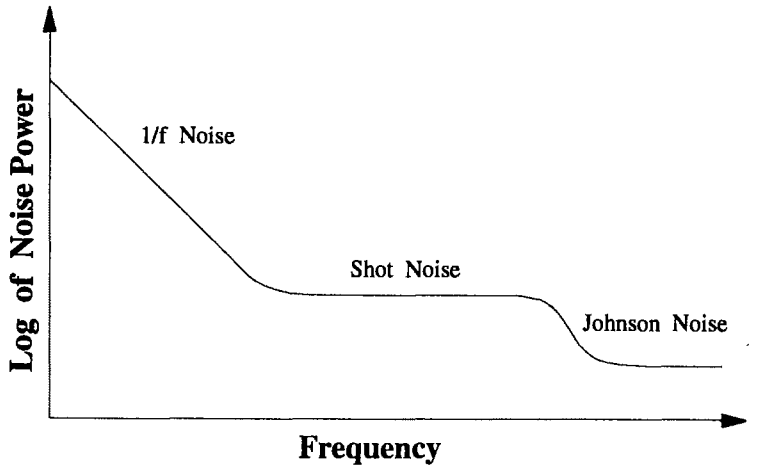

Figure 6.4 Typical photodiode detector current-noise power spectrum.

When Miller implemented the PDMT, he amplitude modulated the laser beam at around 9.7 MHz with an electrooptic modulator. This frequency was chosen, because the noise and fluctuations of his dye laser system were primarily caused by the modelocked argon pump laser. The noise of his pump laser dropped off quickly at frequencies greater than 1 MHz [1], [10]. Similarly, we believe that the system noise of our Ti:sapphire was also directly related to that of our cw argon pump laser. Although, we never checked our system noise with a spectrum analyzer, other individuals have done so with similar systems. **Figure** (6.5) shows the noise spectrum of a Ti:sapphire both with and without the output coupler being translated with a speaker [11]. The Ti:sapphire that this spectrum plot was from had a much slower and smoother oscillation of the output coupler

than ours did. Hence, our system noise was larger when the shaker was on. However, except for the effects caused by the fact that our pump laser is probably noisier than theirs, the characteristics of the noise spectrum are probably similar. Additionally, the noise power continuous to drop as the frequency increases [8]. Furthermore, this plot agrees at least qualitatively to the noise power output signal that we obtained from the lock-in amplifier on the noise setting, as the chopper's frequency was varied. However, no accurate results were obtained by that method, but it appeared that the noise was lower for the higher frequencies, as theory and the results of others suggested. That output was only checked because the frequency of the chopper became unstable near 3 KHz, and that caused the PLL of the lock-in amplifier to temporarily lose track of the modulation. Hence, the output signal of the lock-in amplifier would react with a quick dip in amplitude no matter what the time constants of the filters were set at. But, it was found that the signal to noise ratio would not suffer significantly as long as the chopper's frequency was in the 2 to 3 KHz range. Therefore, the modulation frequency of $2.54 \pm .01$ KHz was chosen, because it was around the maximum frequency where there was no chopper instability.

In addition to the noise and fluctuations mentioned above, there was also a significant amount of laser dropouts and laser drift, so much so that the entire next section will be dedicated to the slow deterioration of laser output that is referred to here as laser drift. Laser dropouts on the other hand were quite curable by ensuring that both the argon and Ti:sapphire were properly aligned. But, when a laser dropout did occur it was usually because the laser was drifting. A laser dropout looks like the complete disappearance of several pulses when looking at the modelocked train on the oscilloscope. This occurrence appears random, and although temporary, this huge change in irradiance causes a great change in the detected nonlinear signal. In fact, the change is

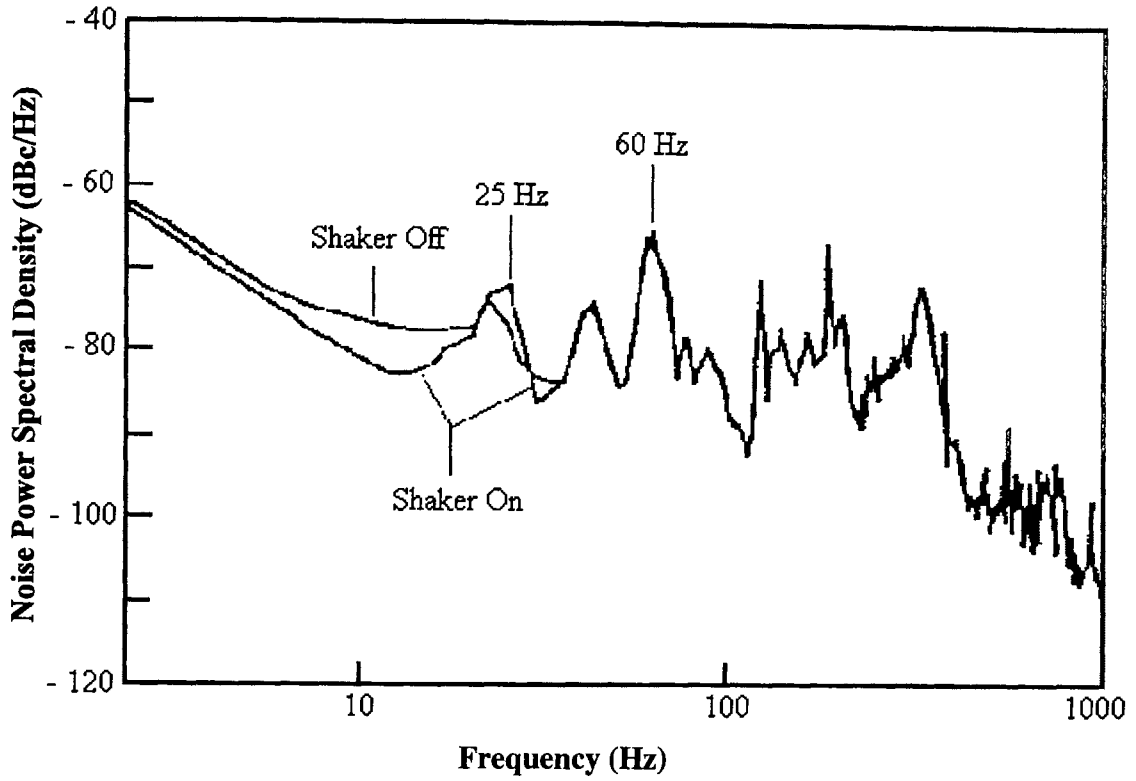

Figure 6.5 Comparison of the low-frequency amplitude fluctuations of a self mode locked Ti:sapphire laser with the shaker both on and off [11].

so huge that at best there is a huge dip in the signal, and usually the lock-in amplifier completely loses its lock on the modulation. Furthermore, just as with the chopper wheel instabilities, changing the time constants of the filters could not remedy this problem in its extreme case. Fortunately, we were able to minimize this problem through better alignment. Yet, looking at the theoretical noise spectrum and measured noise signal only further confirm the hypothesis that most of our noise and fluctuation problems were not from detector noise or thermal instabilities, but rather stemmed from laser dropouts and laser drift [12], [13].

6.4 Laser Drift

The modulation and lock-in techniques reduced the effects of detection noise, thermal instabilities and laser fluctuations, but had no effect upon long term laser drift which is directly related to the stability of the Argon pump laser. Additionally, there was no simple way to use energy or pulse width windows, nor divide the output signal by the laser output. So, the medium to long term laser fluctuations turned out to be quite detrimental. On some days the experiments output signal would change by as much as thirty percent from the beginning to the end of the experiment. However, there were a few days where the Argon performed well and the change was within 5-10 percent for hours.

The Argon ion laser was set on the constant power mode, so that we could keep the output power at the desired 8 watts. The constant power is achieved by using a photodiode with feedback to the power supply. Consequently, as the laser's output power varies, the power supply could compensate almost instantaneously by altering the magnitude of the current across the tube. Hence, the small power fluctuations that existed were not the main problem ,rather the detuning due to thermal and mechanical instabilities of the laser was the main culprit. As the laser detuned the power was on average compensated for, however the pointing of the pump laser into the Ti:sapphire was altered. Therefore there was a gradual misalignment of the Ti:sapphire, which gradually changed the output of the Ti:sapphire. However, this output change was small compared to the change in signal that we observed. Now, we thought that this was in part due to a change in pulse width, which may have been a factor. It turned out that this change in the pointing caused the pointing of the Ti:sapphire to change significantly. In fact a pinhole inches from the output of the Ti:sapphire could detect this pointing error. Consequently, by the time the beam reached our set-up it had wandered significantly, and

this wreaked havoc upon the alignment of our experiment. Furthermore, the stability of the mode locking became poor after the argon drifted by a large amount, and eventually could not be sustained. There are several causes the lead to the drift, noise and distortion of the argon's output beam, but the largest problems were due to the drift that was probably caused by its thermal and/or mechanical instabilities.

6.5 Autocorrelation with Lock-in

There are several reasons why it is useful to perform an autocorrelation measurement with the lock-in amplifier and chopper, even when we could almost as easily perform the more sensitive PDMT. There is of course the obvious reason, that is we want an autocorrelation for pulse width measurement, and it is easiest to perform the autocorrelation without changing the experimental set up. With this set up we are able to obtain a slight variation of the second order intensity autocorrelation function $G_2(\tau)$. The only difference between this autocorrelation and a second order intensity autocorrelation is that one of the background terms is not "seen" or locked into with the lock-in amplifier. Therefore, two identical and collinearly aligned Gaussian beams should theoretically have a peak to background ratio of five to one with the lock-in amplifier, as opposed to six to two(or three to one) ratio that is normally obtained. However, misalignment or unequal beam intensities alters this ratio, just as the effective intensity that we calculate in Chapter 7 for the effective two beam nonlinearity is altered by these conditions. As stated before, a greater signal to noise ratio is obtained when performing the autocorrelation with the lock-in amplifier, because it makes up for the lack of pulse width and energy windows on the accepted data pulses. Furthermore, the amplitude modulated autocorrelation is in fact the PDMT without the added PDM or second lock-in amplifier. Consequently, the autocorrelation is easier to align than the full PDMT, because the second arm of the

Michelson interferometer does not need to be critically aligned. However, because the modulated autocorrelation is one step away from a PDMT it may be useful for calibrating the values obtained from a PDMT measurement. In any event, we know that the peak intensity achieved at the zero delay for an autocorrelation is the same as that obtained when Z is equal to zero in a Two Beam Z-Scan. Therefore, with knowledge of the relationship between the autocorrelation and the PDMT measurement, we should be able to check any calibration. Finally, some materials generate a signal that is much larger than any noise, and the signal from the irradiance dependent nonlinearity overwhelms any from the thermal effects. Consequently, the full PDMT measurement may not be needed and the autocorrelation or even a simpler direct measurement technique may be sufficient to obtain the pertinent material characteristics.

6.6 Pulse Delay Modulation Technique

Several groups, [2] - [7], have performed mathematical analyses of the various modulation techniques, and Miller et al. [1], have given the theoretical treatment for the PDMT in particular. Since, we have no new information relating to the theory, the first part of this section will simply point out some of the salient results pertaining to PDM that were determined by others previously. Similarly, there has already been an overview of the PDMT, as well as a comparison of our set up to that of previous individuals earlier in this chapter. Additionally, the specifics of our experiments will be given along with the results, therefore these topics will not be repeated again in this section. Instead, the second part of this section will describe a new variation of the PDMT that can be used to gain information about nonlinear refractive effects through the use of an aperture.

6.6.1 Open Aperture PDMT

The setup used for the Open Aperture PDMT or simply the PDMT has already been discussed, as well as the benefits of high frequency amplitude modulation. Therefore, here we will discuss the manner in which the PDM can eliminate the effects of thermal nonlinearities. As stated earlier the output of the first lock-in amplifier when performing an autocorrelation with either a phase matched second harmonic crystal or from a 2PA crystal is proportional to the intensity autocorrelation function. Hence, the output of the first lock-in amplifier when there is the addition of PDM through the modulation of the speaker is approximately

$$S_{L1}(\tau) \propto G_2(\tau). \tag{6.10}$$

However, in the case where there is PDM present τ is not a constant, rather τ depends upon the magnitude and frequency of the speaker's oscillation, so that

$$\tau = \tau_o + \Delta\tau\cos(\omega_s t), \tag{6.11}$$

where ω_s is the frequency of the speaker's oscillation, τ_o is the mean time delay between the two beams as is determined by the position of the stage, and $\Delta\tau = \delta/c$ with δ being the magnitude of the speaker's oscillation. Now, when the modulation depth $\Delta\tau$ is small compared to the temporal structure of the pulse, $S(\tau)$ can be expanded in a Taylor series about the fixed delay τ_o as

$$S(\tau) = S\left[\tau_o + \Delta\tau\cos(\omega_s t)\right] \approx \sum \frac{d^m}{d\tau_o^m}\left[S(\tau_o)\right](\Delta\tau/2)^m \cos(m\omega_s t). \tag{6.12}$$

Hence, by locking the frequency of the lock-in amplifier to $m\omega_s$, we obtain an output that is proportional to the mth derivative of $S(\tau)$. Such that

$$S_{Out}(\tau) \approx \frac{1}{2}\frac{d^m}{d\tau^m}\left[S(\tau_o)\right]\frac{(\Delta\tau/2)^m}{m}, \tag{6.13}$$

where we can obtain the first derivative (m=1), and the second derivative (m=2), by setting the frequency setting of the lock-in amplifier to f and 2f respectively.

6.6.2 Closed Aperture PDMT

In addition to the standard PDMT without an aperture it is possible to obtain greater information by performing the measurement with an aperture as in the Z-Scan, which will be described in Chapter 7. For instance, when there is no Two Photon Absorption(2PA) present, the PDMT would normally deliver no signal. Even when the material has nonlinear refraction, the presence of an aperture would still not allow us to obtain any signal with the material at the beams focus. However, by placing the material at positions in Z where a Z-Scan signal would normally be obtained will result in a Closed Aperture PDMT signal. Therefore, for irradiance dependent electronic nonlinearities the optimal positions for a maximum signal would be at $\pm 0.85\ Z_o$, and for free carrier refraction this would occur at $\pm 0.6\ Z_o$. Where Z_o is the Raleigh range of the focused Gaussian beam.

Similarly, the Closed Aperture PDMT should be of use in determining nonlinear refractive effects even in the presence of 2PA. This would be done by performing both the Open Aperture PDMT (standard version), and the Closed Aperture PDMT measurements with the material at focus and the two Z positions of maximum refractive signal . Then the open and closed aperture measurements would be compared at the three positions to determine the presence, and with proper calibration, the magnitude of the nonlinear refractive effects [14], [15].

6.7 Fitting Procedure

As stated above, the magnitude of the PDMT signal is not only proportional to the strength of the materials nonlinearity, but it gives us a scan with a shape which is proportional to the derivative of the autocorrelation of the incident pulse. This fact can be

useful in the analysis of the data and calibration of the system, as well as determining the lasers pulse width. Therefore, so as to ensure that we were in fact getting an accurate PDMT scan, we needed to fit the PDMT data to the derivative of the autocorrelation and compare the fit values to those of the actual autocorrelation. This was important to us, because we were able to experimentally determine if the magnitude of our speaker oscillation was small enough so as not to distort the derivative effect. In addition to describing the fitting procedure, a simple numerical relation between the peaks of PDMT scan (PDM_{Sep})and the FWHM of the incident pulse width will be given.

A good experimentally determined electric field profile of a KLM modelocked Ti:sapphire laser pulse is

$$E(t) = \mathrm{sech}\left(\frac{1.76t}{\Delta t}\right), \tag{6.14}$$

where Δt is the FWHM of the pulse. The shape of the autocorrelation function is proportional to $G_2(\tau)$ for the both second harmonic and the two photon absorption. However, when the lock-in amplifier is used, the term from the unmodulated beam in the intensity autocorrelation is not detected by the lock-in amplifier, and this will result in a theoretical five to one instead of a three to one peak to background ratio.

The starting function for $G_2(t)$ was obtained from a paper by Diels et al. [16], where the normalized intensity autocorrelation function $G_2(\tau)$ for a pulse with $\mathrm{sech}^2(t)$ intensity profile is

$$G_2(\tau) = \frac{\int_{-\infty}^{\infty} |E^2(t)E^2(t-\tau)|d\tau}{\int_{-\infty}^{\infty} |E^2(t)|^2 d\tau} = \frac{3[\tau\cosh(\tau) - \sinh(\tau)]}{\sinh^3(\tau)}. \tag{6.15}$$

By performing consecutive differentiations with respect to τ, we can obtain the first derivative of the intensity autocorrelation function

$$\frac{\partial G_2(\tau)}{\partial \tau} = \frac{3\tau}{\sinh^2(\tau)} - 9\frac{[\tau\cosh(\tau) - \sinh(\tau)]}{\sinh^4(\tau)}\cosh(\tau), \tag{6.16}$$

and the second derivative of the intensity autocorrelation function

$$\frac{\partial G_2(\tau)}{\partial \tau} = 12\frac{\{\tau\cosh^3(\tau) - 2\cosh^2(\tau)\sinh(\tau) - \sinh(\tau) + 2\tau\cosh(\tau)\}}{\{\sinh(\tau)[\cosh^4(\tau) - 2\cosh(\tau) + 1]\}}. \tag{6.17}$$

In order to fit the data, we generalized the beam fitting procedure that our group had already been using when fitting the standard autocorrelation for a temporally Gaussian beam. This was achieved by fitting the data to the values of a_n, b_n, c, and d that minimized the squared error in the fitting equation of

$$F^{(0)}(\tau) = a_0 + b_0 \times G_2(\frac{\tau - c}{d}) \tag{6.18}$$

for the autocorrelation, and

$$F^{(n)}(\tau) = a_n + b_n \times \frac{\partial}{\partial \tau}F^{(n-1)}(\tau) \tag{6.19}$$

$$= a_n + B_n \times \frac{\partial^n}{\partial \tau^n}G_2(\frac{\tau - c}{d})$$

for its derivative of order n. It is crucial that the differentiation with respect to τ be performed upon the scaled autocorrelation function as shown, rather than plugging in the scaling factors after the differentiation of $G_2(\tau)$. The scaling factor c is a relative path or time difference that is determined by the stage position, and d is the $1/e^2$ half width of the autocorrelation function. Additionally, B_n represents a constant amplitude scaling factor for the nth derivative of the autocorrelation. Such that

$$B_n = \prod_{i=0}^{n} b_i, \qquad (6.20)$$

where the b_n terms are scaling factors that relate the relative magnitudes of two consecutive derivatives. Furthermore, the a_n terms (n>0) should ideally be zero, because they just take care of background noise and error. However, in the case of the autocorrelation fitting function $F^{(0)}(\tau)$, a_o also contains one beam's signal from the background part of the autocorrelation. Hence, the a_o term can be useful when calibrating the measurements, but we were unable to develop an absolute calibration for the PDMT that was very accurate. Therefore, the most important fitting parameter for us at this time is d, because the $1/e^2$ half width of the autocorrelation function is related to the pulse width by the Δt. Here Δt is 1.763 and 1.665 for $sech^2$ and Gaussian shaped pulses respectively, as was given earlier in **Table** (5.1).

Although, some of the data was fit to the Gaussian fitting functions as a first order approximation, it turned out that the mean squared error was less for the $sech^2$ fitting functions as should be expected. Although, we fit all the autocorrelations and their derivatives in this thesis with the appropriate $sech^2$ fitting functions, we did use the Gaussian as well as the $sech^2$ fitting functions for the plots that are shown later in the chapter. Therefore, without showing the differentiation, the fitting functions of the autocorrelation and its derivatives for both hyperbolic secant squared and Gaussian shaped pulses are shown below.

The function that we fit the autocorrelation to for a pulse with a temporal intensity profile proportional to $sech^2(t)$ is

$$F_{Sech}^{(0)}(\tau) = a_0 + 3b_0 \frac{\left[\left(\frac{\tau - c}{d}\right)\cosh\left(\frac{\tau - c}{d}\right) - \sinh\left(\frac{\tau - c}{d}\right)\right]}{\sinh^3\left(\frac{\tau - c}{d}\right)}. \qquad (6.21)$$

Similarly the fitting function for the first derivative of the autocorrelation is

$$F_{Sech}^{(1)} = a_1 + 3B_1\left[\frac{(\tau-c)}{d^2\sinh^2(\frac{\tau-c}{d})} - 3\cosh(\frac{\tau-c}{d})\frac{(\frac{\tau-c}{d})\cosh(\frac{\tau-c}{d}) - \sinh(\frac{\tau-c}{d})}{d\times\sinh^4(\frac{\tau-c}{d})}\right], \quad (6.22)$$

and for the second derivative we obtain

$$F_{Sech}^{(2)}(\tau) = a_2 + 3B_2\left[\frac{1}{[d^2\sinh^2(\frac{\tau-c}{d})]} + 12\frac{(\frac{\tau-c}{d})\cosh(\frac{\tau-c}{d}) - \sinh(\frac{\tau-c}{d})}{d^2\sinh^5(\frac{\tau-c}{d})}\cosh^2(\frac{\tau-c}{d})\right.$$

$$\left. -5\cosh(\frac{\tau-c}{d})\frac{(\tau-c)}{[d^3\sinh^4(\frac{\tau-c}{d})]} - 3\frac{(\frac{\tau-c}{d})\cosh(\frac{\tau-c}{d}) - \sinh(\frac{\tau-c}{d})}{d^2\sinh^3(\frac{\tau-c}{d})}\right]. \quad (6.23)$$

Now, the equivalent fitting functions for a pulse with a Gaussian temporal intensity profile are

$$F_{Gauss}^{(o)}(\tau) = a_0 + b_0\times\exp\left[-\frac{1}{2}\left(\frac{\tau-c_0}{d_0}\right)^2\right], \quad (6.24)$$

$$F_{Gauss}^{(1)}(\tau) = a_1 + B_1\frac{-(\tau-c_0)}{d_0^2}\exp\left[-\frac{1}{2}\left(\frac{\tau-c_0}{d_0}\right)^2\right], \quad (6.25)$$

and

$$F_{Gauss}^{(2)}(\tau) = a_2 + B_2\left\{\frac{(\tau-c_0)^2}{d_0^4}\exp[-\frac{1}{2}\left(\frac{\tau-c_0}{d_0}\right)^2] - \frac{1}{d_0^2}\exp[-\frac{1}{2}\left(\frac{\tau-c_0}{d_0}\right)^2]\right\}. \quad (6.26)$$

A plot of the autocorrelation function and its derivatives is shown in **Figure** (6.6) for a hyperbolic secant squared pulse. Similarly, **Figure** (6.7) shows how the relative magnitudes of these functions are altered, when the pulse width is decreased by 50%. Of

course, we expect the width of the functions to change when the pulse width is altered. However, it is important to note that the magnitude of the derivatives, and the relative magnitude between the autocorrelation and its derivatives is decreased as the pulse width is increased. This occurs only when the irradiance and absolute speaker modulation depth remain constant. Furthermore, the magnitude of the optical nonlinearities are proportional to the irradiance, and the irradiance is inversely proportional to the pulse width. Hence, the output of the PDMT scan is even more sensitive to relatively small changes in pulse width as compared to other measurement techniques. In fact, in general the derivatives of the autocorrelation function theoretically appear to be more sensitive to the pulse width and shape than the autocorrelation functions themselves. This is demonstrated by comparing the autocorrelation function in **Figure** (6.8), the PDMT in **Figure** (6.9), and the derivative of the PDMT in **Figure** (6.10) for one temporally Gaussian shaped pulse and different pulse width $sech^2$ pulses.

Furthermore, by looking at the equations for the derivatives of the Gaussian autocorrelation functions, we can determine that the change in magnitude of the first derivative is proportional to 1/d, and that of the second derivative is proportional to $1/d^2$ with respect to the magnitude of the autocorrelation function. However, the actual PDMT scan includes a term that is proportional to $(\Delta\tau)^m$, and this would negate this scaling ratio if $\Delta\tau$ is kept at a constant percentage of the total pulse width. However, we do not keep the ratio constant, and it would be impossible alter $\Delta\tau$ once an experiment has started. The extra factors of one half and the ratio between the pulse width and

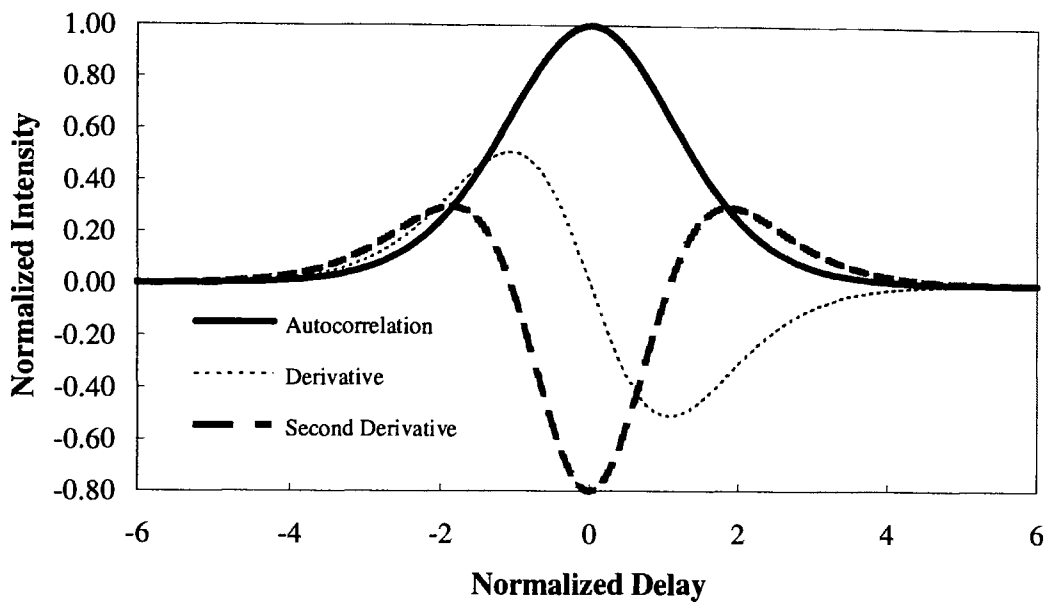

Figure 6.6 Autocorrelation function and its derivatives for a $sech^2$ pulse.

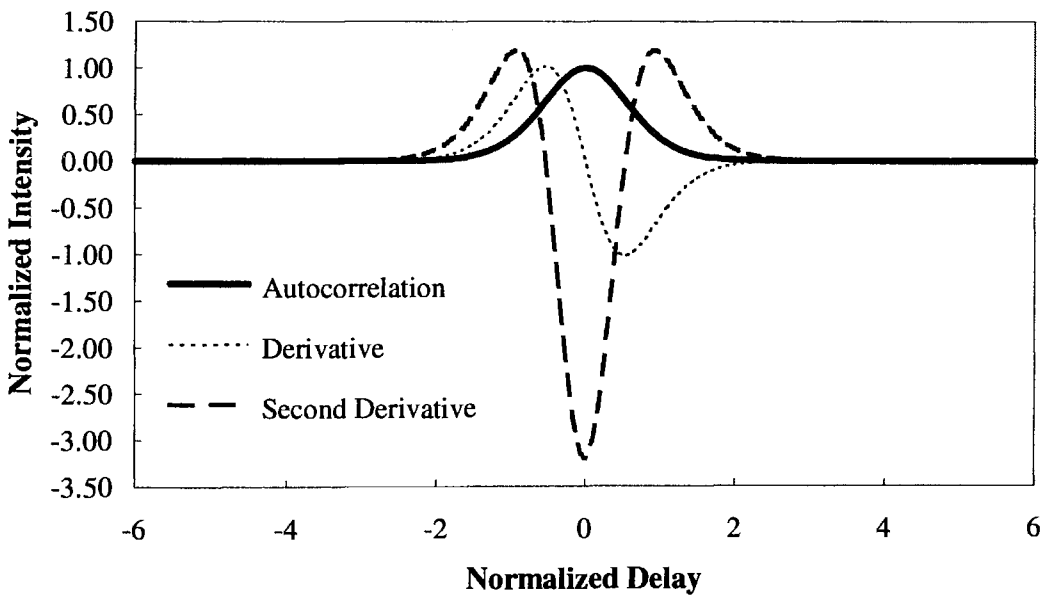

Figure 6.7 Autocorrelation and its derivatives when the pulse width has been cut in half.

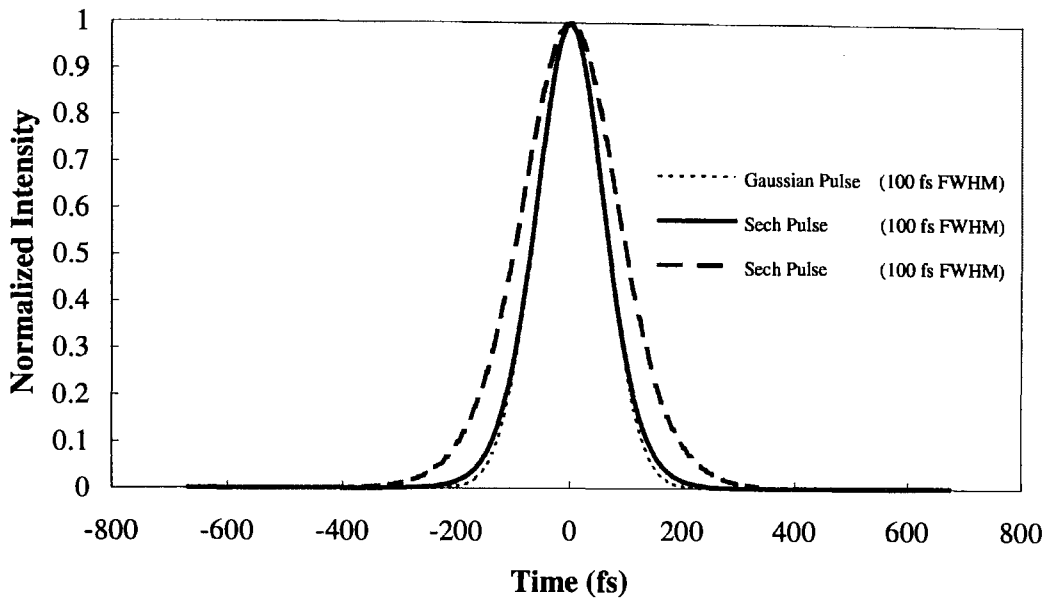

Figure 6.8 Comparison of Autocorrelation functions for different pulse shapes, and pulse widths, but with the same peak irradiance.

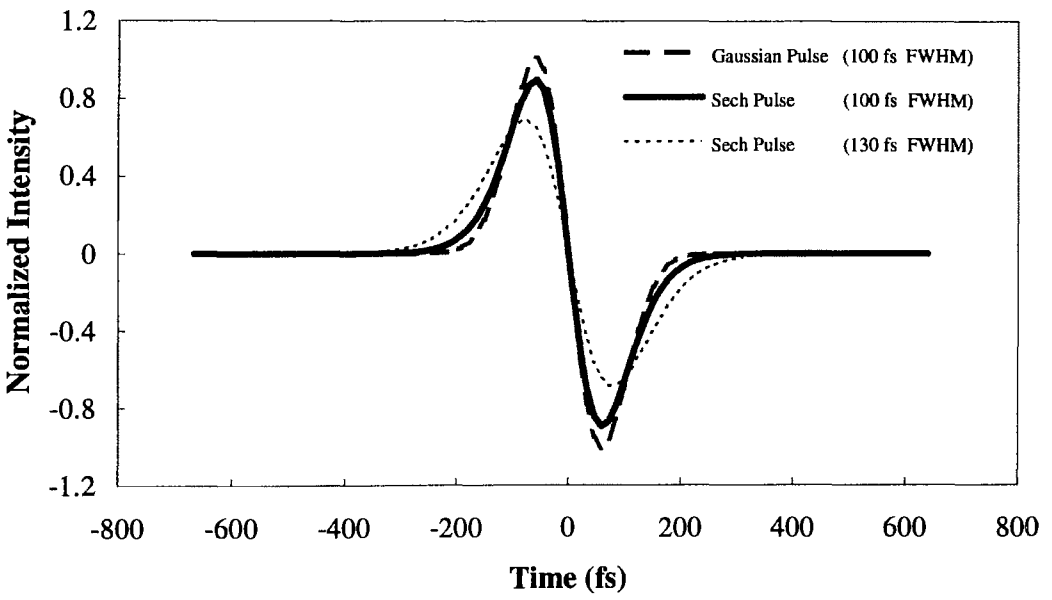

Figure 6.9 Theoretical comparison of PDMT scans with a constant intensity.

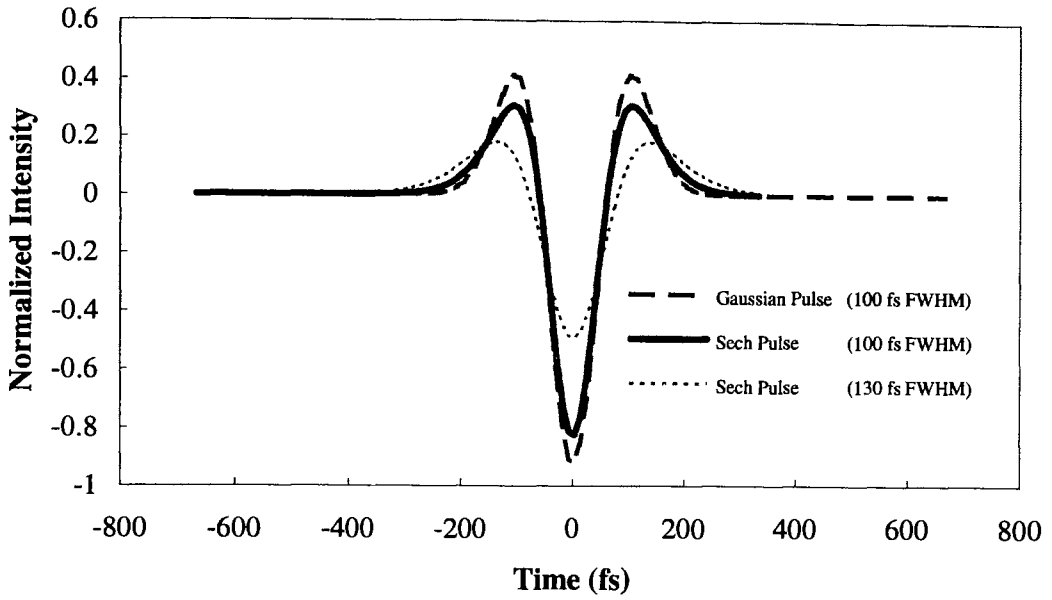

Figure 6.10 Comparison of theoretical PDMT derivatives with a constant intensity.

modulation depth actually ensure that the derivatives turnout to be smaller in magnitude than the autocorrelation itself. However, the conclusion is that the accuracy of the pulse width is extremely important because the shape and magnitude of the scan actually is altered even if the irradiance is kept constant.

We have already demonstrated why determining the correct pulse width is very important to the accurate analysis of the experimental results. Furthermore, in some cases it may be useful to obtain information from a PDMT without the use of a fitting routine. In fact there is a simple relation between the peak to peak separation of the PDMT scan and the FWHM of the incident pulse. We first derived this relation for a temporally Gaussian pulse, because For a temporally Gaussian beam, the pulse width of the incident laser light is readably available from the PDMT data. By setting the derivative of the PDMT which is the second derivative of the scaled intensity autocorrelation function,

$\frac{\partial^2 G_2(\tau/d)}{\partial \tau^2}$ equal to zero, we can find the location of the peaks of the PDMT scan relative to the pulse width of the scaled intensity autocorrelation. For a temporally Gaussian pulse the peaks of the PDMT scan occur exactly at the Half Width $1/e^2$ point of the scaled intensity autocorrelation function. Therefore, with respect to the notation used earlier, the FWHM of the pulse is

$$\mathrm{FWHM}_{\mathrm{Gauss}} = \Delta t \times \frac{\mathrm{PDM}_{\mathrm{Sep}}}{2}, \qquad (6.27)$$

where $\mathrm{PDM}_{\mathrm{Sep}}$ is the separation in time between the peak and valley of the PDMT data and Δt equals 1.665 for a temporally Gaussian pulse. Hence, the FWHM of the pulse can be quickly approximated from the PDMT scan with

$$\mathrm{FWHM}_{\mathrm{Gauss}} = 0.8325 \times \mathrm{PDM}_{\mathrm{Sep}}. \qquad (6.28)$$

Due to its similarity in shape with the temporally Gaussian shaped pulses, as we showed above, we expect that there should be a similar relation between the $\mathrm{PDM}_{\mathrm{Sep}}$ and the pulses FWHM for the hyperbolic secant shaped pulses. Numerically, we found out that the second derivative of the scaled intensity autocorrelation function was equal to zero at about $1.0718118 \times d$. Hence, the peaks of the PDM occur at ± 1.0718118, so the relationship between the pulses FWHM and $\mathrm{PDM}_{\mathrm{sep}}$ can be easily solved for by using the following relation

$$\mathrm{FWHM}_{\mathrm{Sech}} = \Delta t \times \frac{\mathrm{PDM}_{\mathrm{Sep}}}{2 \times 1.072}. \qquad (6.29)$$

Since, a pulse with a $\mathrm{sech}^2(t)$ intensity profile has a Δt equal to 1.763, the FWHM of the actual pulse is can be approximated by

$$\mathrm{FWHM}_{\mathrm{Sech}} = 0.8223 \times \mathrm{PDM}_{\mathrm{Sep}}. \qquad (6.30)$$

REFERENCES FOR CHAPTER 6

[1] S. A. Miller, "Ultrasensitive Technique for Measurement of Two-Photon Absorption", Phd. Diss., University of North Texas, Denton, TX, 1991.

[2] J. J. Snyder, R. K. Raj D. Bloch, and M. Ducloy, "High-sensitivity nonlinear spectroscopy using a frequency-offset pump," *Opt. Lett.* **8**, 163-165 (1980).

[3] W. Length, C. Ortiz, and G. C. Bjorklund, "Pulsed frequency-modulation spectroscopy as a means for fast absorption measurements," *Opt. Lett.* **6**, 351-353 (1981).

[4] F. M. Kamga, and M. G. Sceats, "Pulse-sequence coherent anti-Stokes Raman scattering spectroscopy: a method for suppression of the nonresonant background," *Opt. Lett.* **5**, 126-128 (1980).

[5] B. F. Levine, and C. G. Betha, "Frequency-modulated shot noise limited stimulated Raman gain spectroscopy," *Appl. Phys. Lett.* **36**, 245-247 (1980).

[6] G. C. Bjorklund, "Frequency-modulation spectroscopy: a new method for measuring weak absorptions and dispersions," *Opt. Lett.* **5**, 15-17 (1980).

[7] G. Camy, C. J. Borde, and M. Ducloy, "Heterodyne saturation spectroscopy through frequency modulation of the saturating beam," *Opt. Commun.* **41**, 325-330 (1982).

[8] N. Sarukura, and Y. Ishida, "Ultrashort Pulse Generation from a Passively Mode-Locked Ti:sapphire Based System," *IEEE J. of Quantum Electron.* **QE-26**, 2134-2141 (1992).

[9] Manual for Model SR510 Lock-in Amplifier, Stanford Research Systems.

[10] A. I. Fergusan, J. N. Eckstein, and T. W. Hansch, "A Subpicosecond Dye Laser Directly Pumped by a Mode-Locked Argon Laser," *J. Appl. Phys.* **49**, 5389-5391 (1978).

[11] Y. M. Liu, K. W. Sun, P. R. Prucnal, and S. A. Lyon, "Simple method to start and maintain self-mode-locking of a Ti:sapphire laser," *Opt. Lett.* **17**, 1219-1221 (1992).

[12] R. W. Boyd, Radiometry and the Detection of Optical Radiation, John Wiley & Sons, New York, 1983, p. 164.

[13] T. Limperis, and J. Mudar, "Detectors," in The Infrared Handbook 3rd printing, (W. L. Wolfe and G J. Zissis ed.) Infrared Information Analysis(IRIA) Center of the Environmental Research Institute of Michigan(ERIM), Ann Arbor, 1989

[14] M. Sheik-Bahae, *Personal Communication,* (1994).

[15] E. W. Van Stryland, *Personal Communication,* (1994).

[16] J.-C. Diels, J. J. Fontaine, I. C. McMichael, and F. Simoni, "Control and measurement of ultrashort pulse shapes (in amplitude and phase) with femtosecond accuracy," *Appl. Opt.* **24**, 1270-1282 (1985).

CHAPTER 7

Z-SCAN MEASUREMENT TECHNIQUES

The Z-scan has proven to be a simple yet accurate manner in which to measure the nonlinear optical properties of materials. The Z-Scan has been used to measure the refractive index change induced by two-photon excited free carriers (coefficient σ_r), the two-photon absorption coefficient β, and the bound electronic nonlinear refractive index n_2. We perform Z-scan measurements with a 780 nm high repetition rate Ti:sapphire laser with the addition of an amplitude modulation in one arm so that a lock-in amplifier can be implemented to increase the signal to noise ratio. A Two Beam Z-scan is also performed so that we can calibrate the output from a Pulse Delay Modulated Z-scan (PDM Z-scan) that cannot be calibrated directly. However, the PDM Z-scan differentiates between the irradiance dependent nonlinearities like two photon absorption (2PA) and bound electronic nonlinear refraction from long lived fluence dependent nonlinearities like thermal refraction. Additionally, it provides greater than an order of magnitude increase in the signal to noise ratio through the use of modulation techniques with the lock-in amplifier.

7.1 Overview

The Z-scan in its simplest form consists of a nonlinear material being translated(in Z) by a stage through the focus of an intense Gaussian laser beam. The transmittance of this beam through the sample is then measured with a detector in the far field. This may be done with an aperture in front of the detector (Closed Aperture Z-Scan) or without an

aperture in front of the detector (Open Aperture Z-Scan). The general set-up for a standard Z-Scan is shown in **Figure** (7.1). Although, the overall energy incident on the sample remains constant, the irradiance and fluence vary in a known deterministic manner as the sample moves through focus. Therefore, various forms of self-action can be observed and modeled.

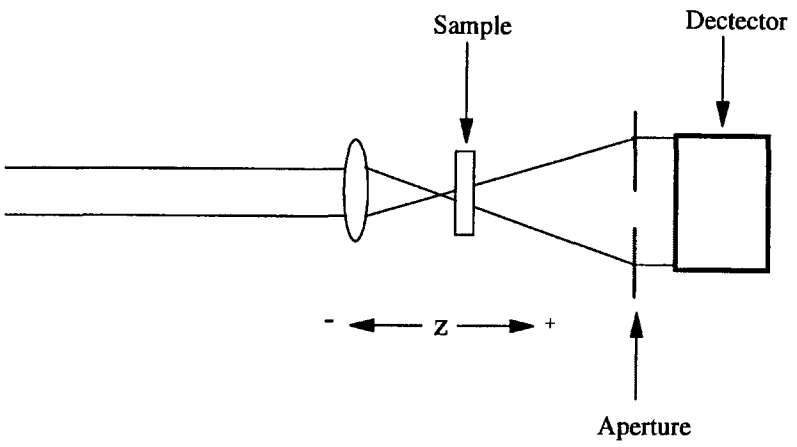

Figure 7.1 Single beam Z-Scan experimental set-up.

If there is no aperture in place multi-photon absorption, and saturation of absorption can be seen. Two photon absorption (2PA) appears as an inverted Lorentzian, with the minimum transmittance at Z=0, whereas saturation of absorption displays the maximum transmission at Z=0 where the maximum irradiance is present.

The presence of an aperture also allows self focusing or self defocusing, which are caused by changes in refractive index effects to be observed. If the sample has a thickness shorter than the diffraction length(thin medium), then it can be considered a thin lens with a variable focal length. If the Z-position of the sample is far away from the focus of the laser beam, then the irradiance is low and negligible nonlinear refraction

occurs. Now, as the sample moves towards the focus the irradiance increases, which leads to self lensing in the material. A negative self lensing prior to focus will collimate the beam, which results in a greater transmittance through the aperture. When the sample reaches focus there is no effect on the far field intensity pattern. This is similar to placing a thin lens at the focus, which would result in minimal alteration of the far field pattern. Then as the sample continues in the positive Z-direction towards the detector, the same self defocusing will lead to beam broadening in the far field. Hence, the detected transmittance will decrease. Then as the sample continues onwards, the irradiance will eventually decrease to a point where the nonlinear effects become negligible. Using a similar analogy, a positive nonlinear refractive index is found to cause a prefocal minimum and a postfocal maximum in transmittance, which is demonstrated in **Figure** (7.2).

The multi-photon absorption and saturation of absorption are still present when an aperture is used. However, the change in transmittance due to the nonlinear refraction is not present in the open aperture Z-scan. So, nonlinear absorption can be determined solely with the open aperture Z-scan, and nonlinear refraction in a nonabsorbing medium can be determined solely by the closed aperture Z-Scan. However, determining the nonlinear refraction in a medium with nonlinear absorption or absorption saturation requires both the open aperture and closed aperture Z-Scan.

There are two ways in which to find the nonlinear refraction in an absorbing medium with both of these scans. The first consists of determining the nonlinear absorption with the open aperture scan, then determining the nonlinear refraction with the closed aperture Z-Scan and the known nonlinear absorption. The second method consists

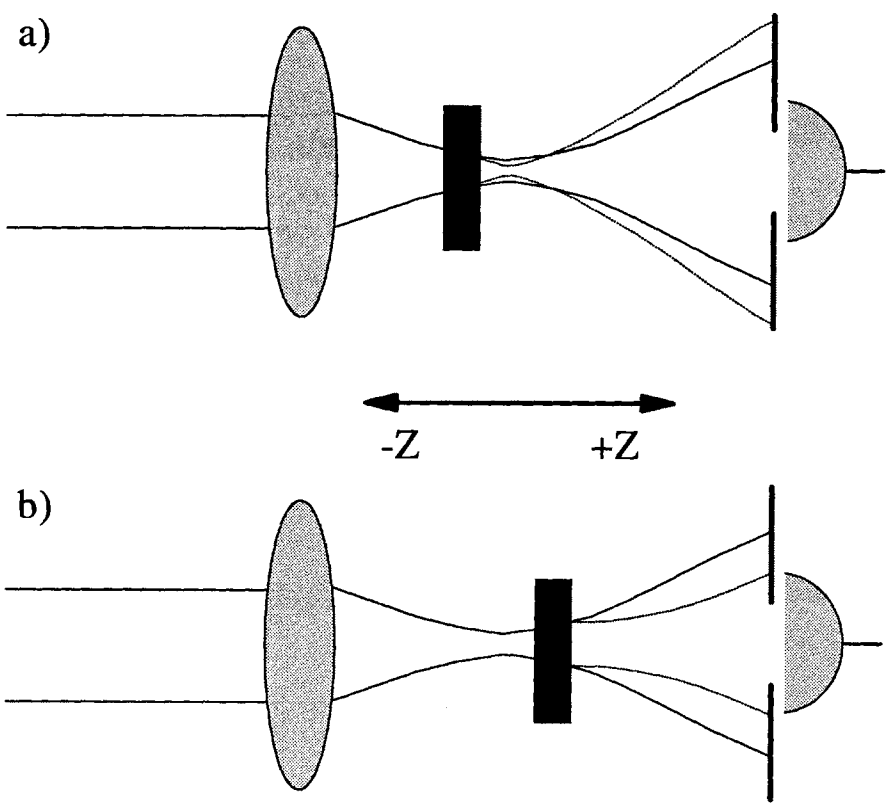

Figure 7.2 Self action of a material with a positive nonlinear refractive index a) Pre-focal minimum. b) Post-focal maximum.

of dividing the closed aperture scan by an identical open aperture Z-Scan. The result being nearly the equivalent to having the closed aperture Z-Scan of a sample with no nonlinear absorption but the same nonlinear refraction as the original sample.

7.2 Theory of Z-Scan in Thin Samples

There are several complete discussions of the theory of the open and closed aperture Z-Scans in thin samples [1], [2], [3], [4]. Therefore, there will not be a thorough discussion here, rather only the minimum information needed to understand the basic concepts will be mentioned, along with a few other salient points.

If the sample length is less than the confocal beam parameter, and if the phase changes in the field caused by the nonlinear interaction are not transformed into amplitude changes within the sample, then the sample is considered thin. In this case, the refractive process is referred to as "external self action." Assuming a thin sample and implementing the slowly varying envelop approximation(SVEA), the wave equation can be separated into an equation for phase and an equation for the irradiance. So that

$$\frac{d\Delta\phi}{dz'} = k\Delta n(I) \qquad (7.1)$$

and

$$\frac{dI}{dz'} = -(\alpha_o + \beta I)I, \qquad (7.2)$$

where $\Delta n(I)$ is the change in the index of refraction as defined in Chapter 2, β is the two photon absorption(2PA) coefficient, k is the magnitude of the wave vector in free space, α_o the residual linear absorption, and z' is the propagation distance within the sample, which should not be confused with z, the sample position with respect to the focal plane.

Fitting programs exist that can determine the nonlinear parameters from Z-Scan data in the case of large depletion, large phase shifts and for thick samples, however they

can be extremely time consuming and/or may require simplifying approximations. The elegance of the single beam Z-Scan stems from the fact that it is highly sensitive and simple to perform, yet in the case of thin samples with small phase shift and depletion can be analyzed without any fitting procedure. The beams confocal parameter Z_o and the nonlinear refractive index are both immediately apparent from a Z-scan in a thin sample with a small phase shift and negligible nonlinear absorption. Independent of exact thickness, the separation in Z between the peak and valley of a closed aperture Z scan when $|\Phi_o|<1$ is given by

$$\Delta Z_{p-v} \cong 1.7\, Z_o, \qquad (7.3)$$

where the beam's spot size is

$$\omega_o = \sqrt{\frac{Z_o \lambda}{\pi}}. \qquad (7.4)$$

For a cubic nonlinearity and relatively small on axis phase shifts ($|\Phi_o|<\pi$), the change in transmission between the peak and valley ($\Delta t_{p-v} = T_p - T_v$) is given by

$$\Delta T_{p-v} \cong 0.405(1-S)^{0.25}\left|\Delta\Phi_o\right| \quad \text{for} \quad \left|\Delta\Phi_o\right| \le \pi. \qquad (7.5)$$

So that for small phase distortion ΔT_{p-v} is linearly dependent upon $|\Delta\phi_o|$. With S=0.4, i.e. a 40% transmitting aperture

$$\Delta T_{p-v} \cong 0.406\left|\Delta\Phi_o\right|, \qquad (7.6)$$

where the on axis phase shift at focus is related to the nonlinear refractive index by

$$\Delta\Phi_0(t) = \frac{2\pi}{\lambda}\Delta n_o(t)\frac{1-e^{-\alpha L}}{\alpha}, \qquad (7.7)$$

where α is the linear absorption. Therefore, if the experimental apparatus is capable of detecting a one percent transmission change, then phase changes corresponding to a $\lambda/250$ wave front distortion are detectable.

It has been shown [5], that for an open aperture Z-scan where 2PA is present, that from equation (7.2) the irradiance at the exit surface of the sample can be given as

$$I(L,r,t,z) = \frac{I(0,r,t,z)\exp(-\alpha_o L)}{1+q(r,t,z)}, \qquad (7.8)$$

where $q(r,t,z,t)=\beta I(0,r,t,z)L_{eff}$, $L_{eff}= [1-\exp(-\alpha_o L)]/\alpha_o$, and z is the sample position. Here,

$$I(0,r,t,z) = \frac{I_o \exp[-2(r/\omega_o)^2 - (t/t_o)^2]}{1+(z/z_o)^2}, \qquad (7.9)$$

with the confocal parameter being $Z_o = \frac{\pi\omega_o^2}{\lambda}$. Now, removing the aperture is equivalent to placing the detector at the exit surface of the sample. Such an open-aperture Z-scan allows us to ignore the phase changes, hence the normalized transmittance can be written as

$$T(z) = \frac{1}{\sqrt{\pi}\, q(0,0,z)} \int_{-\infty}^{\infty} \ln\left[1+q(0,0,z)\exp(-\tau^2)\right] d\tau. \qquad (7.10)$$

The only unknown in this equation is the β in q(0,0,z), so the open aperture Z-scan will give the 2PA coefficient. **Figure** (7.3) shows a plot of T(0) as a function of $q(0,0,0) = \beta I_o L_{eff}$, which can be used to determine β directly from an open aperture Z-Scan without fitting. Therefore, for a thin sample it is possible to obtain both β and n_2 from the data without fitting.

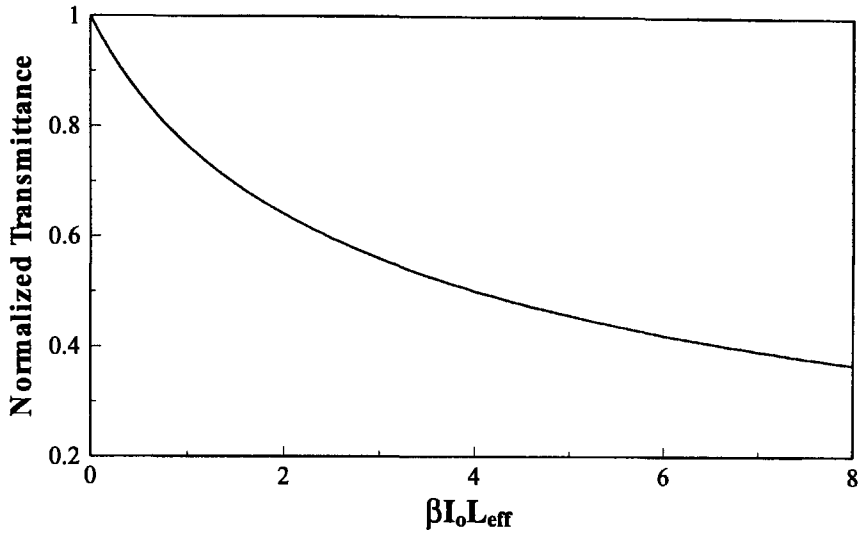

Figure 7.3 Normalized transmittance for an open-aperture Z scan at z = 0 as a function of $\beta I_o L_{eff} = q(0,0,0)$. From this curve β can be determined without fitting the data.

7.3 Thick Media

When materials have a thickness that is greater than the depth of focus (internal self-action), the analogy of the nonlinear optical sample being a simple lens with an irradiance dependent focal length is no longer valid. Rather, a distributed lens model can be used [6], where the thick medium is regarded as a stack of thin lenses whose focal lengths are dependent upon the local beam irradiance. Therefore, this problem is solved numerically by splitting the sample into m different lenses. The focal length of the first lens is determined by the initial irradiance of the beam, and then the irradiance of the beam at the output of the lens is used to determine the focal length of the next lens. This is repeated until the beam exits the sample, so that the accuracy of this process depends upon the number of lenses or iterations that are used. Therefore, as a sample becomes much thicker than the confocal parameter the total ΔT_{p-v} will no longer continue to increase, and using the thin sample theory would cause one to overestimate the effects of

a given nonlinearity upon an incident pulse. Therefore, it can be useful to look at the effective interaction length of the thick sample

$$L_{eff} = \frac{\Delta T_{p-v}(\text{thick})}{\Delta T_{p-v}(\text{thin})} L, \qquad (7.11)$$

where $\Delta T_{p\text{-}v}$ (thick) is calculated using the distributed lens method and $\Delta T_{p\text{-}v}$ (thin) is calculated using the equations from the previous section. Additionally, the width of the Z-scan or the separation in distance between the peak and the valley no longer remains constant as the sample becomes thick. The relation for the peak to peak separation of a thick and thin sample is

$$\Delta Z_{p-v}(\text{thick}) = \left[(L / n_o)^2 + \Delta Z_{p-v}^2(\text{thin}) \right]^{\frac{1}{2}}, \qquad (7.12)$$

where n_o is the linear refractive index [1], [6].

7.4 Actual Z-Scan Configuration

For all of our Z-Scan measurements,(including the modified techniques) we used the same basic set up as was used for the PDMT and autocorrelation measurements. This is because it was difficult to realign the autocorrelation and PDMT set up, therefore we did not want to be continuously realigning it from scratch. Furthermore, we needed the autocorrelation set up to check the pulse width of the Ti:sapphire every day that it was used, and the modulated Z-Scans that we performed also needed a configuration like the PDMT.

Hence, the set up that we used for our PDMT experiments and our Z-Scan measurements were the same, however the procedures were implemented by translating different stages. The Z-Scan was performed by moving the sample in Z through the focus of the laser beam. Whereas, the PDMT and autocorrelation measurements were performed by varying the relative path delay between the two beams, by translating the

stage upon which the prism was mounted. We performed our equivalent of the traditional Z-Scan with either the chopped beam that went through the prism, or with both beams at once. Additionally, we always performed the Z-Scan with zero path delay between the two beams, although with a small Pulse Delay Modulation(PDM) of about 5- 10 wavelengths to average out the fringes. We also ensured that the sample was placed at the laser beam's focus, when we implemented the PDMT and autocorrelation measurements.

7.5 Two beam Z-Scan

As mentioned before, we performed our Z-Scan measurements using the same configuration as we used for the PDMT measurements, yet the two measurements were implemented differently. However, we still wanted to use the full intensity of the laser beam, when performing the Z-Scan. Therefore, we used the energy from both arms of the Michelson interferometer as our laser source, so as to achieve this goal without disrupting the autocorrelation(and PDMT) set-up. Initially, this appeared to be a good idea, because the two beams together consisted of almost twice the energy of the prism beam alone. Hence, we were able to detect a larger Z-Scan signal, and obtained a larger signal to noise ratio than with only one beam. However, using the two beams turned out to significantly complicate the analysis, and added significant sources of error to our results.

7.5.1 Two Beam Effective Nonlinearity

From (7.1) and (7.2), it becomes obvious that we cannot treat the net intensity upon the sample, when performing the Two Beam Z-Scan as simply the sum of the individual intensities. Rather, the electric fields must be added, and the extra cross terms must be included. This equivalent intensity is then used to take into account the two beam effective nonlinearity when modeling the Z-scan. In addition to demonstrating how we

attempted to model the Two Beam Scan, the following calculation demonstrates how several sources of error are added to our analysis when performing the Two Beam Z-Scan.

Now, it is of course possible to go back to Maxwell's Equations and derive the two beam equivalents of (7.1) and (7.2). However, another method of obtaining the same result is by plugging in the individual electric fields into (7.1) and (7.2). Since, we had effectively zero linear absorption in our samples and we assume small nonlinear absorption, equations (7.1) and (7.2) can be written in terms of the incident electric fields as

$$\frac{d\Delta\phi}{dz'} = k\Delta n(|E_1 + E_2|^2), \qquad (7.13)$$

and

$$\frac{dI}{dz'} = -\beta\left(|E_1 + E_2|^2\right)^2. \qquad (7.14)$$

Starting with the absorption term, we obtain

$$\frac{dI}{dz'} = -\beta\left(|E_1 + E_2|^2\right)^2. \qquad (7.15)$$

$$= -\beta\left[I_1 + I_2 + E_1E_2^* + E_2E_1^*\right]^2$$

$$= -\beta[I_1^2 + I_2^2 + E_1^2E_2^{*2} + E_2^2E_1^{*2} + 2I_1I_1 + 2I_1E_1E_2^* + 2I_2E_2E_1^* + 2I_2E_1E_2^* + 2I_2E_2E_1^* + I_1I_2 + I_1I_2]$$

$$= -\beta\left\{I_1^2 + I_2^2 + 4I_1I_2 + 2(I_1 + I_2)[E_1E_2^* + E_2E_1^*]\right\}$$

Here, the electric fields of the prism beam and the corner cube beams respectively are

$$E_1 = f(t)\alpha_1E_o \exp(-j\omega t), \qquad (7.16)$$

and

$$E_2 = \alpha_2 E_o \exp\{-j[\omega t + \Delta\tau\cos(\omega_s t)]\}, \qquad (7.17)$$

where α_1 and α_2 are the relative magnitudes of the electric fields, ω and ω_s are the optical and speaker frequency in radians per second respectively, and $\Delta\tau$ is the maximum extent of the temporal delay caused by the speakers oscillation δ ($\tau = \delta/c$). The last term in equation (7.15) is a rapidly varying cosine with a period of an optical cycle. However, we modulate the speaker by about 10 wavelengths, so this term averages to zero. Hence,

$$\frac{dI}{dz'} = -\beta\{I_1^2 + I_2^2 + 4I_1 I_2\} \qquad (7.18)$$

where the same effective intensity will be obtained for the phase change equation (7.10). A procedure similar to the one above must be followed, and the index change must be then be time averaged

$$\langle \Delta n_o(t) \rangle = \frac{\int_{-\infty}^{\infty} \Delta n_o(t) I_o(t) dt}{\int_{-\infty}^{\infty} I_o(t) dt} \qquad (7.19)$$

as done by Sheik - Bahae et. al. [2] with the single beam Z-scan..

7.5.2 Effects of Lock in Amplifier

The purpose of this section is to find out how the lock-in amplifiers affect the detected signal for the case of the 2 Beam Z-Scan. We will assume that the modulation function imposed by the chopper with a modulation frequency ω_c, in radians per second is

$$f(t) = \left\{\frac{1+\cos(\omega_c t)}{2}\right\} = \cos^2\left(\frac{\omega_c}{2} t\right), \qquad (7.20)$$

instead of the generalized Fourier series function used as a demonstration with a single beam in Chapter 6. The actual shape of the modulation function is a distorted square pulse, which although asymmetric is very similar to this cosine squared function.

We found that both the nonlinear absorption and nonlinear refraction terms were proportional to $I_1^2+I_2^2+4I_1 I_2$. The input to the lock-in amplifier is proportional to

$$V_i \propto f^2(t)I_1^2 + I_2^2 + 4f(t)I_1I_2. \qquad (7.21)$$

$$\propto I_2^2 + I_1^2\left\{\frac{1+\cos(\omega_c t)}{2}\right\}^2 + 4I_1I_2\left\{\frac{1+\cos(\omega_c t)}{2}\right\},$$

which after being multiplied by $\cos(\omega_c t)$ in the Phase Sensitive Detector (PSD) becomes

$$V_{PSD} \propto I_2^2\cos(\omega_c t) \qquad (7.22)$$

$$+I_1^2 \times \frac{1}{4}\{\cos(\omega_c t)+2\cos^2(\omega_c t)+\cos^3(\omega_c t)\}$$

$$+4I_1I_2 \times \frac{1}{2}\{\cos(\omega_c t)+\cos^2(\omega_c t)\}.$$

Hence, after passing through the lowpass filters, only the cosine squared terms survive and the output of the lock-in amplifier is proportional to

$$V_{out} \propto I_2^2 + 4I_1I_2. \qquad (7.23)$$

Therefore, the lock-in amplifier has the effect of eliminating the background term from the unmodulated beam, so that equal intensity beams under ideal circumstances would give us an effective intensity that is a factor of five instead of a factor of two times greater than the intensity of one beam. This same argument holds for the peak to background ration of the second order intensity autocorrelation, rather than obtaining a six to two (3 to 1) peak to background ratio a five to one would be realized under ideal circumstances.

7.6 Pulse Delay Modulated Z-Scan

A Pulse Delay Modulation Z-Scan(PDM Z-Scan) is an open or closed aperture Z-Scan that is performed with PDM. The PDM Z-Scan is performed in the same manner as the Two Beam Z-Scan, except that the amplitude of the speaker modulation is much greater than the pulse width. The second lock-in amplifier is then locked in at twice the frequency of the speaker, so that only the irradiance dependent portion of the Z-Scan is measured. We implemented this measurement technique, because the signal to noise ratio was greatly increased by the addition of the additional amplifier and line of filters. We achieved the best signal to noise ratio of all the measurement techniques with this technique, however unlike the traditional Z-Scan technique there is no easy way to extract the nonlinear constants from the data. In fact, the modeling of the PDM Z-Scan was more difficult than the PDMT or the 2 Beam Z-Scan, therefore as will be explained in Chapter 8, we were only able to indirectly obtain results from the technique.

REFERENCES FOR CHAPTER 7

[1] A. A. Said, "Development and Application of a Nonlinear Optical Characterization Technique", Phd. Diss., University of North Texas, Denton, TX, 1991.

[2] M. Sheik-Bahae, A. A. Said, T-H. Wei, D. J. Hagan, and E. W. Van Stryland, "Sensitive Measurement of Optical Nonlinearities Using a Single Beam", *IEEE J. Quantum Electron.* **QE-26**, 760-769, (1990).

[3] M. Sheik-Bahae, A. A. Said, and E. W. Van Stryland, "High-sensitivity, single-beam n_2 measurements," *Opt. Lett.* **14**, 955-957 (1989).

[4] J. R. Desalvo, "On Nonlinear Refraction and Two-Photon Absorption in Optical Media", Phd. Diss., University of Central Florida, Orlando FL, 1993.

[5] A. A. Said, M. Sheik-Bahae, D. J. Hagan, T. H. Wei, J. Wang, J. Young, and E. W. Van Stryland, "Determination of bound-electronic and free-carrier nonlinearities in ZnSe, GaAs, CdTe, and ZnTe," *J. Opt. Soc. Am. B* **9**, 405-414 (1992).

[6] M. Sheik-Bahae, A. A. Said, D. J. Hagan, M. J.Soileau, E. W. Van Stryland, "Nonlinear refraction and optical limiting in thick media," *Opt. Eng.* **30**, 1228-1235 (1991).

CHAPTER 8

MATERIAL CHARACTERIZATION

This chapter describes our implementation of the PDMT, Z-Scan and the PDM Z-Scan, all of which were described earlier. The results of our calibration process and the details particular to a given experiment or experimental run will be given. Additionally, we will show the results of these experiments in detail, however the analysis and comparison to the theoretical results will be left until the next chapter.

8.1 System Optimization

In all of the scans, the beam in the prism arm of the interferometer was amplitude modulated with the chopper wheel at 2.54 KHz ± 10 Hz. The PDM frequency of the speaker was always modulated at 20 Hz, which was a reduction from our initial trial at 100 Hz as Miller [1] used. This reduction in frequency was partially to move the frequency farther away from the line frequency and its first harmonic at 60 and 120 Hz respectively. But, the main reason was to increase the difference between the modulation frequency of the chopper and the speaker. Optimally, the time constant of the lock-in amplifier should be 3-5 times as long as the period of any signal for averaging purposes. The modulation frequency of the chopper was already near its maximum, so that it could not be altered significantly. Therefore, so as to achieve this averaging, the time constant of the first lock-in amplifier needed to be increased, but then this would cause another problem. Too much averaging by the first lock-in amplifier which was locked in at the chopper's frequency could cause the PDM signal to be partially averaged out, therefore

CHAPTER 8

MATERIAL CHARACTERIZATION

This chapter describes our implementation of the PDMT, Z-Scan and the PDM Z-Scan, all of which were described earlier. The results of our calibration process and the details particular to a given experiment or experimental run will be given. Additionally, we will show the results of these experiments in detail, however the analysis and comparison to the theoretical results will be left until the next chapter.

8.1 System Optimization

In all of the scans, the beam in the prism arm of the interferometer was amplitude modulated with the chopper wheel at 2.54 KHz ± 10 Hz. The PDM frequency of the speaker was always modulated at 20 Hz, which was a reduction from our initial trial at 100 Hz as Miller [1] used. This reduction in frequency was partially to move the frequency farther away from the line frequency and its first harmonic at 60 and 120 Hz respectively. But, the main reason was to increase the difference between the modulation frequency of the chopper and the speaker. Optimally, the time constant of the lock-in amplifier should be 3-5 times as long as the period of any signal for averaging purposes. The modulation frequency of the chopper was already near its maximum, so that it could not be altered significantly. Therefore, so as to achieve this averaging, the time constant of the first lock-in amplifier needed to be increased, but then this would cause another problem. Too much averaging by the first lock-in amplifier which was locked in at the chopper's frequency could cause the PDM signal to be partially averaged out, therefore

the time constant of the first lock-in amplifier should be several times shorter than that of the PDM. Therefore, the PDM or the frequency of the speakers modulation was all that could be changed. After, decreasing the frequency of the speaker to 20 Hz, we then increased the time constant of the first lock-in amplifier to 3 ms up from the original 1 ms.

In all of our experiments the last lock-in amplifier before the data acquisition system was set with the prefilter at 3 seconds and the post filter at 1 second to maximally reduce the noise and fluctuations through the use of its filters. This frequency was not increased, because the time between stage movements also needed to be greater than the filters time constant so as to prevent distortion of the scan, which was caused if there was not enough averaging. So, we initially switched to the 20 Hz speaker frequency so that we could increase the time constant of the prefilter on the first lock-in amplifier to 3 ms. I hoped that this would ensure that the first lock-in amplifier would be able to optimally average the chopper signal without averaging out that of the speaker modulation. As it turned out there was very little change in the signal to noise when performing the scans with both of the modulations. Rather, the reduction in system noise as perceived from the output of the lock-in amplifier by modulating at this lower frequency was most significant when we were only locking in on the chopper's amplitude modulation as in the case of the Two beam Z-Scan and the autocorrelation. In fact, we determined experimentally that a modulation amplitude of 5-10 fringes at this frequency was ideal for increasing the signal to noise ratio by ridding the system of spurious noise caused by the instability of the corner cube on the speaker.

Additionally, the stage that performed the Z-translation had a resolution of 0.6254 microns per step, where a step is the minimum unit by which the stage can be moved by the computer control. There are approximately 800 of these steps per revolution of the

micrometer knob. On the other hand, the stage that performed the femtosecond autocorrelations and PDMT scans needed a much greater resolution and stability. Hence, an adapter was machined so that we could use a differential micrometer with a resolution of 0.0099 microns per step on a larger more stable stage. Considerable time was spent determining the optimal manner by which to take the data, however there really was no ideal procedure for all possible circumstances. This is because increasing the time constant of the lock-in amplifier decreased the frequency bandwidth and the detected noise. However, for the data to still be accurate, we needed to wait longer between shots or groups of shots. Hence, the entire scan became longer and the presence of the drift in the argon causes all the detrimental effects to the alignment of the system that were described in Chapter 6. Similarly, the uncertainty caused by the computer storage speed caused us to make a trade off when it came to determining the optimum number of shots to average per group as well as the time between shots. However, we still wanted to maintain some consistency between the runs that we analyzed, even though the procedure may not be ideal for all the different experiments. We finally decided on using 1 shot per group(or data point), 200 steps of translation and a 10 second delay between groups, as well as 100 groups per experiment.

Furthermore, the beam in the prism arm was between 75-85 percent Gaussian, and the one hitting the small corner cube accrued more loss and distortion, so that it was between 60-70 percent Gaussian with only about 80 percent of the intensity of the beam in the prism/chopper arm. In any event, by looking at the beam profiles on the CCD array, as well as the shape of the Z-Scans performed with thin samples, we determined that the spot size was approximately 14 μm. Due to slight misalignment and lack of symmetry between the beams, the effective spot size is actually smaller for the case of two beams than with just one. Additionally, the pulse width of the Ti:sapphire was

determined with the real time autocorrelator to be approximately 168 fs FWHM on the days of the of Z-scan measurements. The PDMT and autocorrelation scans were performed on a different day and their pulse widths will be discussed along with the results of the fits.

8.2 Autocorrelation

Our first task was to show that the intensity autocorrelation obtained with a 2PA was proportional in shape to $G_2(\tau)$ shown in Chapters 5 and 6. This has already been shown to be true both theoretically [2] and experimentally [1], however we needed to verify that this was true with out experimental arrangement. Therefore, we performed an autocorrelation with both a 2PA crystal(ZnSe), and a second harmonic crystal(LiO_3), then we compared the results in **Figure** (8.1). The laser was less stable and its pulse width was longer than usually, however we demonstrate that the pulse shape and width of the two different autocorrelations are proportional by scaling and flipping the sign of the ZnSe data to match that of the LiO_3.

The next step was to insure that the scans with the second harmonic crystal in our PDM experimental set up were in fact proportional to the second order autocorrelation function. This would then verify that we obtained 2PA scans that were also proportional to this function. The second harmonic crystal was used instead of the 2PA for the following reasons: provided a much larger signal, the second harmonic crystal was already in position from performing the interferometric autocorrelations, we always aligned the system with the second harmonic crystal before using 2PA, and the blue visible light was easier to work with..

The fits were performed using the fitting procedures that are built into Easy Plot and/or Sigma Plot software packages. They gave similar results, however Easy Plot was

very slow, difficult to use efficiently and regularly failed to converge. The fits shown were performed using the hyperbolic secant's scaled autocorrelation and derivative functions as shown in

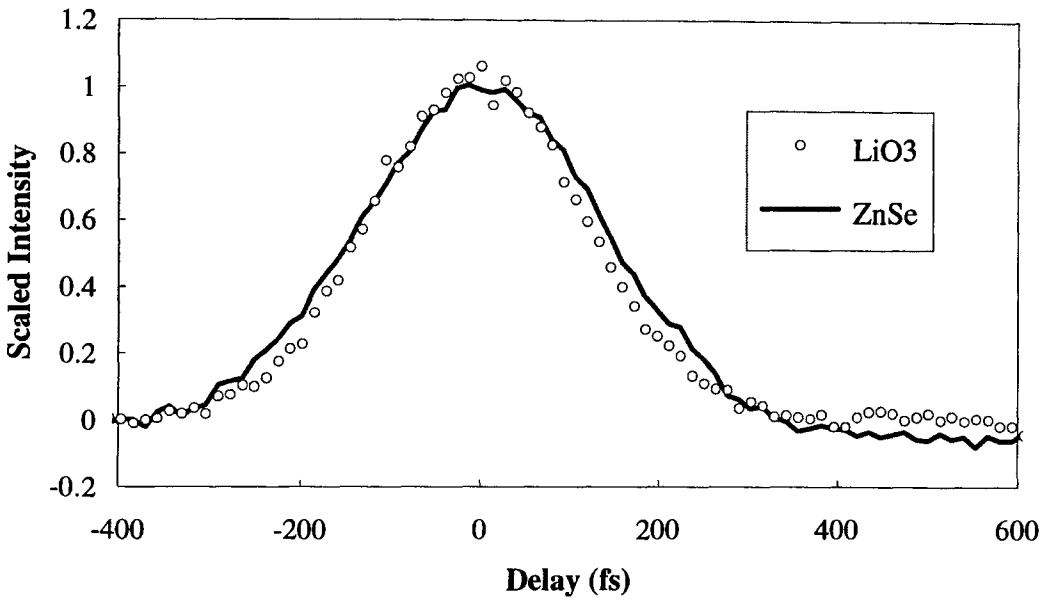

Figure 8.1 Autocorrelation data for 5mm thick $LiIO_3$ crystal and 3.2 mm thick ZnSe sample with the magnitude of the ZnSe scaled and flipped for comparison of pulse implied pulse shape and width.

Chapter 6. However, several of the fits were performed with the respective Gaussian functions and the residuals and the total error as given by Sigma Plot were higher when the Gaussian functions were used. The conclusion is that the hyperbolic secant function gave a better fit. **Figure** (8.2) shows the autocorrelation along with its fit, where $a=0.91\times10^{-11}$, b= 1.04559, c= 8.867 fs and d = 84.2 fs, so that the FWHM of the pulse is approximately 148.4 fs with an error of at most ± 5 fs. We obtained the times for c and d, by calibrating the path length change caused by the translation stage movement into

time(time = distance/3×10^8m/s). This pulse width compares to one of 127 ± 20 fs obtained using the interferometric set up as a real time correlator. The error in measurement with the real time autocorrelator is because we just put a microscope cover slide in the path of the one beam without a mount of any kind. Therefore, the microscope slides were not put in the path perfectly perpendicular to the beam, it was occasionally difficult to judge the time shift from the scope and most importantly we kept breaking the slides so that their thicknesses were never known exactly. On the other hand, we went through a great deal of trouble to obtain a very stable stage with a high resolution, so all the error in that method is derived from the electronic mechanisms that we used to drive the stepper motor. Therefore, the data shown below is believed to be more accurate than the real time autocorrelator, and it demonstrates that we are able to get the autocorrelation function out of the first lock-in amplifier.

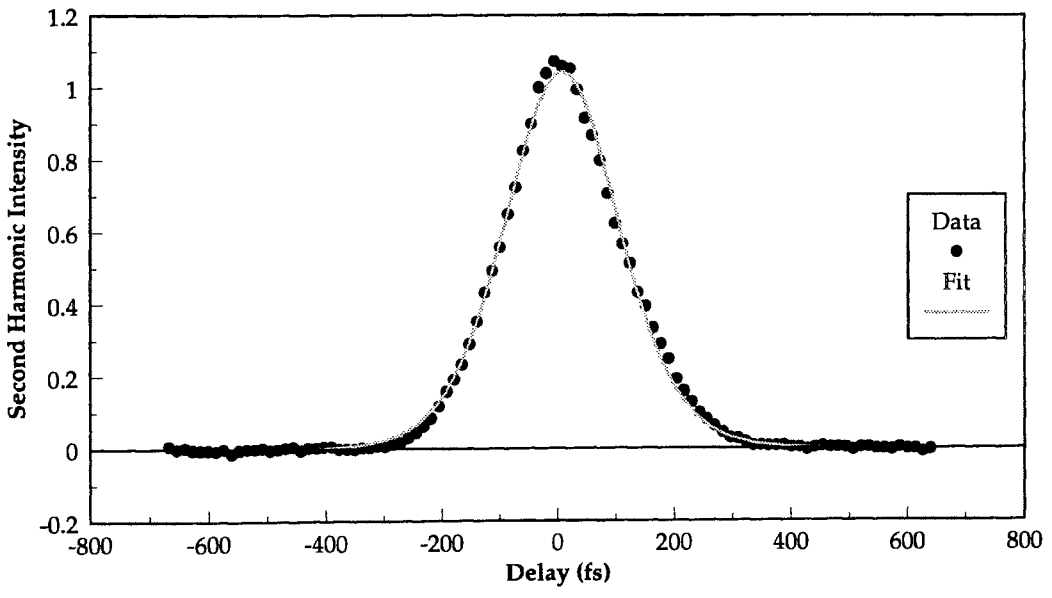

Figure 8.2 Autocorrelation of $LiIO_3$ with fit to the second order intensity autocorrelation function for a $sech^2$ function.

8.3 PDMT vs. Derivative of Autocorrelation

We determined that if the magnitude of the speaker modulation was 25 - 30 fringes, that we would obtain a reasonable signal to noise ratio in our PDMT scan. As mentioned in Chapter 6, when the magnitude of the speaker oscillation is relatively small, then the PDMT scan should be proportional to the first derivative of the autocorrelation function. Therefore, we fit the PDMT data to the scaled derivative as given in Chapter 6, so as to prove that we were in fact not distorting the scan by using too large a modulation. **Figure** (8.3) shows the PDMT data and its fit to the derivative of the autocorrelation function, where the fitting parameters are a= -1.947×10^{-4}, b= 1.046×10^{-2}, c= .7 fs and d = 91 fs. The FWHM of the corresponding autocorrelation function would be 161 fs, which only differs from that of the autocorrelation performed earlier by about 9 percent. This

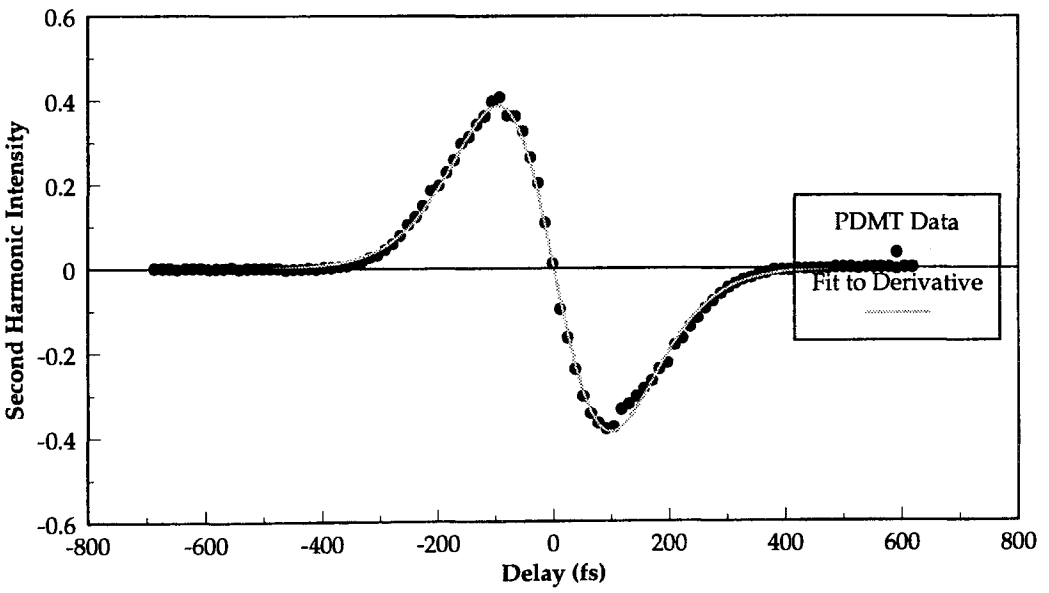

Figure 8.3 PDMT scan and its fit to the derivative of the second order intensity autocorrelation function for a hyperbolic secant squared shaped pulse.

difference can be partly due the change in the laser's pulsewidth, as well as a relatively small deviation from the true derivative of the autocorrelation function. This is in good agreement with the broadening PDM_{broad} expected from a speaker modulation with a magnitude of $\delta = 19.5\ \mu m$ (25 780 nm fringes) for a 148 fs FWHM autocorrelation of

$$PDM_{broad} \cong \sqrt{\left(AC_{FWHM}\right)^2 + \left(\frac{\delta}{c}\right)^2} \cong 162 \quad \text{fs.} \qquad (8.1)$$

The modulation of 25 fringes was needed to obtain a good signal to noise ratio(SNR). As a final comparison in **Figure** (8.4) the PDMT data is plotted against the derivative of the autocorrelation obtained in **Figure** (8.2). This is achieved by putting the pulse width from **Figure** (8.2) into the equation of the scaled derivative and then optimizing the shift and magnitude parameters

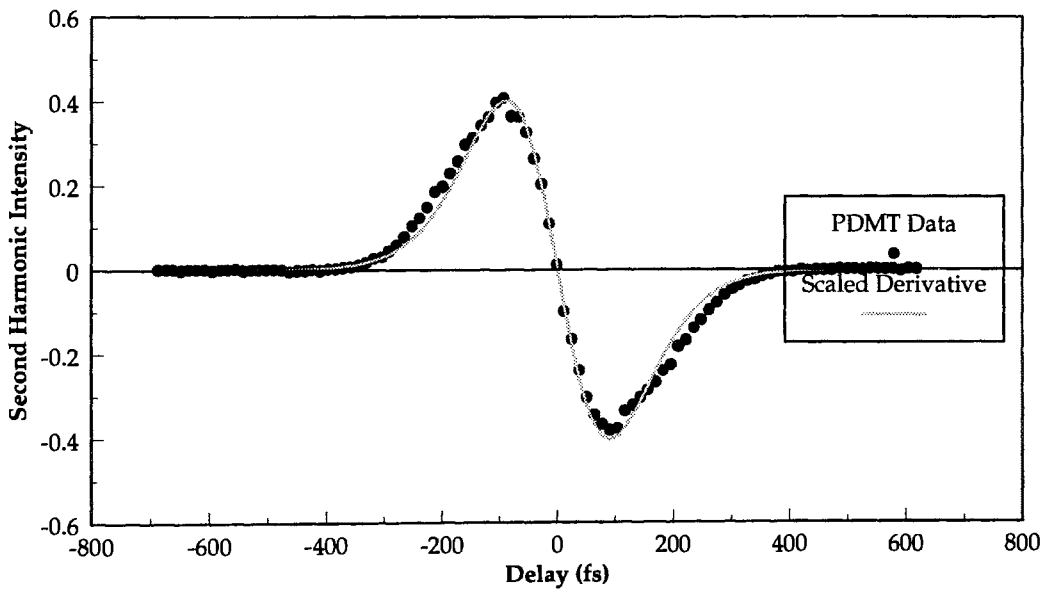

Figure 8.4 PDMT data plotted against the derivative of the autocorrelation from **Figure** (8.2).

8.4 Z-Scan Measurements

From within the PDMT setup, we performed Z-scans with one beam and with both beams with 168 femtosecond pulses at a wavelength of 780 nm upon a 3.2 mm thick ZnSe sample and a clear 1.1 mm thick ZnS sample. We obtained data for the ZnSe sample with the two beam open aperture, two beam closed aperture and single beam open aperture Z-scans, whereas we could not obtain useful data for the ZnS with any of the above measurement techniques. Additionally, some signal was obtained for the ZnSe with the single beam closed aperture scan, but we could not fit it because of the low SNR. Through, the use of a CCD array, we were able to determine that the spot size of the laser pulse at the focus of a 7.5 cm lens was approximately 14 μm, and the irradiance at the sample due to the prism beam was about 4.3×10^2 GW/cm^2, whereas the intensity of the beam in the corner cube arm was about 80 percent of that. For all of the fits shown we used the program Zscanf1, which is a FORTRAN program written by Dr. Ali Said [3]. This code assumes that the sample is thin, and as defined in Chapter 7 the 3.2 mm ZnSe sample with a refractive index of 2.519 at 780 nm does not fit the requirements for a thin sample. However, from previous work by Sheik-Bahae et al. [4]for the ZnSe sample there should be less than a 10% error. Therefore, there is a small error inherent in our fitting procedure that would cause us to underestimate the magnitude of the nonlinear coefficients. The open aperture single beam Z-Scan and its fit where β = 10 cm/GW, I_o = 4.3×10^2 GW/cm^2, and the spot size of ω_o = 15 μm is shown in **Figure** (8.5). We fit the data to the 2PA and the spot size, where we believe that the spot size is different between the single and double beam Z-scans, because the two beams are not identical. They either do not remain perfectly collinear, and/or they are not directly on top of each other. Spatially, the intensity drops off more quickly because of this misalignment, and changes the effective spot size.

After performing the single beam Z-Scan, we then performed the Two Beam Z-Scan, where the intensity of the second beam was 80% of the first beam so that the total intensity upon the ZnSe sample was 7.8×10^2 GW/cm^2. While using the relationships in Chapter 7, the effective intensity upon the sample that takes into account the two beam effective nonlinearity is calculated to be 1.82×10^3 GW/cm^2. We show the open aperture Z-Scan, closed aperture Z-Scan, and the divided scan with fits that use the theoretical effective intensity in **Figure** (8.6), **Figure** (8.7), and **Figure** (8.8) respectively, Here β, n_2 and ω_o were 3.5 cm/GW, 2.5×10^{-11} esu and 14 μm respectively, so the two photon absorption is a factor of three less than calculated from the single beam Z-can and the spot size appears to be 1 μm smaller.

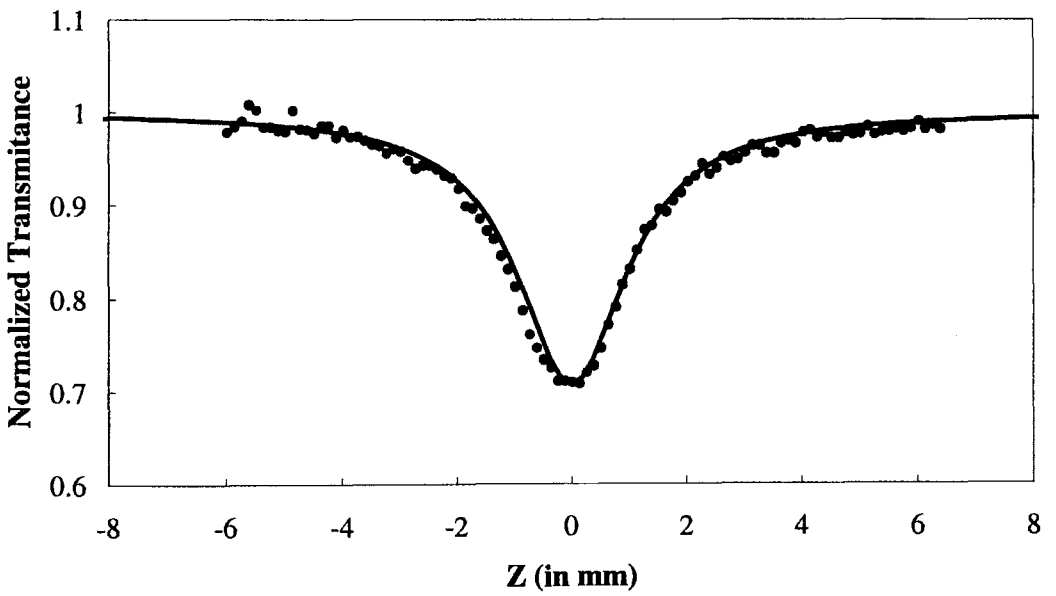

Figure 8.5 Single beam open aperture Z-Scan performed at 780 nm with ZnSe sample. ($I = 4.3\times10^2$ GW/cm^2 and β =10 cm/GW)

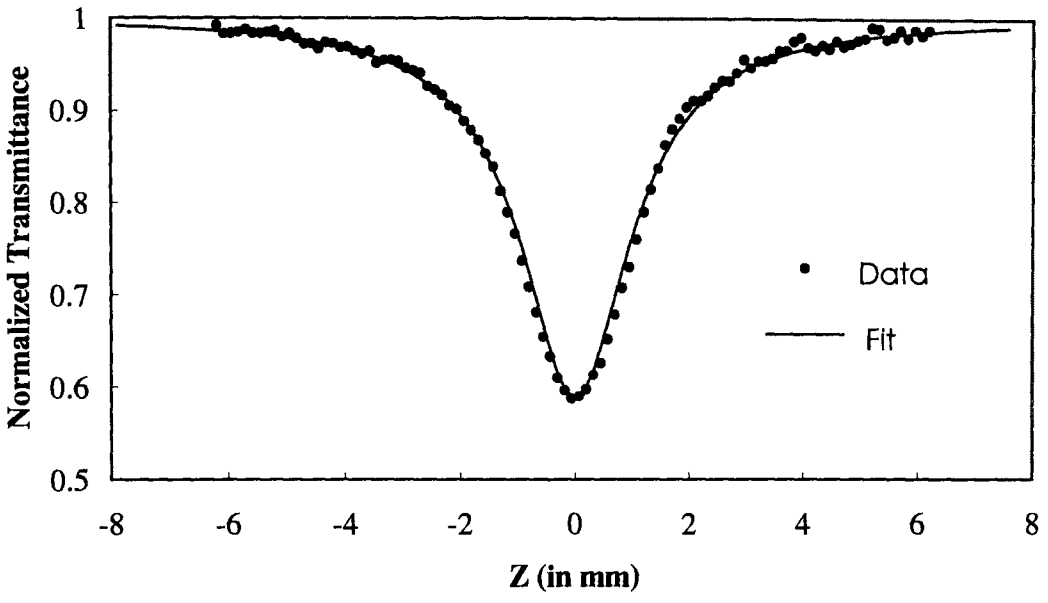

Figure 8.6 Two beam open aperture Z-Scan performed at 780 nm with ZnSe sample. ($I = 1.82\times10^2$ GW/cm^2 and β =3.5 cm/GW)

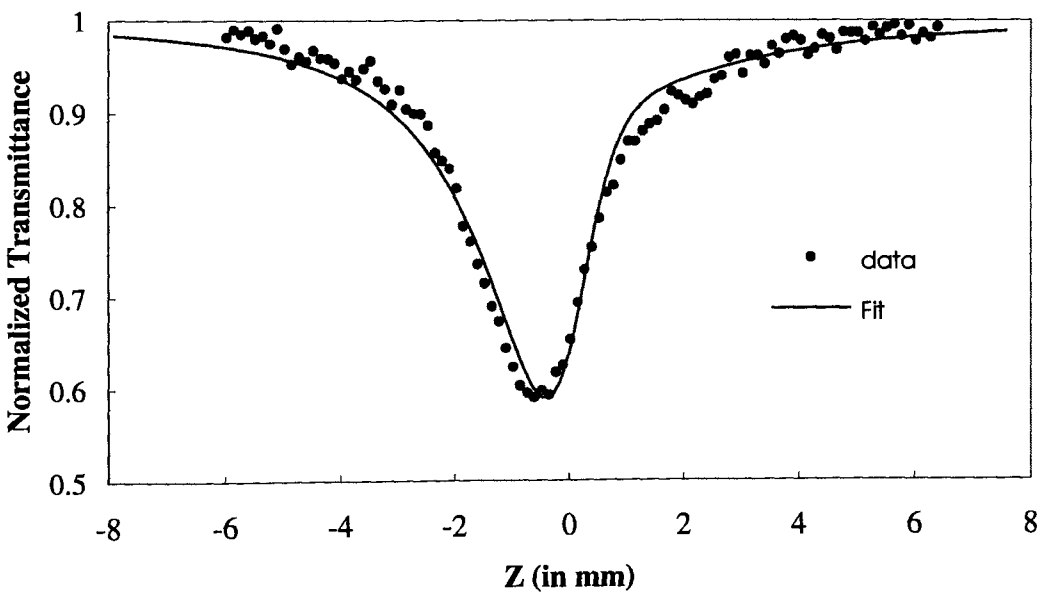

Figure 8.7 Two beam closed aperture Z-Scan performed at 780 nm with ZnSe sample. ($I = 1.82\times10^2$ GW/cm^2 and β =3.5 cm/GW, $n_2 = 2.5\times10^{-11}$ esu)

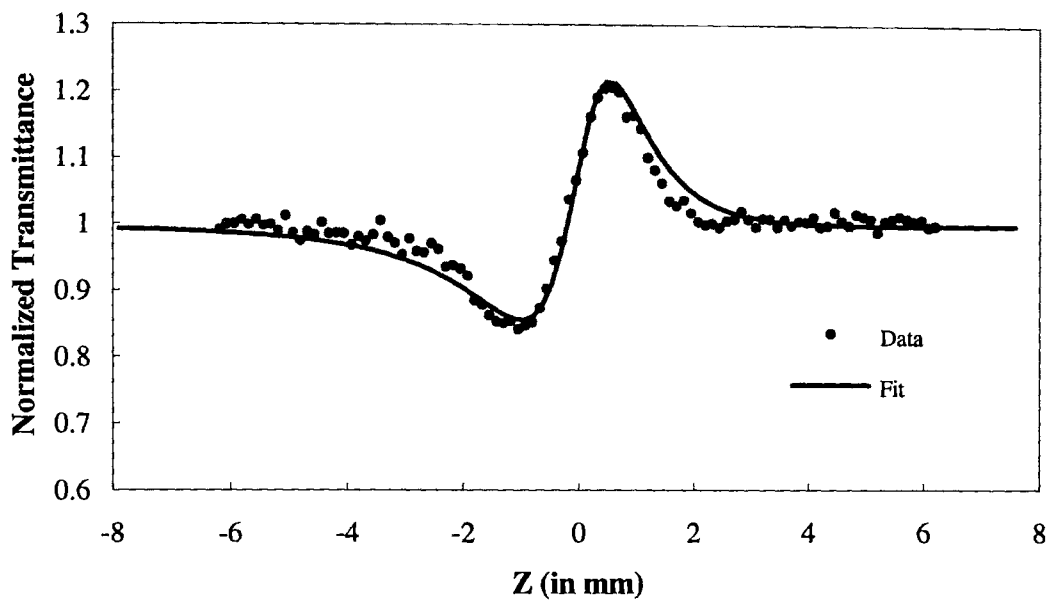

Figure 8.8 Closed aperture Z- scan divided by open aperture Z-scan performed at 780 nm with ZnSe sample. ($I = 1.82\times10^{3}$ GW/cm^2 and β =3.5 cm./GW, $n_2 = 2.5\times10^{-11}$ esu)

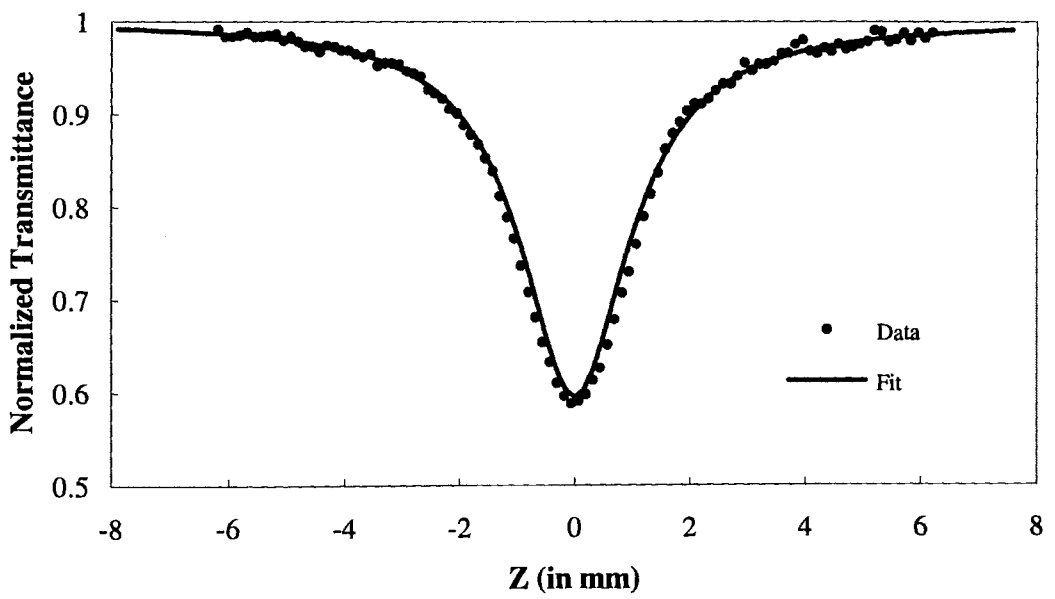

Figure 8.9 Two beam open aperture Z-Scan performed at 780 nm with ZnSe sample. ($I_o = 7.81\times10^{2}$ GW/cm^2 and β =10 cm/GW, $n_2 = 5.7\times10^{-11}$ esu)

In **Figure**'s (8.9), (8.10) and (8.11), the same data is shown as in Figure's (8.6), (8.7) and (8.8) with fits that use the intensity of the two beams added together, which is 7.81×10^2 cm/GW. This is also conveniently the intensity that delivers us the same fit value of β that we obtained with the single beam Z-Scan. We believe that this fact is a coincidence, and due to the experimental and analytical error involved, as opposed to the theoretical effective intensity as given in Chapter 7 being incorrect.

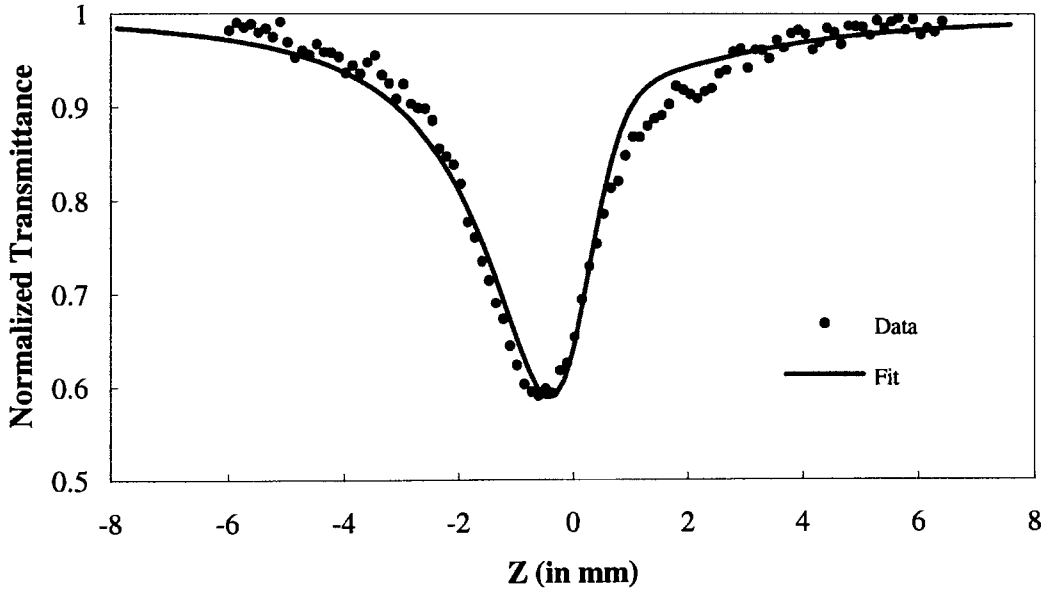

Figure 8.10 Two beam closed aperture Z-Scan performed at 780 nm with ZnSe sample. ($I = 7.81\times10^2$ GW/cm^2 and β =10 cm/GW, $n_2 = 5.7\times10^{-11}$ esu)

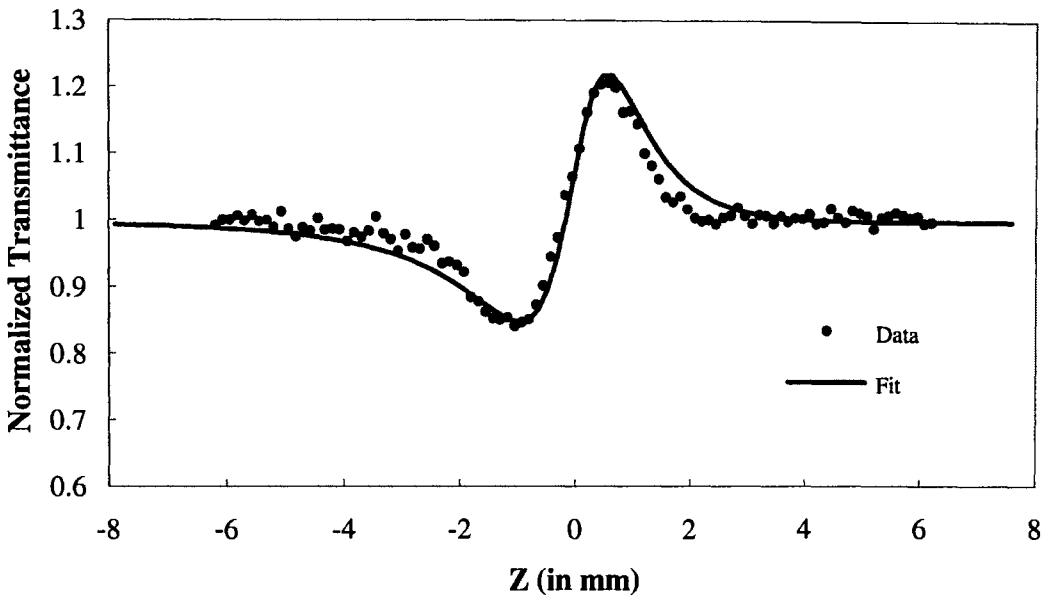

Figure 8.11 Closed aperture Z- scan divided by open aperture Z-scan performed at 780 nm with ZnSe sample. ($I_0 = 7.81\times10^2$ GW/cm^2 and $\beta = 10$ cm/GW, $n_2 = 5.7\times10^{-11}$ esu).

8.5 PDM Z-Scan Measurements

We performed both open and closed PDM Z-Scan measurements upon the same 3.2 mm ZnSe and 1.1 mm thick ZnS samples used in the previous experiments. The data obtained from this procedure can only be used in comparison with an already known nonlinearity, because we have no direct way to calibrate it. However, the only data we have at 780 nm is from the ZnSe, which has a relatively high amount of error. Therefore, I use an alternative method that I believe is correct to within a factor of two. We start by assuming that the peak intensity of the Two Beam Z-Scan at focus is equal to the peak intensity of the PDM Z-Scan, when it is at focus and the beams are temporally overlapped. Then we assume that because the same sample sees the same peak intensity, that the nonlinear change in transmission is the same under both circumstances. Therefore, we assume that the peak of the uncalibrated open aperture PDM Z-Scan for the ZnSe is proportional to the minimum transmission in the Two Beam Z-Scan, also for

ZnSe, and use the fact that the background signals are equivalent to no nonlinear signal to obtain a linear relation between the two. This is plotted for the open aperture, closed aperture and divided scan for ZnSe in **Figure** (8.12). Since, we used a direct linear relation between the two, this is also how the scans look in proportion to each other in the actual scan. The relationship between the open and closed aperture versions of this scan shows us that obviously the relationship between the PDM and the Two Beam data is not linear, and we were not able to fit the data using the methods of the unmodulated Z-Scan.

We knew that the linear transmission through the ZnS sample was approximately the same as that of the ZnSe, and the almost identical readings on the first lock-in amplifier in the far field confirmed this. The ZnS was in the exact same position under all the exact same conditions, except that the amplification of the second lock-in amplifier was 20 times as large as used with the ZnSe previously. We then related the ZnS data to a transmission change, by subtracting the DC offset and dividing it by 20. Then we could use the ratio between the estimated percent transmission of the ZnSe and the full scale to determine the percent transmission of the ZnS signal. There was no signal seen within the noise for the open aperture Z-Scan, so we only show the fits of the ZnS closed aperture Z-Scan. Therefore, we conclude that $\beta = 0$ at $\lambda = 780$ nm for ZnS which is expected from its bandgap energy of Eg = 3.66 eV. We fit the data with a 12 μm spot size, linear refractive index of 2.32 for both the theoretical effective intensity, and the measured intensity. In **Figure** (8.13), n_2 and I_o are $.55\times10^{-11}$ esu and 1.82×10^{3} GW/cm^2 respectively, whereas in **Figure** (8.14) they are 1.25×10^{-11} esu and 7.81×10^{2} GW/cm^2. We conclude that n_2 for ZnS is approximately $.9\times10^{-11}$ esu, and our discussion of the results and comparison will be shown in the next chapter.

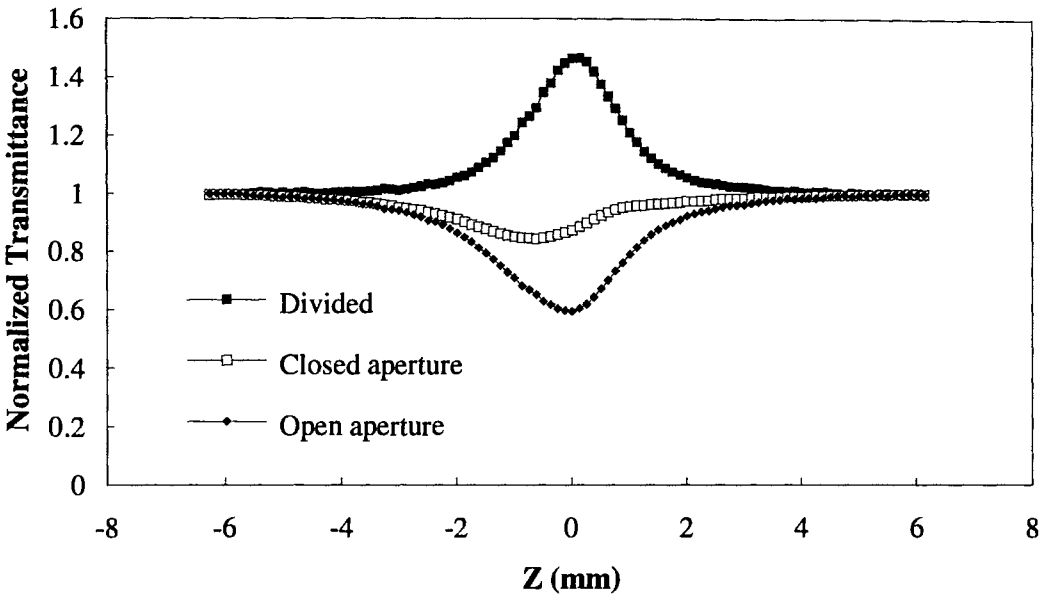

Figure 8.12 PDM Z-scan data for 3.2 mm thick ZnSe after linear calibration.

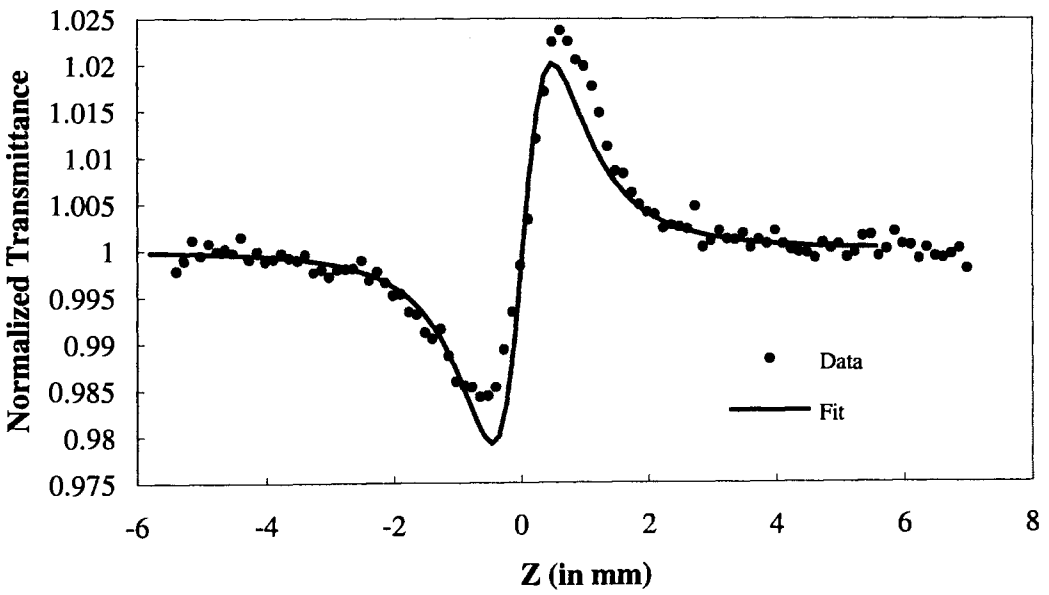

Figure 8.13 PDM Z-Scan of 1.1 mm thick ZnS at 780 nm scaled and fit as a single beam Z-Scan with $I_o = 1.82\times10^3$ GW/ cm^2 and $n_2 = .55\times10^{-11}$ esu.

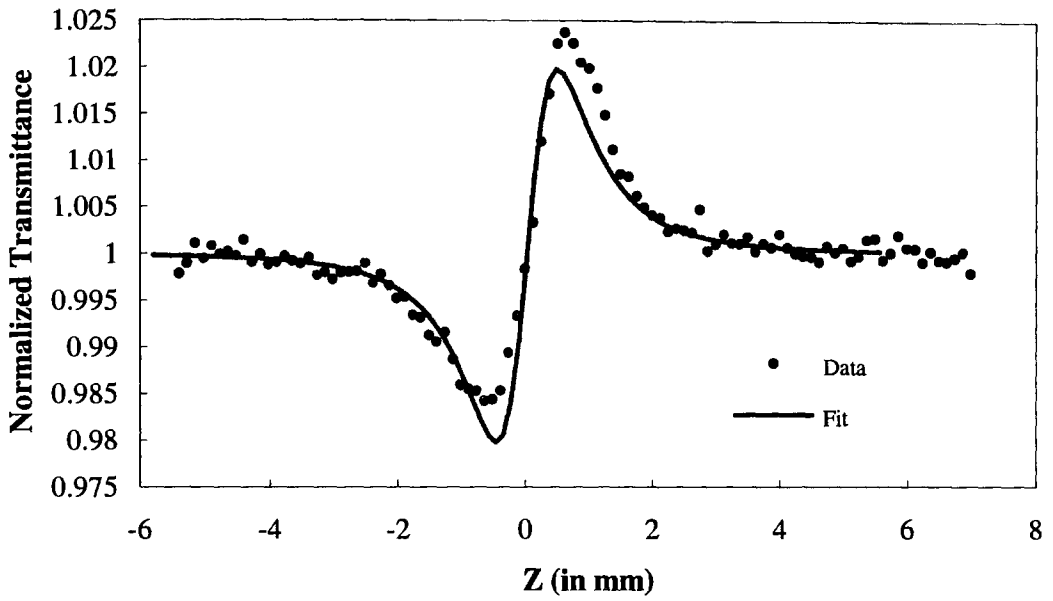

Figure 8.14 PDM Z-Scan of 1.1 mm thick ZnS at 780 nm scaled and fit as a single beam Z-Scan with $I_o = 7.81\times10^2$ GW/ cm^2 and $n_2 = 1.25\times10^{-11}$ esu.

REFERENCES FOR CHAPTER 8

[1] S. A. Miller, "Ultrasensitive Technique for Measurement of Two-Photon Absorption", Phd. Diss., University of North Texas, Denton, TX, 1991.

[2] M. Sheik-Bahae, *Personal Communication* (1994).

[3] A. A. Said, "Development and Application of a Nonlinear Optical Characterization Technique", Phd. Diss., University of North Texas, Denton, TX, 1991

[4] M. Sheik-Bahae, A. A. Said, D. J. Hagan, M. J.Soileau, E. W. Van Stryland, "Nonlinear refraction and optical limiting in thick media," *Opt. Eng.* **30**, 1228-1235 (1991).

CHAPTER 9

CONCLUSIONS

By using a 90 MHz repetition rate Ti:sapphire laser, we were able to measure the two photon absorption in ZnSe and the bound electronic nonlinear refraction in both ZnSe and ZnS at 780 nm. These measurements were obtained using the single beam Z-scan, two beam Z-scan and/or the Pulse Delay Modulated Z-scan (PDM-Z scan), where we were able to get an approximate value (within a factor of three) of the actual values for these parameters. Additionally, we confirmed that the bound electronic nonlinear refractive index seen in ZnS and ZnSe is positive or self focusing at this wavelength, which agrees with the theory of Sheik-Bahae et al. [1], [2]. We were also able to demonstrate that the PDM-Z scan has a sensitivity of over an order of magnitude greater than the single beam Z-scan.

For measuring pulse widths we showed that the signal obtained when performing the Pulse Delay modulation Technique (PDMT) was the derivative of the intensity autocorrelation function $G_2(\tau)$. Furthermore, we were able to determine that the shape of the autocorrelation function using ZnSe generated the same shape and width as that obtained using the second harmonic crystal. Therefore, second order intensity autocorrelations can be performed with ZnSe, so that pulse width measurements can be performed with a good degree of accuracy with a 2PA crystal.

9.1 Analysis

Experimentally, with the single beam Z-scan at an intensity of 4.3×10^2 GW/cm^2, we obtained a value of β =10 cm/GW, however the signal to noise ratio was not high enough for a fit to be made to the closed aperture Z-scan. When the data for the two beam Z-scan

with ZnSe was fitted to the intensity of 1.82×10^{3} GW/cm^2 which takes into account the theoretical nonlinear interaction of the two beams, we obtained values of $\beta = 3.5$ cm/GW and $n_2 = 2.5\times10^{-11}$ esu. The values that we obtained for the measured intensity of 7.81×10^{2} GW/cm^2 gave $\beta = 10$ cm/GW and $n_2 = 5.7\times10^{-11}$ esu. The values for the nonlinear index of refraction as estimated from the PDM-Z scan with ZnS assuming the measured and effective intensities of 7.81×10^{2} GW/cm^2 and 1.8173×10^{2} GW/cm^2 were 1.25×10^{-11} esu and 0.55×10^{-11} esu respectively.

The theoretical values for the nonlinear absorption that were obtained for comparison with our experimental results were based upon a two-parabolic band(TPB) model [1]. The bound electronic nonlinear refractive index n_2 was calculated using a Kramer-Kronig transformation on the calculated absorption spectrum due to two photon absorption, electronic Raman and optical Stark effects [3]. For ZnSe which has an energy gap of 2.58 eV and a linear refractive index of 2.52 at 780 nm, these theories predict that $\beta = 5.1370$ cm/GW and $n_2 = 1.91\times10^{-11}$ esu. For ZnS with a refractive index at 780 nm of 2.32 and a bandgap of 3.6 eV the theory predicts that $\beta = 0$, and that $n_2 = 0.515\times10^{-11}$ esu. Our average values for β and n_2 in ZnSe are 7.9 cm/GW, and 4.1×10^{-11} esu each, whereas the average value for n_2 in ZnS was about 0.9×10^{-11} esu. So, the average values had an error of 50 to 100 percent from the theoretical values, where the variation in the values themselves was between a factor of two and three. Therefore, within the uncertainty of the measurement error, our data was correct. The two beam Z-scans and the PDM Z-scans that took into account the two beam nonlinear interaction gave the values closest to the theoretical ones.

9.2 Discussion

We have found that the PDM Z-scan technique delivered a signal to noise ratio that was over an order of magnitude greater than that obtained with a similar amount of probe

energy in the two beam Z-scan. In addition to reducing the noise and the effects of laser fluctuation , the PDM is only sensitive to irradiance dependent effects like the PDMT. Although, it is a very sensitive technique, the PDM Z-scan is very difficult to calibrate without knowing the nonlinearities of several materials in the region of interest. The method of calibrating the PDM Z-scan that we described in Chapter 8 worked for us, in that we had a low percentage of deviation between our results and the theoretical estimates for these same values. However, from looking at the ZnSe data, it is obvious that there is not a linear correlation between the PDM Z-scan and the two beam Z-scan from zero nonlinear signal to the maximum nonlinear signal. Therefore, if the sensitivity is needed, the technique should be calibrated by comparing the results for several different materials at different intensities so as to determine the true relationship between the self action present and the output of the PDM Z-scan data. Unless, the extra sensitivity or ability to reject thermal nonlinearities is needed then the scan should not be implemented over the other options, because we currently have no way to accurately calibrate the results.

The PDMT was also successfully implemented with the Ti:sapphire laser source, however, there was no evidence that it provided a greater signal to noise ratio than a Z-scan with the same sample irradiance. There were times that its signal to noise was better than that from the Z-scan, however it was difficult to keep the PDMT correctly adjusted and it was very difficult to calibrate. However, relative calibrations should definitely be possible if we have a well known source, and in fact, with further study, an absolute calibration technique may be possible to determine.

Next to the PDM Z-Scan, the Z-Scan performed with the two beams gave us the best signal to noise ratio. This is probably because the effect of the two beam nonlinear interaction is about twice as great as that obtained by summing the two beams, and four times as much as the single beam scan that we performed. However, we are not really

sure what the effect of the two beam nonlinear interaction was, because we experimentally found that the added intensity gave us the same value of β as the single beam Z-scan. In fact, due to the difficulty in accurately aligning this scan, it can never be known as accurately as the single beam Z-scan. Furthermore, there is no advantage of having two beams of the same wavelength. In fact, if we used only one beam outside of the lossy interferometric autocorrelator, then there would have been more laser signal power available. The two beam Z-scan is more difficult to align than the Z-scan and distorts the analysis process. So, even if the true intensity hitting the sample is determined, the two beam Z-scan should not be used unless it is to calibrate a much more sensitive technique like the PDM Z-scan. This is because there is nothing else to gain by using the two beam Z-scan.

The results from using the single beam Z-scan may not seem promising, but it is still the simplest way to obtain data. Furthermore, its simple experimental set up along with the ease and simplicity of its analysis may make up for much of the extra experimental error.

9.3 Future

There are several ways that the application of these experimental techniques can be improved. Since, the performance of these experiments a birefringent filter has been added to the Ti:sapphire, so the output frequency of the laser does not wander. Additionally, we now have the extra flexibility of reliable tuning of the output wavelength over the 750 nm to 850 nm range. Two large high quality corner cubes should be used to give better parallelism of the beams, and to prevent clipping of the beams due to corner cube size or distortion of the beam because of poor surface quality. From the comments in Chapter 6, it is no wonder that I would suggest the introduction of a more stable pump laser. Furthermore, an electrooptic modulator should be used to

elevate the modulation frequency to a lower noise part of the spectrum. It has been shown that the power noise spectrum of the Ti:sapphire laser drops by about 5 decibels, when the modulation frequency is increased from 1 to 2 KHz, and that it drops another 15 decibels when the modulation frequency is increased to 1 MHz [4]. Thus, by modulating at a much higher frequency, we would obtain a better signal-to-noise ratio.

Additionally, although its results were closer to the theoretical predictions, the two beam Z-scan should not be used unless needed for calibration of another scan. Rather, the single beam Z-scan should be used in its own set up, outside that of the interferometric autocorrelator. In this way, the simplicity of the Z scan's analysis could be obtained with a larger intensity. A second lock-in amplifier should be used to monitor a reference detector. This signal could be used to normalize the output of the Z-scan to lower the effects of the laser instability. Finally, a large number of the traditional Z-Scans with the Ti:sapphire should be performed on samples that are known to have minimal thermal nonlinearities and relatively large irradiance dependent nonlinearities. Then, these values can be used to calibrate the PDMT and PDM Z-scans, which are more stable and capable of differentiating between the fluence and irradiance dependent nonlinearities. However, unless a simple and efficient calibration process is determined, the Z-scan technique should be used over the PDMT and Z-scans containing the PDM.

The amount of signal from the single beam Z-scan can be increased by performing the Z-scan outside the interferometric set up. However, it was not the lack of signal that was the problem, rather it was the large long term laser fluctuations. Therefore, it may be worthwhile to decrease the filter time constants on the lock-in amplifiers and accept the extra noise, in exchange for being able to decrease the scan time. The will reduce the effects of the laser drift. Furthermore, a low intensity background scan should be performed to be used as a background subtraction from the actual data.

REFERENCES FOR CHAPTER 9

[1] M. Sheik-Bahae, D. C. Hutchings, D. J. Hagan, E. W. Van Stryland, "Dispersion of bound electronic nonlinear refraction in solids," *IEEE J. Quantum Electron.* **QE-27,** 1296-1309 (1991).

[2] M. Sheik-Bahae, D. J. Hagan, and E. W. Van Stryland, "Dispersion and band-gap scaling of the electronic Kerr effect in solids associated with two photon absorption," *Phys. Rev. Lett.* **65**, 96-99 (1990).

[3] M. Sheik-Bahae, J. Wang, and E. W. Van Stryland, "Nondegenerate Optical Kerr Effect in Semiconducors," *IEEE J. Quantum Electron.* **QE-30,** 249-255 (1994).

[4] N. Sarukura, and Y. Ishida, "Ultrashort Pulse Generation from a Passively Mode-Locked Ti:sapphire Based System," *IEEE J. of Quantum Electron.* **QE-26**, 2134-2141 (1992).